

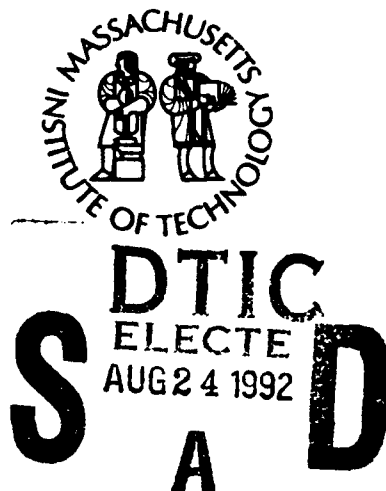


2

Woods Hole Oceanographic Institution Massachusetts Institute of Technology



Joint Program
in Oceanography/
Applied Ocean Science
and Engineering



DOCTORAL DISSERTATION

**A Model of a Mediterranean Salt Lens
in External Shear**

by

David Walsh

June 1992

This document has been approved
for public release and sale; its
distribution is unlimited.

92 8 21 120

381000

92-23447



1728

WHOI-92-21

**A Model of a Mediterranean Salt Lens
in External Shear**

by

David Walsh

**Woods Hole Oceanographic Institution
Woods Hole, Massachusetts 02543**

and

**The Massachusetts Institute of Technology
Cambridge, Massachusetts 02139**

June 1992

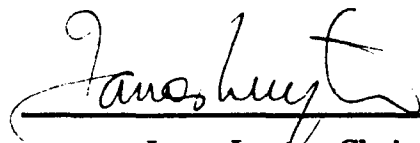
DOCTORAL DISSERTATION

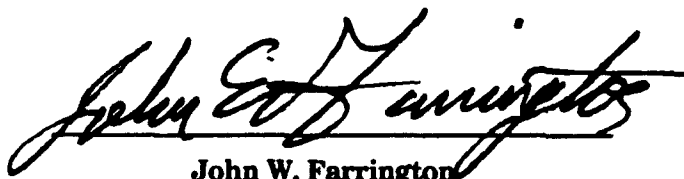
**Funding was provided by the Office of Naval Research through Contract No. N00014-89-J-1182 and
the National Science Foundation under Grant Nos. OCE89-16446 and OCE87-00601.**

**Reproduction in whole or in part is permitted for any purpose of the United States
Government. This thesis should be cited as: David Walsh, 1992. A Model of a
Mediterranean Salt Lens in External Shear. Ph.D. Thesis. MIT/WHOI,
WHOI-92-21.**

Approved for publication; distribution unlimited.

Approved for Distribution:


James Luyten, Chairman
Department of Physical Oceanography


John W. Farrington
Dean of Graduate Studies

Accession For	
NTIS	CRA&I <input checked="" type="checkbox"/>
DTIC	TAB <input type="checkbox"/>
Unannounced <input type="checkbox"/>	
Justification	
By	
Distribution/	
Availability Codes	
Dist	Availability for Special
A-1	

DTIC QUALITY INSPECTED 5

A Model of a Mediterranean Salt Lens in External Shear

by

David Walsh

B.A., Earlham College, 1984

Submitted in partial fulfillment of the
requirements for the degree of

Doctor of Philosophy
at the

MASSACHUSETTS INSTITUTE OF TECHNOLOGY

and the

WOODS HOLE OCEANOGRAPHIC INSTITUTION

April, 1992

© David Walsh, 1992

The author hereby grants to MIT and to WHOI permission to reproduce
and to distribute copies of this thesis document in whole or in part.

Signature of Author

David Walsh

Joint Program in Physical Oceanography
Massachusetts Institute of Technology
Woods Hole Oceanographic Institution
April, 1992

Certified by

Lawrence J. Pratt

Lawrence J. Pratt
Thesis Advisor

Accepted by

Lawrence J. Pratt

Lawrence J. Pratt
Chairman, Joint Committee for Physical Oceanography
Massachusetts Institute of Technology
Woods Hole Oceanographic Institution

A Model of a Mediterranean Salt Lens in External Shear

by
David Walsh

Submitted in partial fulfillment of the requirements for the degree of Doctor of Philosophy
at the Massachusetts Institute of Technology and the Woods Hole Oceanographic Institution
April, 1992

Abstract

A pair of simple models representing the interaction of a continuously stratified f -plane quasigeostrophic lens with a uniform external shear flow is examined. The study is motivated by the desire to understand the processes that affect Mediterranean Salt Lenses and other mesoscale lenses in the ocean. The first model represents the eddy as a pair of quasigeostrophic 'point potential vortices' in uniform external shear, where the two point vortices are imagined to represent the top and bottom of a baroclinic eddy. While highly idealized, the model succeeds in qualitatively reproducing many aspects of the behavior of more complex models. In the second model the eddy is represented by an isolated three dimensional patch characterized by quasigeostrophic potential vorticity linear in z , in a background flow with constant potential vorticity. The boundary of the lens may be deformed by interactions with a uniform background shear. A family of linearized analytical solutions representing such a vortex is discussed in Chapter 3. These solutions represent lens-like eddies with trapped fluid cores, which may propagate through the surrounding water when there is external vertical shear. The analysis predicts the possible forms of the boundary deformation in a specified external flow, and the precession rate of normal mode boundary perturbations in the absence of external flow. The translation speed of the lens with respect to the surrounding fluid is found to be a simple function of the external vertical shear and the core baroclinicity.

A numerical algorithm which is a generalization of the contour dynamics technique to stratified quasigeostrophic flow is used to extend the linear results into the nonlinear regime. This numerical analysis allows a determination of the range of environmental conditions (*e.g.*, the maximum shear and/or core baroclinicity) in which coherent vortex solutions can be found, and allows the stability of the steadily translating solutions to be examined directly. It is found that the solutions are stable if neither the external shear nor the core baroclinicity is too large, and that the breakdown of the unstable solutions is characterized by the loss of an extrusion of core fluid to the surrounding waters. The translation speeds of the large amplitude numerical solutions are found to have the same functional dependence on the external vertical shear and the core baroclinicity that was found in the linear analysis, and it is demonstrated that the solutions translate at a rate which is equal to the background flow speed at the center of potential vorticity of the lens.

As a test of the model results, new data from a recent SOFAR float experiment are presented and compared with the model predictions. The data show that the cores of two different Mediterranean Salt Lenses are tilted, presumably as a result of interactions with external flows. Both the sense of the tilt and its relation to the translation of the lens are in qualitative agreement with the model solutions.

Thesis Advisor:
Lawrence J. Pratt
Associate Scientist

Acknowledgements

Many different people contributed to this thesis, in many different ways. It is not possible to mention all of them here. Special thanks go to my advisor, Larry Pratt, who gave me the idea of using a contour dynamics approach to study Mediterranean Salt Lenses, and who supported me for the last $3\frac{1}{2}$ years. Phil Richardson was my advisor for my first two years in the Joint Program, and generously provided the SOFAR float data used in the thesis. Joe Pedlosky, Glenn Flierl, and Karl Helfrich (the remaining members of my thesis committee) all read the final draft of the thesis carefully, and gave many helpful suggestions. Thanks also to Nelson Hogg, who was the chairman of my defense.

House-mates Jim Bowlin, Mike DeGrandpre, Ray Howard (*emeritus*), and of course my friend Renee White were key in helping me maintain my sanity for these last few years. My fellow students – especially Chen Chang Sheng, Barry Klinger, Antonietta Capotondi, and Liu Zhengyu, gave valuable intellectual and emotional support along the way. I'm grateful to Phil Richardson for introducing me to oceanography when I first came to Woods Hole, and also for those pleasant afternoons spent sailing in the Vineyard Sound. Needless to say, my family was behind me all the way – even though I'm sure they were rather baffled by the whole process of getting a Ph.D.

I am happy to acknowledge the support of the Office of Naval Research (grant N00014-89-J-1182) and the National Science Foundation (grants OCE 8916446 and OCE 87-00601), who supported me while I worked on this thesis.

Table of Contents

Abstract	2
Acknowledgements	4
Table of Contents	5
Chapter 1: Introduction	6
1 Motivation	6
2 Related Work	8
3 Overview of the Thesis	11
4 Derivation of Equations	14
 Chapter 2: A Simple Point Potential Vortex Model	 22
1 Introduction	22
2 Phase Plane Behavior	34
3 Steadily Translating Point Vortex Pairs	38
4 Stability Analysis	42
5 Propagation of the Point Vortex Pairs	44
6 Summary	46
 Chapter 3: A Model of a Lens in Shear: Linear Theory	 48
1 Introduction	48
2 Normal Modes on a Spherical Vortex	55
3 A Monopolar Vortex in External Shear: Steady States ...	61
4 A Vortex with Baroclinic Core in Shear: Translation	68
5 Steady Behavior	76
6 Summary	83
 Chapter 4: Numerical Calculations	 84
1 Introduction	84
2 Derivation of Contour Dynamics Equations	85
3 An Algorithm for Finding Steady Solutions	88
4 Characterization of the Steady Solutions	91
5 Initial Value Runs: Stability	107
6 Summary	129
 Chapter 5: Analysis of Meddy SOFAR Float Data	 130
1 Introduction	130
2 Comparison with the Model Results	142
3 Possible sources of Error	146
 Concluding Remarks	 151
Appendices	154
Bibliography	165

Chapter 1

Motivation

The role played by coherent vortices in the oceanic general circulation is an important unanswered question. The large property fluxes associated with many of these vortices indicates that they may have an important effect on the large scale circulation. Among the best known are Gulf Stream Rings, which are evident in many satellite photographs of the Gulf Stream region. In recent years, new data have shown that subsurface lenses are also quite common in the ocean. For a good introduction to the current knowledge of the behavior of mesoscale and submesoscale lenses, the reader is referred to the review article by McWilliams (1985). Among the better documented are Mediterranean Salt Lenses (Armi *et al.*, 1989; Richardson *et al.*, 1989) and Arctic Eddies (Manley *et al.*, 1985). Mediterranean Salt Lenses ("Meddies") are believed to play an important role in the along-isopycnal transport of heat and salt in the Canary Basin. Armi and Zenk (1984) have estimated that a single Mediterranean Salt Lens may contain as much as 10 days worth of Mediterranean salt outflux. Given the large number of Meddies that have been observed (Richardson *et al.*, 1989), and the large distances they have been observed to travel, it is possible that they may play an important role in determining the structure of the Mediterranean Salt Tongue.

With the advent of the SOFAR float as a practical oceanographic tool, it has become possible to 'tag' an individual eddy, and to observe it continuously for long periods of time. Beginning in 1984, several Meddies were seeded with floats. One of these Meddies ('Sharon') was extensively studied during the two year period for which it was tracked, giving an unprecedented description of the evolution and decay of a Meddy (Armi *et al.*, 1989). During this time, the Meddy drifted more than 1000 km to the south, gradually decaying as a result of intrusive mixing (Ruddick, 1988). Armi *et al.* (1988) also report seeing numerous patches of salty water outside the Meddy core, which suggests that 'chunks' of fluid may be periodically lost from the core, presumably as a result of isolated instability events. Recent work by Hebert *et al.* (1990) and

Shultz Tokos *et al.* (1991) describes the evolution of the size and strength of Meddy Sharon in detail. Another Meddy ("Meddy 2" in Richardson *et al.* (1989)) drifted in a southwestward direction for about 9 months before being catastrophically destroyed in a collision with the Hyeres seamounts. The data from floats deployed in these Meddies show that the interaction between a Meddy and an external flow can have important and readily observable consequences. In Chapter 5 of this thesis new data is presented which demonstrate one such interaction, by showing that the core of a Meddy can be deformed by external flows.

It is now appropriate to summarize various essential physical characteristics of Mediterranean Salt Lenses, which will be referred to often in the following chapters. For more detailed information, the reader is referred to Armi *et al.* (1989), or Richardson *et al.* (1989). A Meddy is typically 60 km in diameter, 800 m thick, and has a rotation period of about a week. Velocities within the core are anticyclonic, increase linearly with radius at any depth within the core, and decay monotonically in all directions outside the core. Maximum azimuthal velocities of over 20 cm s^{-1} have been observed at the edge of the core. The float data indicate that the rotation rate can vary significantly with depth inside the core. This is in agreement with recent work by Prater (*personal communication*), who used XCP data to examine the velocity structure of a Meddy. He found evidence of a marked variation of rotation frequency with depth within the core. Meddies are strongly localized in the vertical: they are typically centered at about 1100 m, the vertical extent of the core is about 800 m, and they have little or no surface or bottom velocity signature. The core contains anomalously warm and salty water ($\Delta T \approx 4^\circ\text{C}$, $\Delta S \approx 1 \text{ psu}$), which is stratified, although the stratification is generally weaker than that of the surrounding water. The estimated Rossby number for a Meddy is fairly low: if the Rossby number is estimated by $Ro \sim U/f_0 R$, then $Ro \approx 0.1$, where the characteristic values $U \approx 20 \text{ cm s}^{-1}$ and $R \approx 30 \text{ km}$ are used for the swirl speed and radius of a Meddy. Alternatively, if the Rossby number is defined as $Ro \sim \zeta/f_0$ (where ζ is the relative vorticity in the core), then the estimated Rossby number is

$Ro \approx 0.2$. Whichever measure of Ro is used, Ro is small enough for quasigeostrophic (hereafter QG) theory to be applied with some confidence. The magnitudes of the shears encountered by Meddies are not well known, but the available data suggest that the external flow speed may vary by some 2 cm s^{-1} over the core region (Saunders, 1981). These observations show that Meddies are strong vortices, in the sense that characteristic internal velocities are much larger than external velocities. An estimate of the Burger number $S = \frac{N^2 D^2}{f_0^2 R^2}$, which provides a measure of the aspect ratio of the lens, is also needed. Hebert (1988) reports a buoyancy frequency of $N = 2.5 \times 10^{-3} \text{ s}^{-1}$ within the core of a Meddy, and if the characteristic values $D = 400 \text{ m}$ (representing the half-depth of the lens), $f_0 \approx 7 \times 10^{-5} \text{ s}^{-1}$, and $R = 30 \text{ km}$ are used, it follows that $\frac{N^2 D^2}{f_0^2 R^2} \approx 0.23$.

Related Work

Thus far, most attempts to model mesoscale lenses have considered isolated eddy models, for which the flow vanishes far from the eddy. However, in the ocean such vortices do not occur in isolation from external flows, and therefore it is important to try to understand how they are influenced by external flows. An intriguing example of what may be a consequence of 'Meddy-mean flow interaction' is found in Richardson *et al.* (1989), who observed Meddies 'propagating' through the surrounding waters at about 1.4 cm s^{-1} . An early example of an isolated eddy model is the study by Ikeda (1982), in which the steady behavior of an homogeneous lens was examined using a $2\frac{1}{2}$ layer model. The vortex was assumed to have formed via the adjustment of an initially cylindrical intrusion. Gill (1981) conducted a detailed investigation of the steady behavior of an homogeneous intrusion in a stratified fluid. In Gill's model the lens was assumed to be infinitely long, and the vertical cross-section was required to be elliptical. Starting with these assumptions, he was able to solve for the flow field associated with the lens.

Only recently have investigators begun to consider the influence of external flows on the behavior of such eddies. There have been a number of studies using such non-isolated eddy models in recent years. The simplest conceptual model is that of Hogg and Stommel (1990), who used a $2\frac{1}{2}$ layer f -plane model to represent the interaction of

a pair of point vortices in a vertically sheared flow. Ruddick (1987) used a three layer model to examine the possible steady configurations for an homogeneous intrusion with finite Rossby number in a large scale strain/shear flow. He found a maximum strain rate beyond which no steady solutions were possible. He thus obtained an estimate of the range of environmental conditions under which coherent vortices could exist. Brickman *et al.* (1990) have extended this work to look at the stability properties of Ruddick's solutions representing a lens in a strain field. Zhmur (1989) has found a class of analytical solutions representing quasigeostrophic vortices with uniform potential vorticity and ellipsoidal shape in a stratified fluid with constant vertical and horizontal shear. This demonstrated that solutions like those found by Ruddick were possible in a more realistic, continuously stratified model. The stability of these solutions was not addressed in the study. Meacham (*unpublished manuscript*) has found steadily precessing ellipsoidal solutions using a model like that of Zhmur, and has used a numerical scheme to obtain steadily precessing solutions with more complex shapes, characterized by three-fold, four-fold, and higher degrees of symmetry.

The translation of mesoscale lenses was not addressed by any of the previously mentioned studies, with the exception of Hogg and Stommel (1990). A number of different mechanisms have been proposed to account for the motion of Meddy-like vortices. Several investigations have focused on the role played by β in eddy motion. Nof (1981) and Killworth (1985) found that analytical solutions were possible in which the lens drifted steadily westward. However, the behavior of these solutions does not resemble that of real Meddies, which generally drift to the south or southwest. McWilliams *et al.* (1986) and Beckmann *et al.* (1989) have examined the evolution of a lens-like anticyclonic eddy on a β -plane using a conventional numerical approach. Both investigations found that anticyclones on a β -plane tended to drift unsteadily in a southwestward direction, which is qualitatively in agreement with observed Meddy movement. Beckmann *et al.* (1989) suggested that the irregularities observed in Meddy trajectories could be attributed to instability events, in which fluid from the core was lost. More recently,

Colin de Verdiere (1991) has proposed an interesting mechanism to account for the observed southward translation of Meddies. He suggests that the gradual flattening of the core due to small-scale mixing processes must be balanced by a southward movement of the lens on the β -plane. None of the models just discussed includes any externally imposed flow field, and thus they ignore any advection and distortion of the core by exterior flows. However, the good qualitative agreement between surface drifter tracks and Meddy trajectories suggests that the large scale external flow may play a significant role in producing the observed translation. In an attempt to isolate another possible mechanism for the observed propagation, Hogg and Stommel (1990) proposed that Meddy motion could be explained by the interaction between external shears and the vertically inhomogeneous distribution of potential vorticity associated with the Meddy. They found solutions which translated at a fraction of the speed of the upper layer, provided that the upper layer flow was not too intense (in which case the vortices were torn apart). This model contains the effect of a baroclinic flow in the "core" of the eddy, which can interact with external flows, but the singular nature of the potential vorticity field is highly unrealistic. The idealized nature of Hogg and Stommel's model makes it difficult to draw meaningful comparisons with oceanographic data. Therefore, it is important to determine whether similar solutions can be found using a more realistic continuous (non-singular) model of the potential vorticity field.

Despite the availability of high quality data and numerous modeling efforts, many questions remain unanswered. Perhaps most importantly, very little work has been done to test the various models mentioned above using real ocean data. In addition, as indicated above, the mechanism responsible for Meddy movement is still a matter of debate. In this thesis, a model has been developed which combines the strengths of several of the models discussed earlier. While the modeling work is primarily directed toward Meddies, the results should apply equally well to other mesoscale lenses, such as those discussed by Richardson (1992, *in preparation*). The model allows a propagation mechanism similar to that proposed by Hogg and Stommel (1990), while also allowing

a realistic stratified flow like that found in real Mediterranean Salt Lenses. We have found that realistic translating solutions exist, representing a lens in an external shear flow, and we have examined the behavior and stability properties of a family of steady solutions.

Overview of the Thesis

The heart of this thesis consists of an examination of a simple f -plane quasi-geostrophic model, which represents a Meddy as a lens with anomalous potential vorticity in an unbounded fluid with constant stratification. The potential vorticity within the core of the Meddy is assumed to be linear in z , and the background flow is characterized by constant potential vorticity. The depth dependent core potential vorticity is consistent with float observations, which show an increase in the rotation frequency with depth in the cores of some Meddies. In addition, this depth dependence allows the solutions to exhibit a propagation similar to that found by Hogg and Stommel (1990). The core of the vortex is bounded by the material surface surrounding the region of anomalous potential vorticity, which may be deformed by interactions with external flows. While highly idealized, the simple model allows a qualitative reproduction of many aspects of the behavior of real Meddies.

The behavior of many of the solutions which have been found is qualitatively similar to those found analytically by Ruddick (1987). However, the flow field associated with his model was rather unrealistic, and the model did not allow propagating solutions. The model employed in this work is far more realistic, since it allows stratification and realistic vertical structure. The model is closely related to that used by Zhmur, except that in the present case the core potential vorticity need not be uniform, but can be a function of z . This introduces new physics into the problem, as baroclinic instability is possible when the depth variations of core potential vorticity become large. The baroclinic core also allows modon-like propagation and the formation of localized extrusions of core fluid in the numerical simulations. Finally, the numerical algorithm used allows a direct examination of the stability properties of the steady solutions.

In Chapter 2 a highly simplified model consisting of a pair of 'point potential vortices' in a shear flow is formulated and discussed. This model is actually an extension of the 'heton' model discussed by Hogg and Stommel (1990) to continuously stratified fluids. The use of point vortices to model quasigeostrophic flow of a stratified fluid was first discussed by Flierl (1987). In the point vortex model, the potential vorticity field associated with the eddy is idealized as a pair of delta functions. The motion of these vortices provides a conceptual model of the behavior of the first two horizontal moments of a more general continuous potential vorticity distribution. This often provides a useful analog to the continuous model, as certain aspects of the dynamics can be illustrated in their simplest form by a collection of interacting point vortices. For example, it illustrates very simply the mechanism by which a baroclinic vortex interacts with an external vertical shear, causing the vortex to translate, like the 'heton' solution discussed by Hogg and Stommel (1990). As a consequence of the extreme simplicity of the model, nonlinear steady state solutions may be found, and their stability properties determined analytically.

Chapters 3 and 4 are devoted to an analysis of a model vortex with a lens-shaped core. The eddy is represented by a lens of fluid with constant potential vorticity in an ambient fluid with uniform potential vorticity. These model assumptions seem to be in good agreement with the available data. It is found that the flow field associated with simple model solutions is in qualitative agreement with the flow measured by Richardson *et al.* (1989). The model is sufficiently simple that analytical solutions can in some cases be found representing a vortex in external shear. In its most general form it has four free parameters, representing the strength of the external vertical and horizontal shear, the baroclinicity of the vortex, and its size. In Chapter 3 a family of linearized analytical solutions is discussed, giving the behavior of the model vortex in weak external shear. The solutions seem to capture many important aspects of the observed structure and behavior of Meddies. For example, they have a large core region of trapped fluid which is deformed by interactions with external flows. The predicted deformations appear to be

quite realistic, based upon a comparison with the available data (which is the subject of Chapter 5 of this thesis). Solutions representing vortices with baroclinic cores translate through the external fluid at a rate proportional to the magnitude of the boundary deformation. The mechanism responsible for this translation is similar to that found in the point vortex solutions, and it is speculated that a similar mechanism may be partially responsible for the observed propagation of Mediterranean Salt Lenses.

While intuitively valuable, the analytical results are only valid within a limited region of parameter space, and numerical techniques are necessary to characterize the model behavior in situations where the linear solution is not valid. Furthermore, the stability properties of the analytical solutions are not known, and the algorithm permits the stability properties of the solutions to be examined directly. This is the subject of Chapter 4 of this thesis. The analysis in Chapter 4 focuses on a characterization of steadily translating solutions which are possible in uniform external shear. These steady solutions represent the time-average behavior a much larger class of unsteady solutions. Even with this simplification, the examination of the behavior of the model solutions in their most general form would require the characterization of the solutions throughout a four dimensional parameter space – an overwhelming task. For this reason, the numerical investigation has been further constrained to an examination of the effect of external vertical shear and variable core baroclinicity on the vortex behavior, thus neglecting the effects of horizontal shear and variable vortex size. Attention is focused on these parameters because the Meddy float data show a core deformation and a translation tendency which are consistent with the model solutions representing a lens with a baroclinic core in an external vertical shear. It is found that the propagation speeds of the numerical solutions are accurately predicted by the linear theory. There is a well defined region of parameter space in which steady solutions can be found: the existence of steady solutions requires that neither the shear nor the baroclinicity of the core can be too large. The stability of the steady solutions is then tested by perturbing them slightly and observing the subsequent evolution of the vortex. This analysis shows that the solutions are in

general stable, as introducing a small perturbation leads only to a periodic modulation of the original steady solution. However, the solutions may be unstable if either the external shear or the baroclinicity is too large. In this case the perturbed solutions are 'drawn out' by the external flow, forming sinuous extrusions of core fluid.

In Chapter 5, new data are presented which show two different Meddies which are 'tilted', presumably due to the influence of external flows. This tilt was inferred from a comparison of trajectories of floats at different depths within the same Meddy, which show a systematic lateral shift of the rotation axis with depth. To the best of our knowledge, this is the first time that the deformation of a subsurface mesoscale eddy has been detected. The tilt of the core is generally perpendicular to the drift direction of the lens, apparently demonstrating a relationship between the deformation of the core and the translation of the lens. The magnitude and direction of the tilt is found to be consistent with the predictions of the model discussed in Chapter 3. The Meddies studied by Richardson *et al.* (1989) were found to move at $1.4 \pm 0.3 \text{ cm s}^{-1}$ relative to nearby floats outside the Meddy cores. It is found that the relationship between the sense of the tilt and the translation is qualitatively in agreement with the model, but the predicted model velocities are significantly less than observed velocities.

Derivation of Equations

In this section we derive the quasigeostrophic equations, and the related equations which govern the behavior of the models discussed in Chapters 2, 3, and 4. The special form of the evolution equations used in the contour dynamics calculations is also derived. The Navier-Stokes equations for a stratified, incompressible fluid on a β plane (see, *e.g.*, Pedlosky, 1987) may be written:

$$\begin{aligned} \frac{D_* u_*}{Dt_*} - (f_0 + \beta y_*) v_* &= -\rho_{0*}^{-1} \frac{\partial p_*}{\partial x_*} \\ \frac{D_* v_*}{Dt_*} + (f_0 + \beta y_*) u_* &= -\rho_{0*}^{-1} \frac{\partial p_*}{\partial y_*} \\ \frac{D_* w_*}{Dt_*} &= -\frac{1}{\rho_*} \frac{\partial p_*}{\partial z_*} - g \end{aligned} \tag{1.1}$$

$$\begin{aligned}
\frac{D_* \rho_*}{Dt_*} &= 0 \\
\frac{\partial u_*}{\partial x_*} + \frac{\partial v_*}{\partial y_*} + \frac{\partial w_*}{\partial z_*} &= 0 \\
\frac{D_*}{Dt_*} &\equiv \partial_{t_*} + u_* \partial_{x_*} + v_* \partial_{y_*} + w_* \partial_{z_*},
\end{aligned}$$

where stars denote dimensional quantities. These equations will now be specialized for quasigeostrophic motions characterized by a depth scale D and a horizontal scale R . Specifically, we shall focus on lens-like phenomena like that shown in Figure 1.1a. We begin by nondimensionalizing the set (1.1). The velocity is scaled by $a_* R$, where a_* is the average value of the quasigeostrophic potential vorticity within the lens. Letting $p_* = p_{0*} + p'_*$ and $\rho_* = \rho_{0*} + \rho'_*$, where the primed variables represent small anomalies on a hydrostatically balanced basic state, and introducing the nondimensional variables $(x, y) = (x_*, y_*)/R$, $z = z_*/D$, $t = t_* a_*$, $(u, v) = (u_*, v_*)/(a_* R)$, $w = w_*/(\delta \epsilon a_* R)$, $p' = p'_*/(\rho_{0*} f_0 a_* R^2)$, and $\rho' = g D \rho'_*/(\rho_{0*} f_0 a_* R^2)$ gives the dimensionless set of equations

$$\begin{aligned}
\epsilon(u_t + uu_x + vv_y + \epsilon wu_z) - (1 + \hat{\beta}y)v &= -p'_x \\
\epsilon(v_t + uv_x + vv_y + \epsilon wv_z) + (1 + \hat{\beta}y)u &= -p'_y \\
\delta^2 \epsilon^2(w_t + uw_x + vw_y + \epsilon ww_z) &= -p'_z - \rho' \\
\rho'_t + u\rho'_x + v\rho'_y + \epsilon w\rho'_z &= wS(z) \\
u_x + v_y + \epsilon w_z &= 0,
\end{aligned} \tag{1.2}$$

where $\epsilon \equiv a_*/f_0$ is a Rossby number, $\delta \equiv D/R$ is the aspect ratio of the vortex, $S(z)$ is the stratification parameter (defined by $S(z) \equiv N^2 D^2 / f_0^2 R^2$), and $\hat{\beta} \equiv \beta R / f_0$. When $S(z) = O(1)$ and $\epsilon \sim \hat{\beta} \ll 1$, the set (1.2) can be expanded in powers of ϵ to obtain the quasigeostrophic potential vorticity equation for synoptic scale motions

$$\begin{aligned}
q_t - \psi_y q_x + \psi_x q_y &= 0, \\
q &= \psi_{xx} + \psi_{yy} + (S^{-1} \psi_z)_z + \frac{\hat{\beta}}{\epsilon} y,
\end{aligned} \tag{1.3}$$

where the geostrophic streamfunction ψ is defined by

$$u = -\psi_y, \tag{1.4}$$

$$v = \psi_x .$$

The dynamical importance of the β effect in QG theory is measured by the parameter $\beta R^2/U$, which for a Meddy is small $\beta R^2/U \sim 0.04 \ll 1$, so that the f plane approximation should be quite good. Furthermore, for simplicity, only the special case in which S is approximately constant will be considered, so that q can be written in the approximate form

$$q \approx \psi_{xx} + \psi_{yy} + S^{-1} \psi_{zz} . \quad (1.5)$$

To examine the effect of an externally imposed flow on the vortex, it will be convenient to divide the flow field into two components: that associated with the vortex itself, and a specified external shear flow

$$\psi = \psi_v + \psi_b . \quad (1.6)$$

The vortex flow is assumed to vanish at large distances, while the background flow may extend to infinity. The streamfunction for the external flow is *defined* by

$$\psi_{b,xx} + \psi_{b,yy} + S^{-1} \psi_{b,zz} = q_b = \text{a constant} . \quad (1.7)$$

Because q_b is constant there is no ambient potential vorticity gradient, and the effect of the background flow is therefore purely advective. The only potential vorticity gradients are therefore those associated with the jump in potential vorticity across the vortex boundary. We shall *choose* ψ_b to be of the form

$$\psi_b = -\alpha yz + \frac{1}{2} q_b y^2 , \quad (1.8)$$

which represents a zonal flow with constant vertical and horizontal shear:

$$u_b = \alpha z - q_b y . \quad (1.9)$$

Of course this is not the only possible form for the external flow that satisfies (1.7), but it will be sufficient to allow an examination of the qualitative effects of large scale

external shear on the vortex. Notice that there is no barotropic flow component. This is because it is assumed that the coordinate system has been chosen to translate at the mean external flow speed. The dimensionless parameters α and q_b are defined by

$$\begin{aligned} q_b &= \frac{q_{b*}}{a_*} \\ \alpha &= \frac{\alpha_* D}{a_* R}, \end{aligned} \tag{1.10}$$

where α_* is a dimensional measure of the vertical shear of the background flow. We note here that this form for the external velocity field is more general than it might seem, as any slowly varying external flow field may be locally represented in this form using a Taylor series expansion. This representation should be adequate as long as the external flow varies on length scales much larger than the size of the lens.

In the following chapters two special forms for the potential vorticity field will be considered in some detail. The most important case is the one in which the potential vorticity is horizontally piecewise constant, which provides a useful idealization of the potential vorticity field of a Meddy. The second case is that in which the potential vorticity field is represented by a pair of delta functions. In Chapter 2 we shall see that this simple model is capable of reproducing many aspects of the behavior of the more complicated continuous model. To model a lens-shaped eddy, it is assumed that the potential vorticity field can be written in the form ¹

$$q_* = q_{b*} + (a_* + b_* z_*) \mathcal{H}(B), \tag{1.11}$$

where the boundary of the vortex is made up of those points satisfying the relation

$$B = 0. \tag{1.12}$$

¹ $\mathcal{H}(B)$ is the Heaviside step function. It has a value of unity if $B > 0$ (i.e., inside the vortex), and a value of 0 if $B < 0$ (outside the vortex).

Equation (1.11) represents a blob with potential vorticity $q_* = a_* + b_* z_* + q_{b*}$ inside, and $q = q_{b*}$ outside. Then the equation for the streamfunction ψ is

$$\begin{aligned} q &= \psi_{xx} + \psi_{yy} + S^{-1}\psi_{zz} = q_b + (1 + bz)\mathcal{H}(B) \\ \psi &\rightarrow \psi_b, \quad r \rightarrow \infty, \end{aligned} \quad (1.13)$$

where

$$b \equiv \frac{b_*}{a_*} D. \quad (1.14)$$

Because S is a constant, the transformation

$$z \rightarrow z/\sqrt{S} \quad (1.15)$$

transforms (1.13) to Poisson's equation. Thus, (1.13) takes the form

$$\begin{aligned} q &= \psi_{xx} + \psi_{yy} + \psi_{zz} = q_b + (1 + bS^{-1/2}z)\mathcal{H}(B), \\ \psi &\rightarrow \psi_b, \quad \text{as } r \rightarrow \infty. \end{aligned} \quad (1.16)$$

The flow associated with a potential vorticity field of this form depends upon the shape of the vortex boundary, and on the value of the parameter b , as well as on the imposed external flow. When the core is monopolar ($b = 0$) and z axisymmetric, and the flow vanishes far from the vortex ($\alpha = q_b = 0$), then the flow inside the core is in solid body rotation, and velocities decay monotonically outside the core (see Figure 3.2a). When b is nonzero the flow in the core is vertically sheared (see Figure 3.2b). In transformed space, the streamfunction for the background flow becomes

$$\psi_b = -\alpha S^{-1/2}yz + \frac{1}{2}q_b y^2, \quad (1.17)$$

where α and q_b are measures of the external shear. Notice that in transformed space both the vertical shear and the baroclinicity depend upon the size parameter S . This is because in transformed space, varying the radius R of the lens results in a vertical stretching or squashing of the lens. The shear α and the baroclinicity b must therefore be

scaled accordingly if the external flow speed variation and potential vorticity variation over the core depth are to remain fixed.

In summary, the equations governing the behavior of the model vortex are:

$$q_t - \psi_y q_x + \psi_x q_y = 0 \quad (1.18)$$

$$\begin{aligned} q &= \psi_{xx} + \psi_{yy} + \psi_{zz} \\ &= q_b + \left(1 + \frac{b}{\sqrt{S}} z\right) \mathcal{H}(B) \end{aligned}$$

$$\psi \rightarrow \psi_b \text{ as } r \rightarrow \infty$$

$$\psi_b \equiv -\alpha S^{-1/2} yz + \frac{1}{2} q_b y^2.$$

The model parameters are defined by

$$\begin{aligned} \alpha &= \frac{\alpha_* D}{a_* R} \\ q_b &= \frac{q_{b*}}{a_*} \\ S &= \frac{N^2 D^2}{f_0^2 R^2} \\ b &= \frac{b_*}{a_*} D, \end{aligned} \quad (1.19)$$

where b is a measure of the baroclinicity of the lens, q_b measures the magnitude of the external horizontal shear, and α measures the vertical shear of external flow.

Equation (1.18) seems to imply that decreasing the stratification parameter S has the same effect as increasing the baroclinicity b . However, it turns out that this is not true, since changing S also changes aspect ratio of the lens (which is manifested as a vertical stretching or squashing of the surface $B = 0$). This can be easily seen by considering the special case in which the vortex boundary is given in dimensional variables by

$$1 - (x_*^2 + y_*^2)/R^2 - z_*^2/D^2 = 0, \quad (1.20)$$

representing a spheroid with aspect ratio $\frac{D}{R}$ (see Figure 1.1a). After nondimensionalizing and carrying through the coordinate transformation (1.15), one finds that the

transformed boundary is given by

$$\mathcal{B} = x^2 + y^2 + z^2/S - 1 = 0. \quad (1.21)$$

This describes a spheroid with aspect ratio \sqrt{S} , which will be spherical only in the special case in which $S = 1$ (i.e., $R = ND/f_0$). In Chapters 3 and 4 we will consider a model of a lens for which $S = 1$. A lens with radius larger than ND/f_0 is oblate in transformed space; a lens with radius less than ND/f_0 is prolate.

The time evolution of the flow can be found by integrating the potential vorticity equation (1.18a). For the special class of flows characterized by the potential vorticity (1.16), this equation takes a particularly simple form. This expression can be obtained by substituting the diagnostic relation between q and ψ given in (1.16) into (1.3a). This gives a kinematic boundary condition, which is needed to ensure that the boundary of the lens is a material surface. One finds:

$$(\partial_t + \psi_x \partial_y - \psi_y \partial_x)(q_b + (1 + bS^{-1/2}z)\mathcal{H}(\mathcal{B})) = 0, \quad (1.22)$$

and it follows that

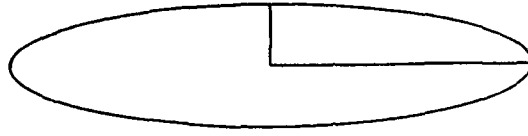
$$(1 + bS^{-1/2}z)\delta(\mathcal{B})(\partial_t + \psi_x \partial_y - \psi_y \partial_x)\mathcal{B} = 0. \quad (1.23)$$

Thus when $\mathcal{B} = 0$ the condition

$$(\partial_t + \psi_x \partial_y - \psi_y \partial_x)\mathcal{B} = 0 \quad (1.24)$$

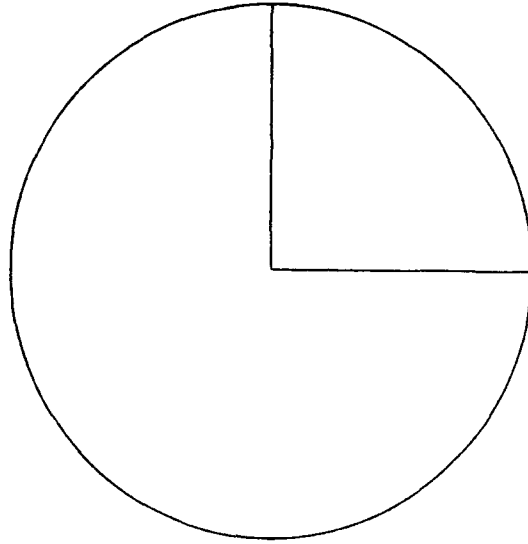
must be satisfied. This is the kinematic boundary condition which will be used in Chapters 3 and 4 to determine the evolution of the flow field.

a



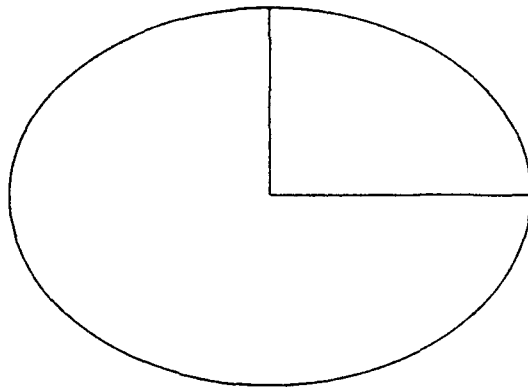
$$\frac{x_*^2 + y_*^2}{R^2} + \frac{z_*^2}{D^2} = 1$$

b



$$x^2 + y^2 + z^2 = 1$$

c



$$x^2 + y^2 + \frac{z^2}{S} = 1$$

Figure 1.1: Schematic showing how the boundary of a lens which is a prolate spheroid with aspect ratio D/R is changed by the various coordinate transformations discussed in this chapter. Schematic of lens shape (a) in the ocean, (b) in nondimensional space, and (c) after the transformation (1.15). In transformed space the lens is a spheroid with aspect ratio \sqrt{S} .

Chapter 2

A Simple Point Vortex Model

Introduction

In this chapter the behavior of a quasigeostrophic vortex in a shear flow will be examined using a very simple point vortex analog. The model consists of a pair of three dimensional 'point potential vortices' with strengths Q_1 and Q_2 in a flow with constant vertical and horizontal shear. The point vortices are advected by the background flow as they go around one another due to their mutual interactions. This seemingly simple situation allows for a rich variety of behaviors. The point potential vortex model used here is closely related to that discussed in the review by Flierl (1987), while the systematic application of the point vortex ansatz in examining the stability and propagation of oceanic mesoscale lenses can be traced to recent work by Hogg & Stommel (1990). It will be convenient to think of the point vortex pair as a crude representation of the behavior of the first two horizontal moments of some more general continuous potential vorticity distribution. The separation of the vortices represents the size and deformation of the analogous continuous vortex, while their strengths represent the integrated potential vorticity in the upper and lower halves of the vortex, respectively. In the next chapter, it will be seen that the point vortex model often anticipates the behavior of a continuous vortex subject to low mode forcing (that is, in a gradually varying background flow), as a low mode forcing typically produces a low mode response.

In this case the flow consists of a pair of point vortices located at (x_1, y_1, z_1) and (x_2, y_2, z_2) in an external flow with constant potential vorticity, and therefore the equation for the streamfunction is

$$\begin{aligned}\psi_{xx} + \psi_{yy} + \psi_{zz} &= q_b + 4\pi Q_1 \delta(\vec{r} - \vec{r}_1) + 4\pi Q_2 \delta(\vec{r} - \vec{r}_2) \\ \psi &\rightarrow \psi_b \quad (r \rightarrow \infty),\end{aligned}\tag{2.1}$$

where Q_1 and Q_2 can be written in the form

$$Q_1 = 1 + \Delta, \tag{2.2}$$

$$Q_2 = 1 - \Delta.$$

Δ measures the antisymmetric component of the potential vorticity field, and it follows from (2.1) and (2.3) that $\Delta = 0$ implies that the vortices have equal strengths, while the limit $\Delta \rightarrow \infty$ represents two oppositely signed vortices. The point vortex configuration is sketched in Figure 2.1.

It is easily verified that a solution to (2.1) is

$$\begin{aligned}\psi &= \psi_b - \frac{Q_1}{|\vec{r} - \vec{r}_1|} - \frac{Q_2}{|\vec{r} - \vec{r}_2|}, \\ \psi_b &= -\alpha yz + \frac{q_b}{2} y^2.\end{aligned}\tag{2.3}$$

This is not the most general form for ψ_b , but it will be sufficient for our purposes, as it represents a flow with both vertical and horizontal shear. Because the point vortices are material particles, they must move at the local flow speed, and it follows that their motions are given by

$$\begin{aligned}\frac{dx_n}{dt} &= -\frac{\partial \psi}{\partial y} \Big|_{\vec{r}_n} \\ \frac{dy_n}{dt} &= \frac{\partial \psi}{\partial x} \Big|_{\vec{r}_n},\end{aligned}\tag{2.4}$$

for $n = 1, 2$. Taking the horizontal gradient of (2.3), using (2.4), and evaluating the result at the positions of the vortices gives a coupled set of equations governing their motions. Thus, the motion of two QG point potential vortices in a zonal flow given by $u_b = \alpha z - q_b y$ is governed by

$$\begin{aligned}\dot{x}_1 &= \frac{-Q_2(y_1 - y_2)}{|\vec{r}_1 - \vec{r}_2|^3} + \alpha z_1 - q_b y_1 \\ \dot{x}_2 &= \frac{-Q_1(y_2 - y_1)}{|\vec{r}_1 - \vec{r}_2|^3} + \alpha z_2 - q_b y_2 \\ \dot{y}_1 &= \frac{Q_2(x_1 - x_2)}{|\vec{r}_1 - \vec{r}_2|^3} \\ \dot{y}_2 &= \frac{Q_1(x_2 - x_1)}{|\vec{r}_1 - \vec{r}_2|^3} \\ \dot{z}_1 &= 0 \\ \dot{z}_2 &= 0.\end{aligned}\tag{2.5}$$

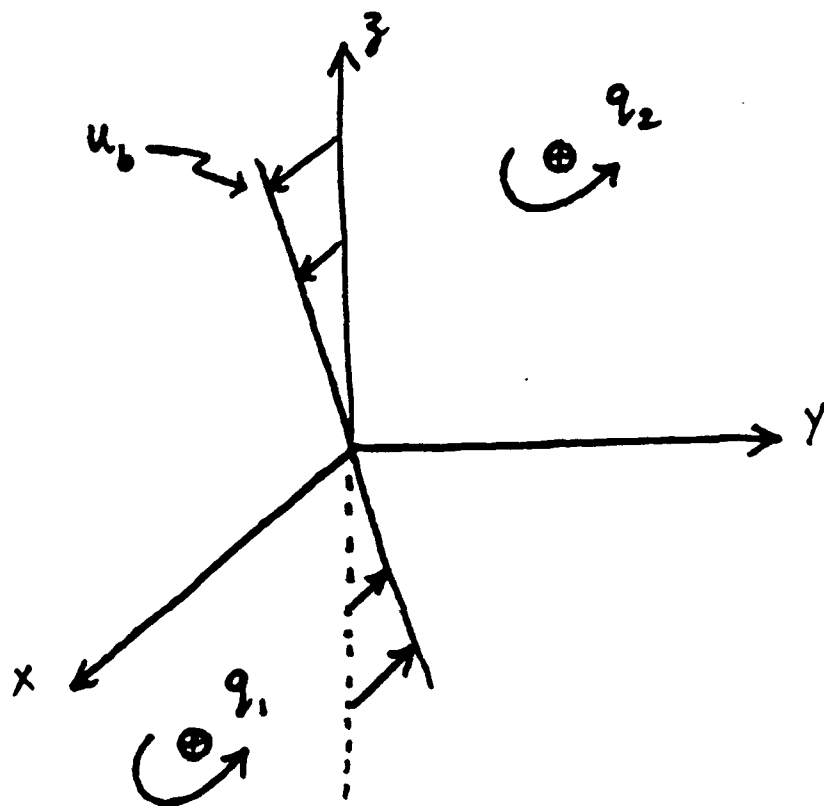


Figure 2.1: Schematic of two point potential vortices of strengths Q_1 and Q_2 in a background flow with constant shear.

Notice that the velocity of each vortex is equal to the sum of the velocity induced by the other vortex plus an advection by the background flow.¹ The last two equations are a consequence of the quasigeostrophic nature of the flow². In Figure 2.2 the velocity field is contoured for a single point vortex in a quiescent fluid. Notice that when $z \neq 0$, the velocity peaks some distance away from the vertical axis.

Figures 2.3a through 2.3i show the trajectories of two point vortices with strengths $Q_1 = 3/2$, $Q_2 = 1/2$, for various initial configurations. These were obtained by integrating the equations (2.5) numerically. In each case the trajectory of the stronger vortex is shown by a solid line, that of the weaker vortex by a dash-dotted line, and that of their center of potential vorticity $(Q_1 \vec{r}_1 + Q_2 \vec{r}_2)/(Q_1 + Q_2)$ by a dashed line. The vortices are positioned such that there is initially no net advection by the background flow. In these runs the vortices are initially at $x_1 = x_2 = 0$, $z_1 = 1$, $z_2 = -1$, and the initial y positions are symmetric with respect to the x, z plane. Figure 2.3a shows that in the absence of external shear the vortices describe circular orbits about their common center of vorticity. In 2.3b a very small external vertical shear is introduced, with the result that the orbits no longer close on themselves, and there is a slow drift to the right. The remaining plots show translating vortex pairs in external shear. Figures 2.3c through 2.3e show the vortices in horizontal shear ($\alpha = 0.0$, $q_b = -0.05$); Figures 2.3f through 2.3i show them in vertical shear ($\alpha = 0.05$, $q_b = 0.0$). In each of these sequences, the external shear is held fixed, and the initial y separation of the vortices is varied. In 2.3c the initial y separation $y_2 - y_1$ is -2.78, in 2.3d it is -2.0, and in 2.3e it is -1.0. In 2.3f the initial separation is -3.70, in 2.3g it is -0.448, in 2.3h it is 0.0, and in 2.3i it is +1.0. These runs are summarized in Figure 2.5, in which the phase plane behavior of the vortex pairs is shown.

The mechanism behind the propagation of the vortex pairs is quite simple, and can be seen in its purest form in the propagation of a purely antisymmetric pair ($Q_1 =$

¹As is customary, a dot denotes a derivative with respect to time.

²In quasigeostrophic theory, advections are assumed to be purely horizontal and therefore the z coordinates of the vortices can't change.

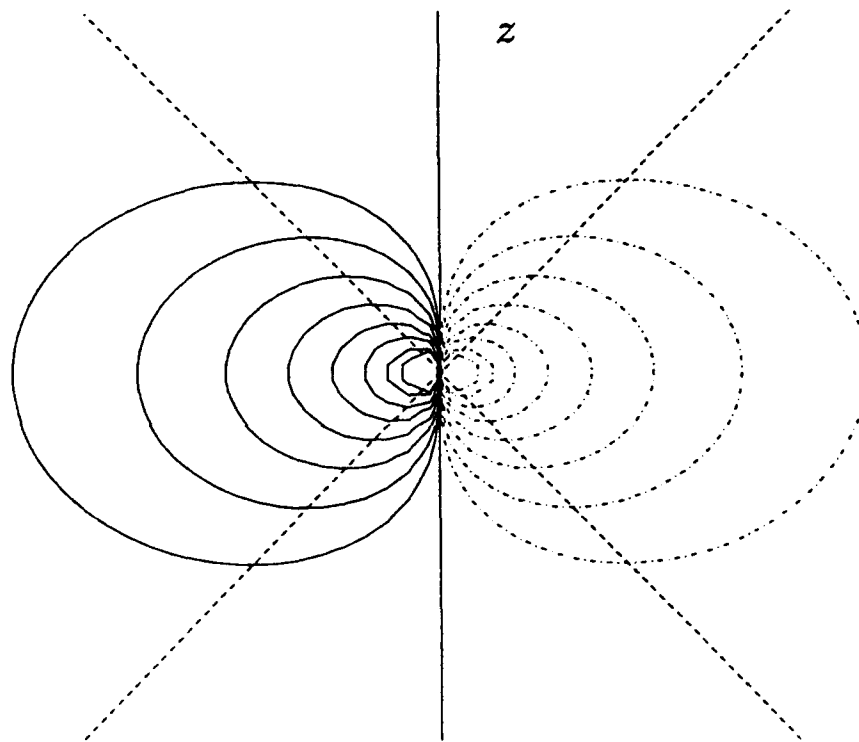
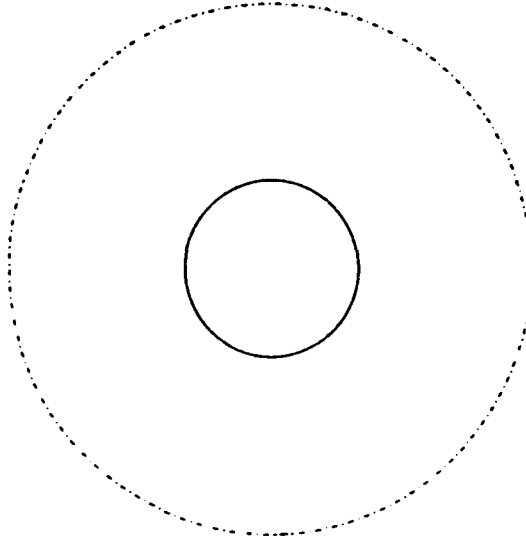


Figure 2.2: Contour plot of velocity field for a single point vortex. The dashed lines connect the points at which the velocity is maximum as a function of perpendicular distance from the z axis.

a



b

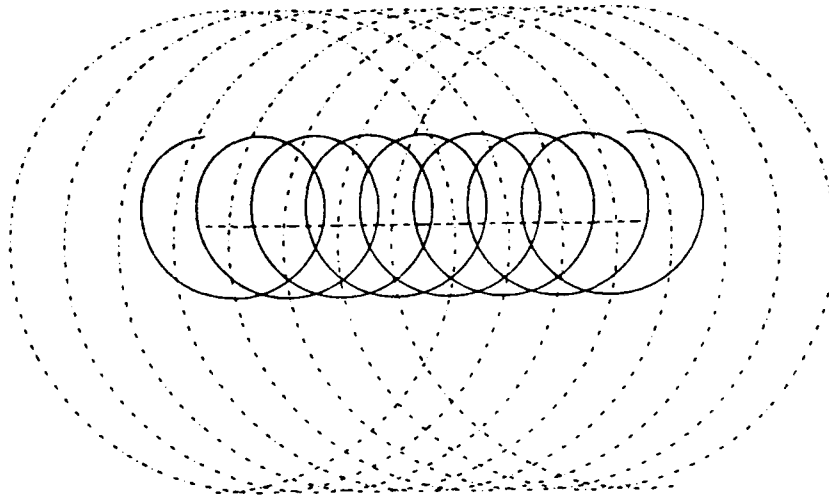
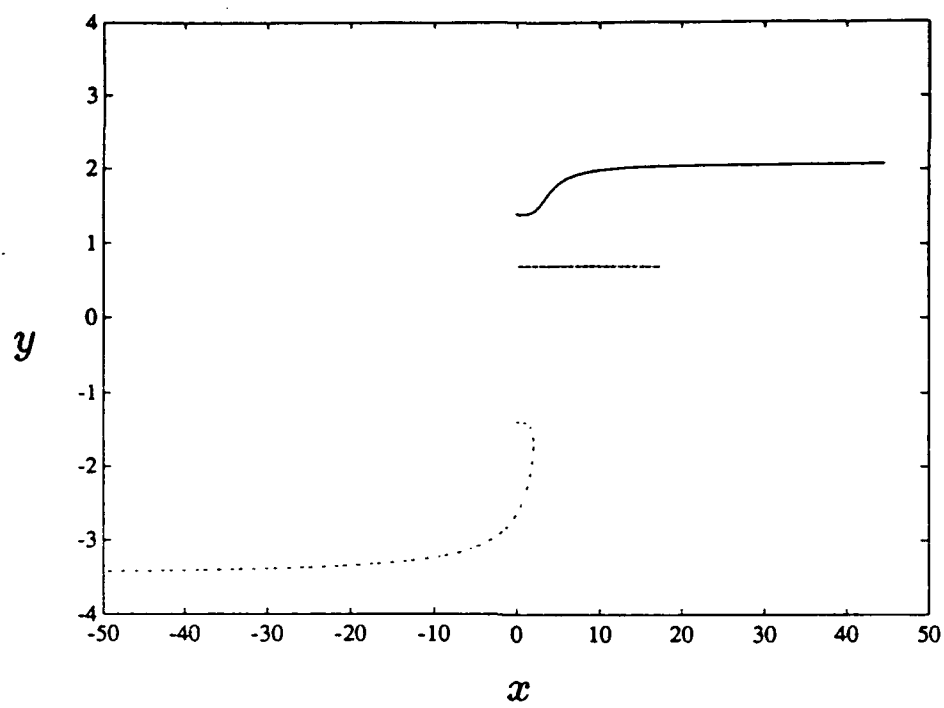
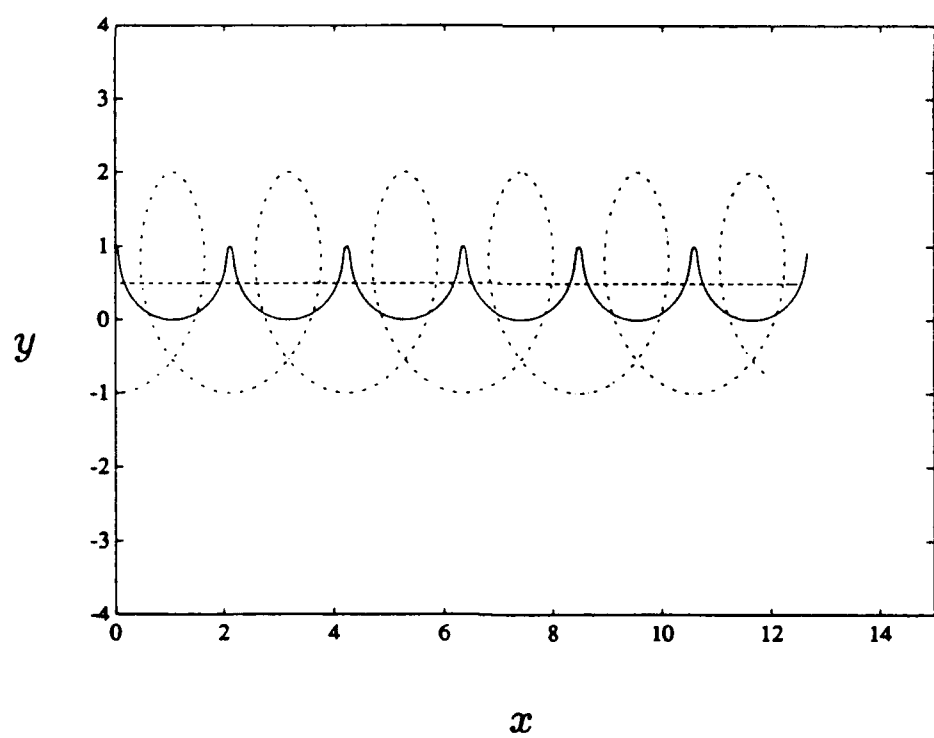


Figure 2.3: Point vortex trajectories obtained by integrating (2.5) in time. Plot (a) shows two point vortices circling one another in a quiescent fluid, (b) demonstrates the effect of adding a weak external vertical shear. (c)-(e) show the two vortices in horizontal shear (for various initial separations), and (f) through (i) show them in vertical shear.

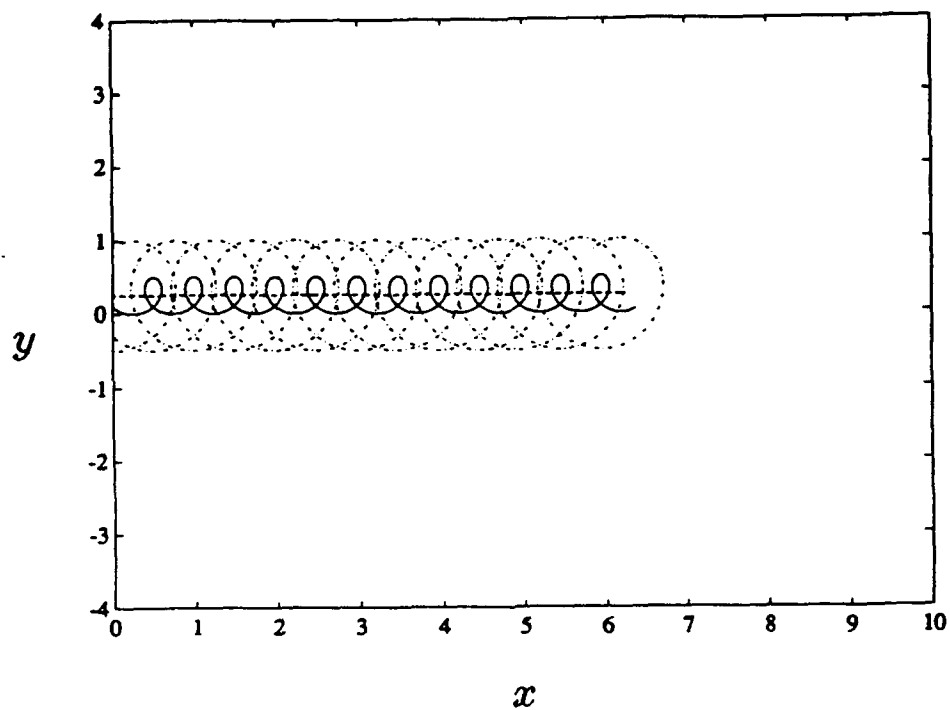
c



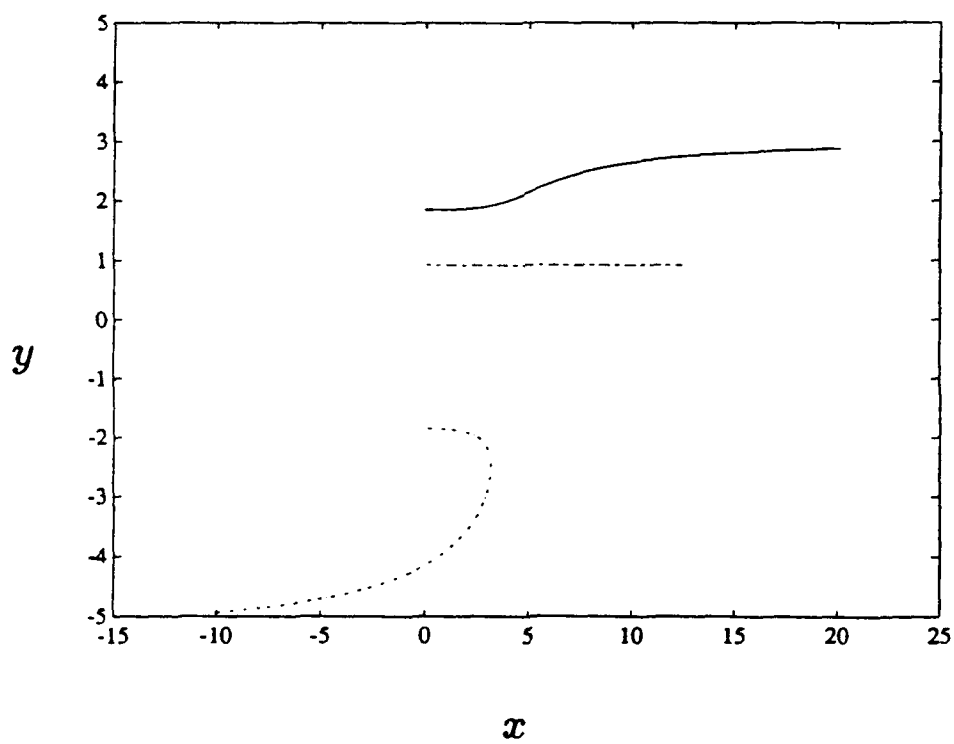
d



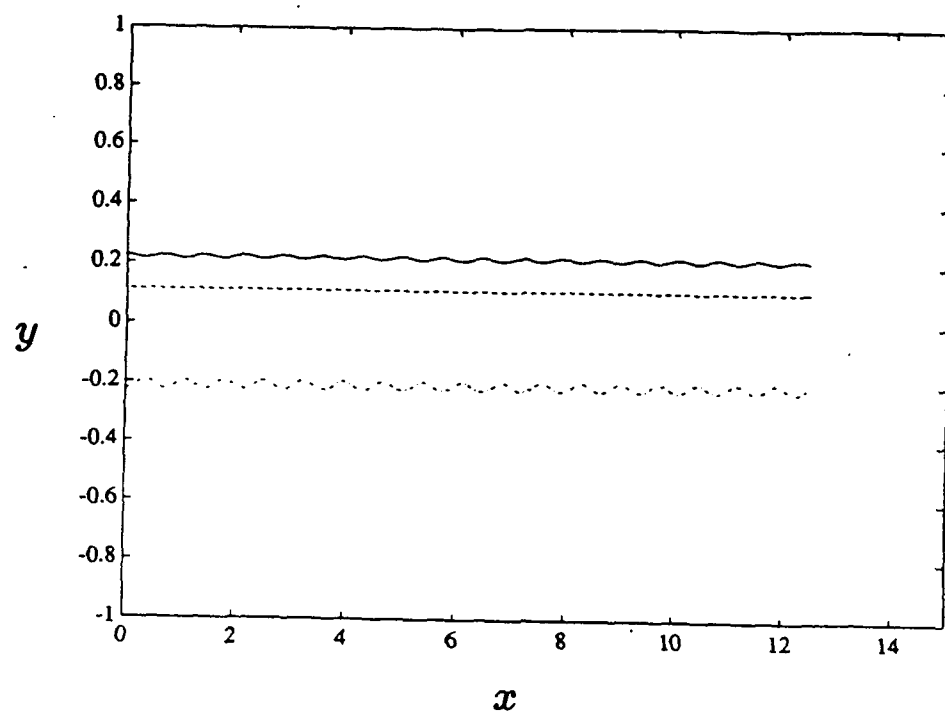
e



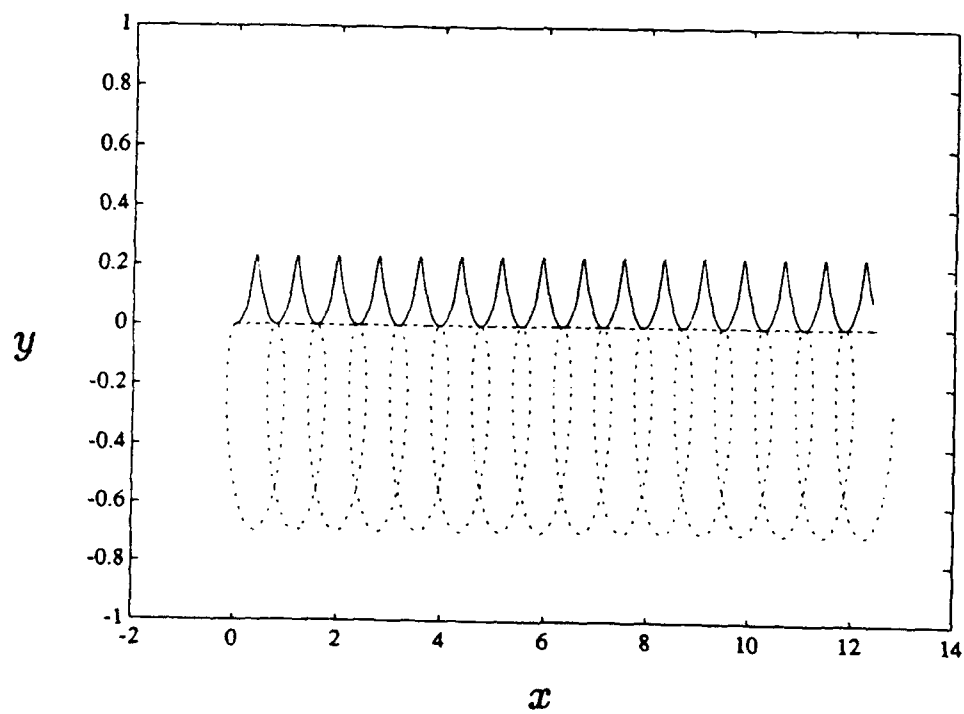
f



g

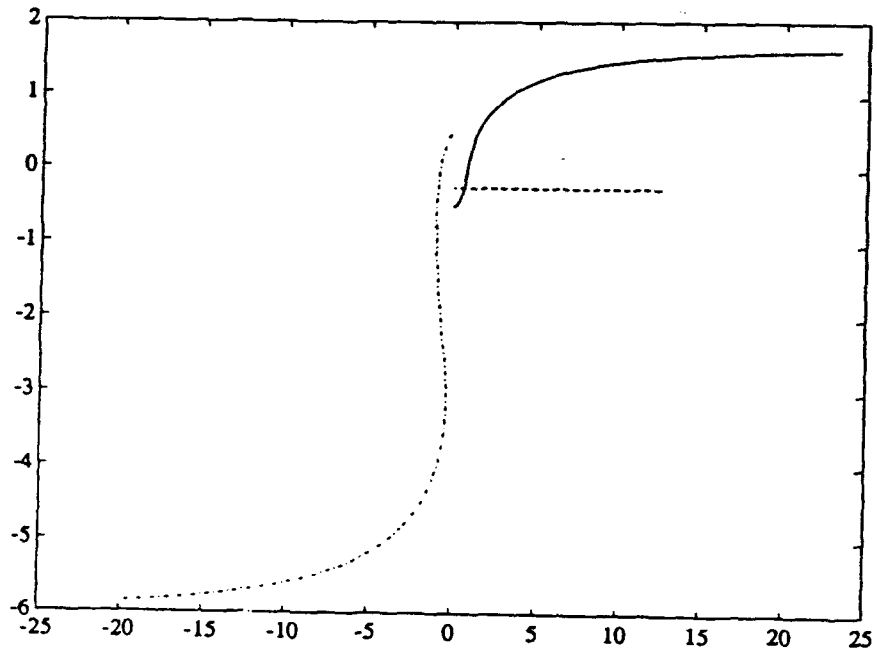


h



i

y



x

1, $Q_2 = -1$) in a quiescent fluid. This situation is shown schematically in Figure 2.4. For such a pair, the circulations of the vortices are of opposite signs, so that the advection of the second vortex by the first vortex is in the same direction as the advection of the first vortex by the second. This leads to a net translation of the vortex pair. The propagation mechanism is much the same when the vortex pair is not purely antisymmetric, except that in this case an external shear is needed to counterbalance the influence of the symmetric component of the potential vorticity field, giving the vortices a preferred orientation (in a time average sense) with respect to the external flow.

It will be convenient to cast the set (2.5) in a new form, which explicitly decouples the translation of the vortices from their relative motions. We shall see that in considering the relative motions of the vortices, the antisymmetric component of the potential vorticity field (given by Δ) drops out of the problem entirely. Δ is only important in determining the translation of the vortex pair as a whole. For convenience the notation $X \equiv \frac{1}{2}(x_1 - x_2)$, $Y \equiv \frac{1}{2}(y_1 - y_2)$, $Z \equiv \frac{1}{2}(z_1 - z_2)$, $R \equiv \sqrt{(2X)^2 + (2Y)^2 + (2Z)^2}$, $u_{b,1} \equiv -\partial_y \psi_b |_{\vec{r}_1}$, $u_{b,2} \equiv -\partial_y \psi_b |_{\vec{r}_2}$, $U \equiv \frac{1}{2}(u_{b,1} - u_{b,2})$, is introduced, after which subtracting (2.5b) from (2.5a), and (2.5d) from (2.5c) (and recalling the definitions of Q_1 and Q_2) gives:

$$\begin{aligned}\dot{X} &= -Y/R^3 + \alpha Z - q_b Y \\ \dot{Y} &= +X/R^3 ,\end{aligned}\tag{2.6}$$

and of course

$$\dot{Z} = 0 .$$

The set (2.6) describes the evolution of the relative displacement of the two vortices. Notice that Δ does not appear, implying that the evolution of the displacement (for a given initial vortex configuration) is uniquely determined by the external flow for *all* values of Δ .

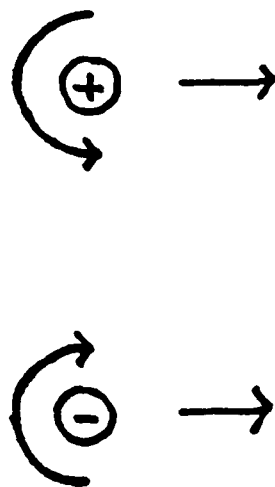


Figure 2.4: Schematic of mechanism by which oppositely signed point vortices can 'self propagate'. The upper vortex is advected by the anticyclonic flow of the lower vortex, causing the upper vortex to move to the right. At the same time, the lower vortex is advected to the right by the cyclonic flow of the upper vortex, causing the pair to move to the right.

In a similar fashion, adding (2.5b) and (2.5a), and (2.5d) and (2.5c) gives an expression for the motion of the center of the vortex pair:

$$\begin{aligned}\dot{\bar{x}} &= +\Delta Y/R^3 + \overline{u_b} \\ \dot{\bar{y}} &= -\Delta X/R^3,\end{aligned}\tag{2.7}$$

where the overbar denotes a spatial average (e.g., $\bar{x} = (x_1 + x_2)/2$). Equation (2.7) says that geometric center of the pair moves under the combined influence of the background flow and the advection due to the *antisymmetric* component of the potential vorticity field. Notice that the set (2.6), (2.7) are equivalent to (2.5), as once X , Y , \bar{x} , and \bar{y} are known, the positions \bar{r}_n of the vortices can be readily computed, since $x_1 = \bar{x} + X$, $x_2 = \bar{x} - X$, etc.

Phase plane behavior

To study the behavior of nonequilibrium solutions to (2.6), the equations can be integrated numerically and the solution trajectories plotted in (X, Y) space. To do this, it is convenient to introduce a new streamfunction Ψ describing the relative vortex motions, defined by

$$\begin{aligned}\Psi_X &= +\dot{Y} \\ \Psi_Y &= -\dot{X}.\end{aligned}\tag{2.8}$$

After making use of (2.6), (2.8) may be integrated numerically to get Ψ . The streamlines $\Psi = \text{constant}$ give solution trajectories in (X, Y) space. Fixed points represent steadily translating configurations, while closed trajectories represent solutions which are periodic in a translating reference frame. Saddle points represent unstable steady solutions; centers represent stable steady solutions. It will be seen that all solutions are periodic if the external shear is not too large, and are nonperiodic otherwise.

First consider background flows with purely horizontal shear. The phase plane plots are shown in Figure 2.5a. The qualitative behavior of the solutions depends on the sign of q_b . When q_b is negative there are three fixed points in (X, Y) space, representing

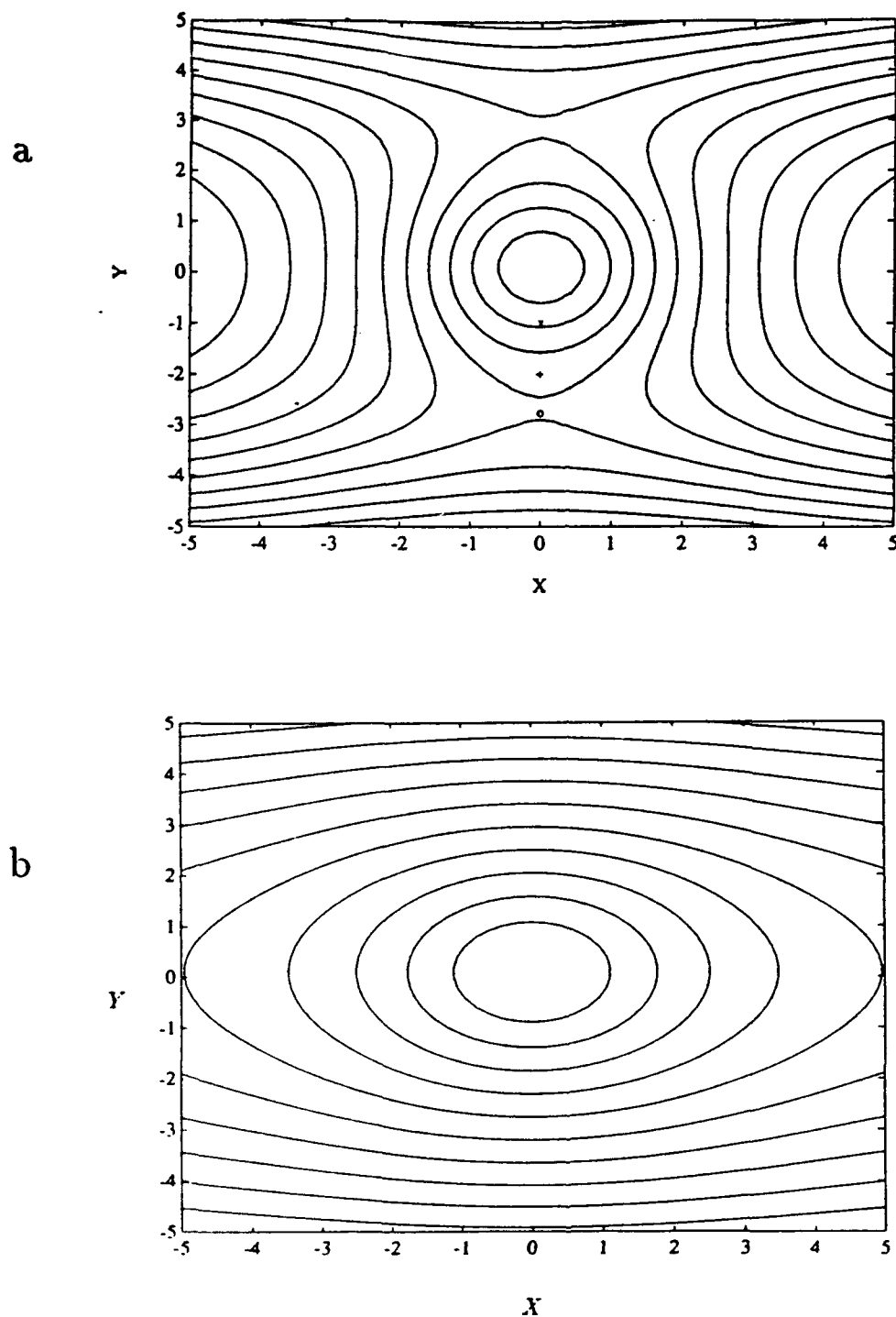
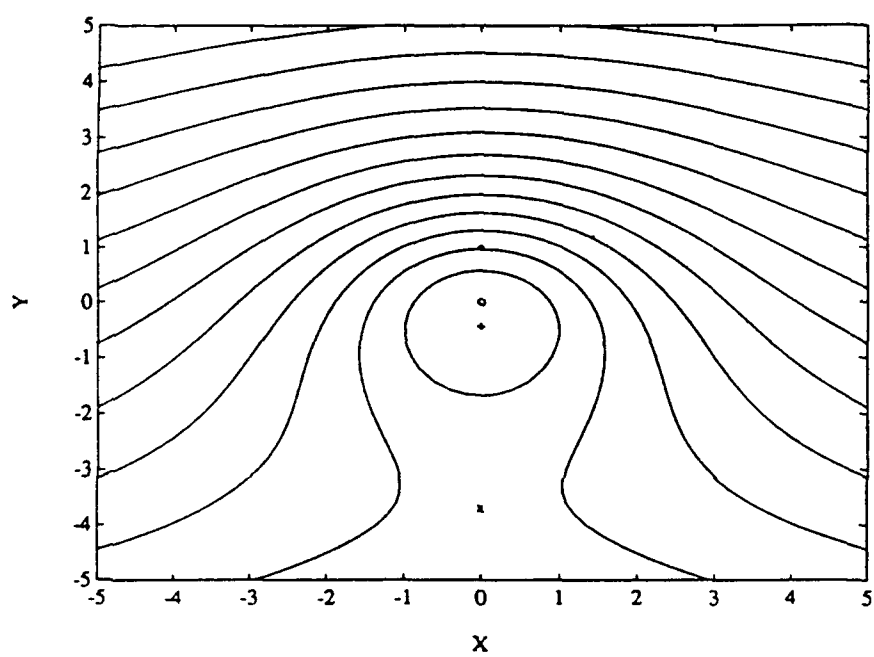


Figure 2.5: Phase plane behavior of point vortex pairs in (X, Y) phase space. (a) represents the case in which the vortices are in horizontal shear ($q_b < 0$), (b) represents the horizontal shear case as well, but with ($q_b > 0$), and (c) represents the case in which they are in vertical shear. The fixed points represent steadily translating point vortex configurations. The 'o' in Figure 2.5a represents the run in Figure 2.3c, the '+' represents the run in 2.3d, and the 'x' represents that in 2.3e. The 'x' in Figure 2.5c represents the run shown in Figure 2.3f, the '+' represents 2.3g, the 'o' represents 2.3h, and the '*' represents the run in 2.3i.

C



steady configurations. The first is a stable ³ fixed point (a center) at $X = Y = 0$ surrounded by a region of closed trajectories, representing periodic solutions. There are also two unstable fixed points, situated at the saddle points on the Y axis. These represent configurations in which the vortices are displaced in a direction perpendicular to that of the external flow. The symbols in the plots represent the initial configurations for the numerical runs shown in Figure 2.3. The 'o' located near the saddle point in Figure 2.5a represents the run in Figure 2.3c, and it shows that the run was very close to an unstable steady solution.

When q_b is positive there is just one fixed point (as shown in Figure 2.5b) - the same stable fixed point at the origin discussed earlier. In this case, however, there are no other fixed points, as the background shear is of the wrong sense to balance the motions of the vortices. It is worth noting that in this case *all* the trajectories are closed, so the vortices *cannot* be carried arbitrarily far apart by the flow, and therefore they remain at least weakly coupled for all time. This implies that any coupled vortex configuration of this kind (not necessarily steady) is more robust when $q_b > 0$ than when $q_b < 0$.

For a vertically sheared background flow the situation is quite different, as Figure 2.5c shows. In this case there are two fixed points - one stable, one unstable. Both of these represent configurations which are 'tilted' by the background flow. The saddle point near the bottom of the figure represents a strongly tilted unstable configuration; the center near the middle of the plot represents a weakly tilted stable configuration. The '+' represents the initial configuration for the run in Figure 2.3g, which was clearly close to the stable fixed point. The 'x' represents the run in Figure 2.3f, which was close to the unstable fixed point. There are no solutions representing vertically aligned ('untilted') vortex pairs, as were found in the horizontally sheared case. As $1/UZ^2$ decreases, the region of closed trajectories surrounding the stable fixed point gets smaller until eventually no bound states are possible.

³This solution is stable, since, when perturbed, the system falls onto one of the closed trajectories adjacent to the fixed point, and hence remains 'near' the unperturbed solution for all time.

Steadily translating point vortex pairs

Now (2.6) can be used to examine in detail the character of the possible steady solutions. These solutions will correspond to the fixed points in the phase plane diagrams just discussed. However, they will be somewhat more general, as each of the phase plane plots applies to a specific parameter setting, while the present analysis will give the positions of the fixed points as functions of the model parameters α , q_b , etc. Setting $\dot{X} = \dot{Y} = 0$ gives

$$X_s = 0 \quad (2.9)$$

(so all steady configurations must be perpendicular to the background flow) and hence also

$$\frac{1}{(Y_s^2 + Z_s^2)^{3/2}} Y_s = \alpha Z_s - q_b Y_s, \quad (2.10)$$

where the subscript s denotes a steady solution to (2.6). Equation (2.10) is simply the mathematical statement of the fact that for a steady solution to exist, the tendency of the background flow to tear the vortices apart must be exactly counterbalanced by the mutually induced velocities.

For our purposes it will be sufficient to solve (2.10) graphically. Consider first a horizontally sheared background flow, in which case $\alpha = 0$, and (2.10) is satisfied if either

$$Y_s = 0, \quad (2.11)$$

or

$$Y_s^2 + Z_s^2 = \left(\frac{-1}{q_b}\right)^{2/3}. \quad (2.12)$$

Thus, either $Y_s = 0$, so that the vortices are right on top of each other, or else they lie on a circle (in (Y_s, Z_s) space) of radius $(\frac{-1}{q_b})^{1/3}$, as shown in Figure 2.6. The three steady solutions represented in Figure 2.6 correspond to the three fixed points in the phase plane diagram shown in Figure 2.5a. Configurations lying along the circle represent vortex pairs which are displaced in a direction perpendicular to the background flow. Notice that if $\frac{1}{q_b} > 0$, the radius $(\frac{-1}{q_b})^{1/3}$ of the circle is negative, implying that no

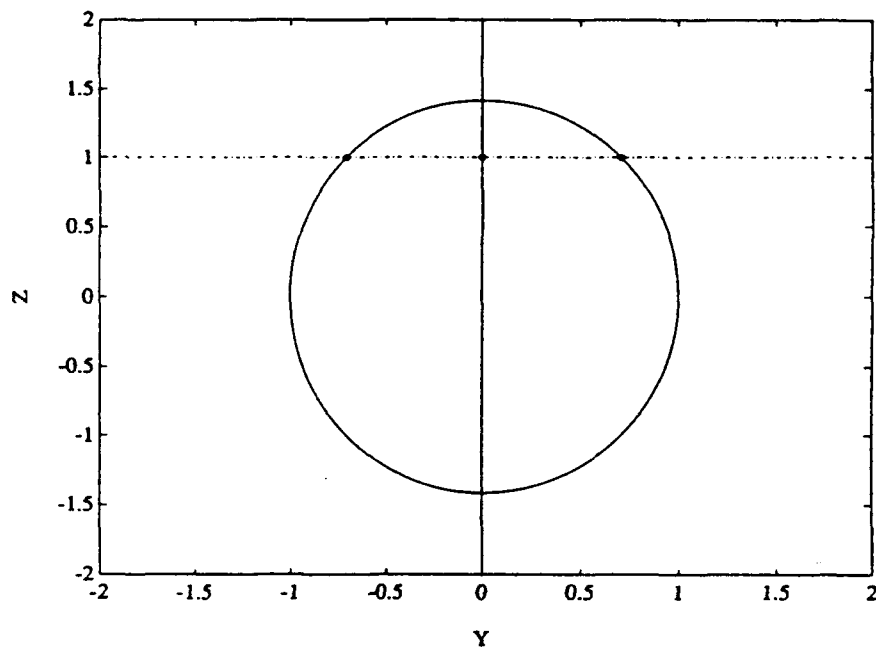


Figure 2.6: Possible steady configurations for a point vortex pair in a horizontally sheared flow. The steady configurations lie either on the Y axis, or on a circle of radius $(-q_b)^{-1/3}$ in (Y, Z) space. The 'o' symbols represent the three possible steady solutions for some fixed Z ($Z < (-q_b)^{-1/3}$).

solutions of this type exist. In this case the background shear is of the wrong sense to counterbalance the relative motions of the two vortices, and the only possible steady solutions are those with $Y_s = 0$.

For vertically sheared background flows the situation is somewhat different. In this case $q_b = 0$ and (2.10) may be written in the form

$$\frac{1}{\alpha Z_s^3} Y_s / Z_s = (1 + (Y_s / Z_s)^2)^{3/2}. \quad (2.13)$$

Thus the 'tilt' of the vortex (as measured by the quantity Y_s / Z_s) is a function of one parameter: $\frac{1}{\alpha Z_s^3}$, which is related to the ratio of U_{vortex} to $U_{\text{background}}$. Using well known properties of cubic equations ⁴, it can be shown that there are no real solutions when $(\frac{1}{\alpha Z_s^3})^2 < 27/4$, one when $(\frac{1}{\alpha Z_s^3})^2 = 27/4$, and two solutions in every other case. Notice that, in contrast to the case with horizontal shear, the sense of the background shear is not important, since changing the sign of α simply changes the sign of Y_s / Z_s . In the context of Figure 2.5c, this amounts to reflecting the entire plot about the X axis. On the other hand, Figures 2.5a,b show that changing the sign of q_b has a profound effect upon the qualitative behavior of the solutions.

Figure 2.7 shows the roots of (2.13) as a function of $\frac{1}{\alpha Z_s^3}$. Notice that the roots get farther apart as $\frac{1}{\alpha Z_s^3}$ increases. The smaller of the two roots represents a pair which becomes increasingly aligned in the vertical as $\frac{1}{\alpha Z_s^3}$ increases, corresponding to the center in Figure 2.5c. The larger root represents a pair which becomes increasingly tilted, and it corresponds to the saddle point in Figure 2.5c. The fact that there are two possible steady configurations is due to the special character of the point vortex flow field. Recall from Figure 2.2 that as one moves horizontally outward from the z axis at some level $z = z_0 \neq 0$, the azimuthal velocity first increases, then peaks and decreases monotonically to zero. Now, for a steadily translating configuration to exist, the tendency of the vortices to move with respect to one another must be precisely counterbalanced by the differential advection by the background flow. There will be two separation distances at which this

⁴This becomes a cubic equation for Y_s / Z_s , after squaring both sides.

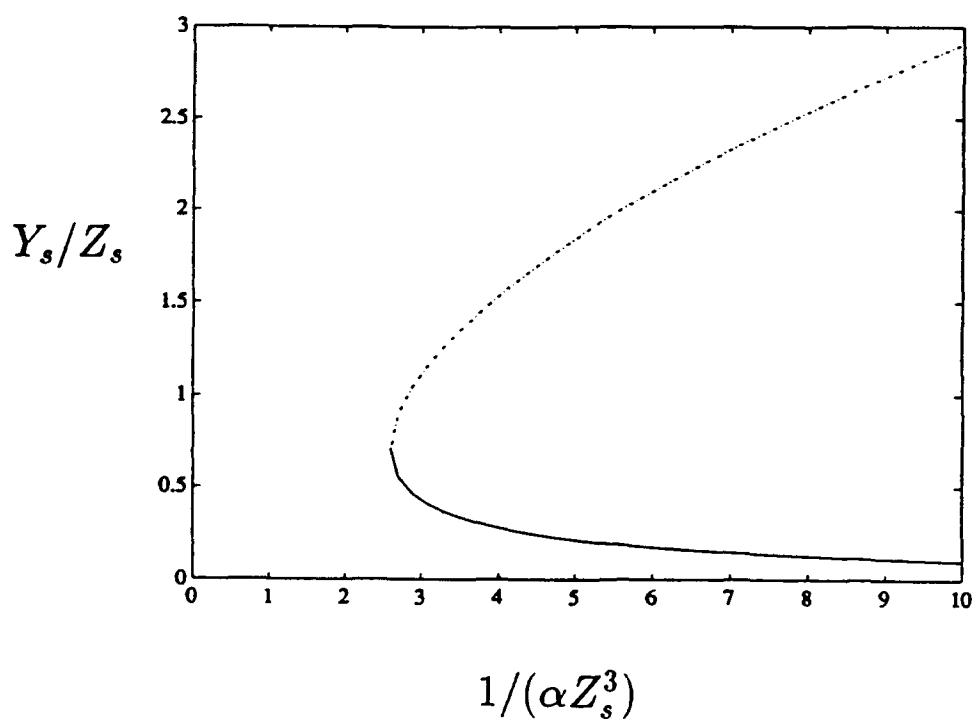


Figure 2.7: Roots of (2.13), representing steady configurations in a vertically sheared external flow. The vertical axis measures the tilt of the pair, while the horizontal axis is *inversely* proportional to the strength of the external shear. The upper (dashed) branch (representing strongly tilted pairs) represents unstable steady solutions, while the lower branch represents stable solutions. If the external shear is too large ($-\frac{1}{\alpha Z_s^3} < \sqrt{27/4}$), there are no steady solutions at all. Notice that along the stable branch the vortices get farther apart as the shear increases (assuming that the vertical separation Z , is fixed), while the opposite is true for the unstable branch.

can occur (provided that the shear is not too large), since the azimuthal velocity takes a given value at two different radial distances.

Stability Analysis

The stability properties of the steady solutions just discussed will now be examined. This analysis will allow a determination of the region of parameter space in which the solutions are realizable. Our approach will be to superimpose small perturbations on the steady solutions, and then to deduce whether the perturbations grow by solving linearized stability equations. Putting $X = X_s + X'$, $Y = Y_s + Y'$, $Z = Z_s + Z'$ in (2.6), there follows:

$$\begin{aligned}\dot{X}' &= -(Y_s + Y')/((X_s + X')^2 + (Y_s + Y')^2 + (Z_s + Z')^2)^{3/2} + \alpha(Z_s + Z') - q_b(Y_s + Y'), \\ \dot{Y}' &= +(X_s + X')/((X_s + X')^2 + (Y_s + Y')^2 + (Z_s + Z')^2)^{3/2}, \\ \dot{Z}' &= 0.\end{aligned}\tag{2.14}$$

Assuming that the perturbations are small (i.e., $X'^2 + Y'^2 + Z'^2 \ll X_s^2 + Y_s^2 + Z_s^2$), these may be written in the approximate form

$$\begin{aligned}\dot{X}' &\approx -\frac{(Y_s + Y')}{(X_s^2 + Y_s^2 + Z_s^2)^{3/2}}(1 - 3(X_s X' + Y_s Y' + Z_s Z')/R_s^2) + \alpha(Z_s + Z') - q_b(Y_s + Y'), \\ \dot{Y}' &\approx +\frac{(X_s + X')}{(X_s^2 + Y_s^2 + Z_s^2)^{3/2}}(1 - 3(X_s X' + Y_s Y' + Z_s Z')/R_s^2).\end{aligned}\tag{2.15}$$

Using the steady state balance (2.10) and discarding terms quadratic in perturbation quantities gives coupled, linearized evolution equations for X' and Y' :

$$\begin{aligned}\dot{X}' + \left(\frac{1}{R_s^3} - \frac{3Y_s^2}{R_s^5} + q_b\right)Y' &= \left(\alpha + \frac{3Y_s}{R_s^5}Z_s\right)Z' \\ \dot{Y}' - \frac{1}{R_s^3}X' &= 0.\end{aligned}\tag{2.16}$$

These may be combined to give

$$\begin{aligned}d^2 X'/dt^2 + \mu^2 X' &= 0, \\ d^2 Y'/dt^2 + \mu^2 Y' &= \frac{1}{R_s^3}\left(\alpha + \frac{3Y_s}{R_s^5}Z_s\right)Z', \\ \mu^2 &\equiv \frac{1}{R_s^6}(1 - 3Y_s^2/R_s^2 + q_b R_s^3),\end{aligned}\tag{2.17}$$

from which it follows that X' and Y' will be oscillatory if $\mu^2 > 0$, and will grow exponentially in time if $\mu^2 < 0$. The forcing term $\frac{1}{R_s}(\alpha + \frac{3Y_s}{R_s}Z_s)Z'$ does not affect the stability of the solutions, so in what follows we shall set $Z' = 0$. The stability of the system is thus governed by two dimensionless quantities: Y_s/R_s , measuring the tilt of the pair, and $q_b R_s^3$, which measures the jump in the background flow speed (U) between the two vortices. Although the expression for μ^2 does not explicitly contain α , the influence of vertical shear is implicit, as Y_s/R_s depends on α .

Because $0 < Y_s^2/R_s^2 = Y_s^2/(Y_s^2 + Z_s^2) \leq +1$, it follows immediately that all solutions are stable when $q_b R_s^3 > +2$, and are unstable when $q_b R_s^3 < -1$. Thus, vortex structures are apparently more readily destabilized by 'adverse' horizontal shears ($q_b < 0$), than by favorable shears (those for which $q_b > 0$). Recall from the last section that for flows with purely horizontal shear there are either one or three fixed points, depending on the sign of q_b (see Figure 2.5a). Whatever the sign of q_b , there is a root with $Y_s = 0$, corresponding to the case in which the vortices are vertically aligned. In this case $\mu^2 = (1 + q_b R_s^3)$, so the solution is unstable if $q_b R_s^3 < -1$. Therefore, this root is unstable only in strong adverse shears. When $q_b < 0$ there are two additional fixed points, which lie on a circle in (Y_s, Z_s) space, as shown in Figure 2.6. Their positions are given by $Y_s^2 = (\frac{1}{q_b})^{2/3} - Z_s^2$, and it is easy to show that in this case $\mu^2 = 3(Z_s^2(q_b)^{2/3} - 1)$. However, Figure 2.6 shows that $Z_s^2 \leq (1/q_b)^{2/3}$ for all solutions, so μ^2 is necessarily negative, and so these solutions are always unstable. This is consistent with the saddle point character of the top and bottom fixed points in Figure 2.5a. Thus, the *only* stable configuration in horizontal shear is the one in which one vortex is directly above the other.

For a vertically sheared background flow, α is nonzero, $q_b = 0$, and it follows from (2.8) that steady solutions are unstable if $Y_s^2/R_s^2 > 1/3$ (that is, if the vortex pair is too strongly tilted). Interestingly, the stability limit $Y_s^2/R_s^2 = 1/3$ describes configurations in which the vortices lie along the lines $z = \pm y\sqrt{2}$ in Figure 2.2. Thus, these lines are curves of marginal stability, and it follows that the sectors above and below the vortex

can be thought of as 'stability wedges', as there are no stable steady solutions for which the vortices lie outside of these wedges. From our earlier discussion of the character of the vortex flow field, it is apparent that outside the stable sectors ($Y_s^2/R_s^2 > 1/3$), the vortices interact less strongly when separated, while within these sectors ($Y_s^2/R_s^2 < 1/3$), they interact more strongly when separated slightly (the 'strength' of the interaction is measured by the speed of the relative motions of the two vortices caused by their mutual interactions).

We have demonstrated that steady configurations in vertical shear will be unstable if $Y_s^2/R_s^2 > 1/3$. However, it is not immediately obvious from (2.13) whether any solutions satisfying this inequality exist. To answer this question, notice that $Y_s^2/R_s^2 > 1/3$ implies that $Y_s/Z_s > \sqrt{1/2}$. A glance at Figure 2.7 shows that there are no real roots to (2.13) when $\frac{1}{\alpha Z_s^2} < \sqrt{27/4}$, and it is easily shown that $Y_s/Z_s = \sqrt{1/2}$ when $\frac{1}{\alpha Z_s^2} = \sqrt{27/4}$. Therefore, whenever $\frac{1}{\alpha Z_s^2} > \sqrt{27/4}$, Figure 2.7 shows that there is a root for which Y_s/Z_s is larger than $\sqrt{1/2}$, and another for which Y_s/Z_s is less than $\sqrt{1/2}$. Thus, the larger root represents a steady solution which is *always unstable*, corresponding to the saddle point in Figure 2.5c, while the smaller root represents a solution which is *always stable*, corresponding to the center in Figure 2.5c.

Propagation of the Point Vortex Pairs

Recall from (2.7) that the equations governing the translation of the *geometric* center of the pair are

$$\begin{aligned}\dot{\bar{x}} &= +\Delta Y/R^3 + \bar{u}_b \\ \dot{\bar{y}} &= -\Delta X/R^3.\end{aligned}$$

The first term on the right hand side represents the tendency of the vortex pair to propagate. Combining these with the equations governing the displacements (X, Y) (2.6), one obtains

$$\frac{d}{dt}(\bar{x} + \Delta X) = \bar{u}_b + \Delta U$$

$$\frac{d}{dt}(\bar{y} + \Delta Y) = 0. \quad (2.18)$$

Now, it can be shown that $\bar{x} + \Delta X$ is actually the x coordinate of the 'center of potential vorticity' of the component of the potential vorticity field due to the vortices themselves. Similarly, $\bar{y} + \Delta Y$ is the y coordinate of the center of potential vorticity, since it follows from the definitions of Δ , \bar{x} , \bar{y} , X , and Y that

$$\begin{aligned} (\bar{x} + \Delta X) &= \frac{Q_1 x_1 + Q_2 x_2}{Q_1 + Q_2} \equiv \langle x \rangle, \\ (\bar{y} + \Delta Y) &= \frac{Q_1 y_1 + Q_2 y_2}{Q_1 + Q_2} \equiv \langle y \rangle. \end{aligned} \quad (2.19)$$

Therefore, after employing the definitions of u_b and U , we find that the center of potential vorticity ($\langle x \rangle, \langle y \rangle$) moves according to

$$\begin{aligned} \frac{d}{dt} \langle x \rangle &= -q_b \bar{y} + \Delta(\alpha Z - q_b Y) \\ &= \Delta \alpha Z - q_b \langle y \rangle \\ \frac{d}{dt} \langle y \rangle &= 0. \end{aligned} \quad (2.20)$$

The second of these states that $\langle y \rangle$ is constant. It follows that $\langle x \rangle$ is a linear function of time, since the right hand side of (2.20a) is constant. Therefore, the center of vorticity of the pair must move with constant speed

$$u_0 = \Delta \alpha Z - q_b \langle y \rangle. \quad (2.21)$$

Notice that this is true for *all* solutions, not just steady ones – even if the vortices go around one another in some complicated fashion, their mutual center of potential vorticity moves in a straight line with constant speed. This can be clearly seen in Figure 2.3, where the dashed line shows the path of the center of potential vorticity. Finally, using the definitions of $\langle y \rangle$ and $\langle z \rangle$ (2.19) it is easy to show that

$$u_0 = u_b(\langle y \rangle, \langle z \rangle), \quad (2.22)$$

which shows that the speed of the pair is given by the background flow speed at the center of potential vorticity.

What is the physical mechanism which causes the vortex pairs to propagate? The translation is due to a modon-like propagation tendency of the dipolar component of the potential vorticity field. The modon character of the translation can be seen more clearly if propagation speed is written in terms of the separation of the pair. To do this, notice that for steadily translating configurations (2.6) shows that $\alpha Z - q_b Y = Y/R^3$, which simply says that in the steady limit the separation of the vortices is fixed by the external shear. Therefore, we may write

$$u_0 = \Delta Y/R^3 - q_b \bar{y} . \quad (2.23)$$

The first term on the right hand side represents the part of the translation speed which is due to the self interaction of the antisymmetric component of the potential vorticity field, while the second term represents a bulk advection by the background horizontal shear. The first term is most interesting, since it represents a modon-like propagation of the pair. When $Y \ll R$, c increases approximately linearly with Y due to the increasing interaction between the vortices. Thus if $Y \ll R$, an increase in the external shear requires a similar increase in Y for a steady balance to be maintained. This in turn leads to greater interaction between the vortices, and hence a larger propagation speed. Next, notice that $\Delta Y/R^3$ is precisely the propagation speed of an antisymmetric pair with strengths $\pm \Delta$ in a quiescent fluid. Thus, the vortex pairs can be thought of as monopoles with antisymmetric 'riders', which lead to propagation. The mechanism behind the propagation of unsteady vortex pairs is similar: the unsteady pairs have an *average* dipole moment which leads to propagation in a fixed direction.

Summary

A variety of solutions representing pairs of point potential vortices have been discussed. The vortex-vortex interactions combined with the influence of the imposed background flow on the vortex pair allow for a rich variety of possible behaviors. It was found that modon-like propagation can occur when the vortices are of opposite sign. The vortex pair may also translate with respect to the ambient fluid when the vortices

1

have the same sign, provided that there is a background flow of the appropriate form and an antisymmetric potential vorticity component. The propagation mechanism is the same in both cases: the antisymmetric component of the potential vorticity field causes the vortex pair to 'self propagate'. There is no inherent limit on the antisymmetry Δ of the pair. Changing Δ changes the translation speed of the vortex pair, but does not alter the shape or the stability properties of the solutions. The difference between propagation in a quiescent fluid and propagation in shear is that, in the latter case, a certain minimum symmetric component is needed to keep the vortices aligned (in a time average sense) with respect to the external flow. Solutions periodic in a translating reference frame were found for both horizontally and vertically sheared background flows. Stable, steadily translating solutions of this type exist in vertically sheared background flows, but not in horizontally sheared flows. In horizontal shear, all tilted configurations were found to be unstable. The point vortex solutions discussed here will be referred to often in the next chapter, when a model of a continuous vortex in an external shear is discussed. It will be seen that the point vortex pair often represents quite well the behavior of low mode disturbances on a continuous vortex.

Chapter 3

A Simple Model of a Quasigeostrophic Vortex in a Stratified Fluid

Introduction

In this chapter a simple model of a three dimensional quasigeostrophic vortex embedded in a uniformly sheared background flow will be examined. It is well known that steadily translating solutions can be found when $u \rightarrow 0$ as $r \rightarrow \infty$. A classic example of this in two dimensional flow is the 'Batchelor modon' (Batchelor, 1967, p. 535). In the present work, a related family of solutions is discussed, representing a lens-shaped quasigeostrophic vortex in a continuously stratified fluid. The propagating solutions have potential vorticity which varies with depth in the vortex core, which allows propagation if the core of the vortex is 'tilted' with respect to the vertical axis. A variety of steady and unsteady solutions will be discussed, representing translating and nontranslating vortex solutions. Initially, the case of a monopolar vortex in a quiescent fluid is addressed, then a uniform external shear is added, and finally the effect of baroclinic flow in the core is examined. The results show that both external vertical shear and depth variation of the potential vorticity within the core are necessary for vortex propagation, and that the propagation speed is proportional to the size of the boundary deformation. It is found that there is a limiting core baroclinicity beyond which no steady solutions exist. The results which will be discussed are linearized analytical solutions, and their validity requires that both the external shear and the deformation of the vortex boundary are small.

The approach taken will be to consider small perturbations superimposed on a basic state flow which is an exact steady solution to the potential vorticity equation. For flows characterized by a potential vorticity field which is piecewise constant in the horizontal, the entire flow field at each instant is determined by the position of the vorticity fronts, and it follows that the evolution of the entire flow field is determined by the motion of the front. To simplify the mathematics, the vortex is assumed to be of radius $R = ND/f_0$, where D is the half depth of the lens, N is the buoyancy frequency,

and f_0 the coriolis parameter, and it follows that the Burger number $S = N^2 D^2 / f_0^2 R^2$ is equal to one ¹. It follows that the model contains three independent parameters: b , q_b , and α , where b is a measure of the baroclinicity of the vortex, q_b is the potential vorticity of the background flow, and α measures the vertical shear of the external flow.

As discussed in Chapter 1, the motions of interest to us are governed by the f plane quasigeostrophic potential vorticity equation (see *e.g.* Pedlosky, 1979):

$$\partial_t q + \psi_x q_y - \psi_y q_x = 0, \quad (3.1)$$

where the quasigeostrophic potential vorticity field has the special form ²

$$q \equiv \psi_{xx} + \psi_{yy} + \psi_{zz} = q_b + q_v(z) \mathcal{H}(1 + \eta - r), \quad (3.2)$$

$$\psi \rightarrow \psi_b \quad \text{as } r \rightarrow \infty,$$

where r is the distance from the origin. Thus, (3.2) represents an isolated three dimensional patch with potential vorticity $q_b + q_v(z)$, in an external flow with potential vorticity q_b . Because η is assumed to be small, the vortex is almost spherical, as shown in Figure 3.1. In what follows $q_v(z)$ is chosen in the special form

$$q_v(z) = 1 + bz, \quad (3.3)$$

which may be thought of as a truncated expansion of a field with a more complicated z dependence. Notice that the choice (3.3) gives solutions which are cyclonic, even though it is well known that Meddies are anticyclonic vortices. This is primarily a notational convenience, as it is clear from (3.1) that re-scaling q merely alters the time scale of the problem.

It will be convenient to decompose the streamfunction ψ into three parts: $\psi = \psi^v + \psi' + \psi_b$, where ψ^v represents the pressure field of the unperturbed spherical vortex, ψ' gives the small anomalous pressure fluctuations associated with the deformation of the

¹As discussed in Chapter 1, when $S = 1$ an oblate spheroidal vortex will be spherical in transformed space, which allows the problem to be conveniently expressed in spherical coordinates.

² \mathcal{H} is the Heaviside step function: $\mathcal{H}(x) = 0$ if $x < 0$, $\mathcal{H}(x) = 1$ if $x > 0$.

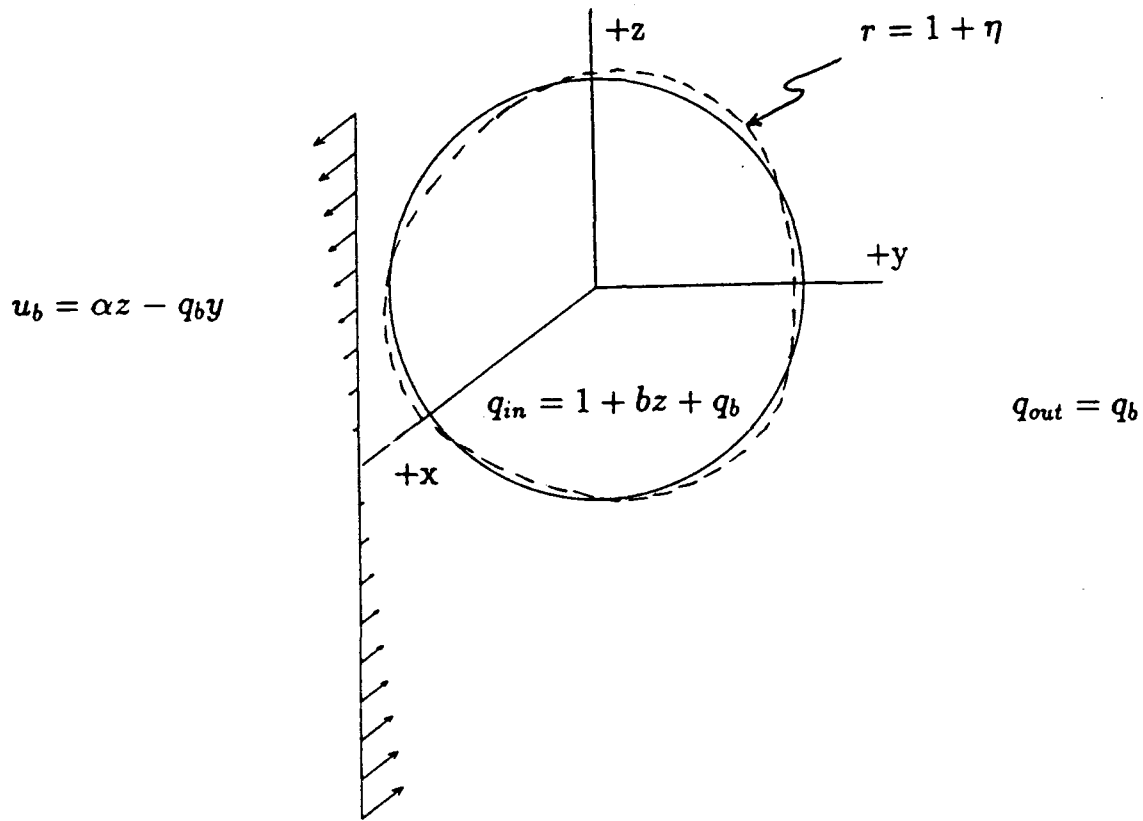


Figure 3.1: Schematic of a three dimensional quasigeostrophic vortex in a shear flow given by $u_b(y, z) = \alpha z - q_b y$. The boundary of the vortex departs from a unit sphere by the small amount $\eta(\theta, \phi, t)$. Inside the core the potential vorticity is given by $q = 1 + bz + q_b$; outside the core $q = q_b$.

boundary, and ψ_b is the pressure field associated with the background flow. ψ can then be found by solving for the three components ψ^v , ψ^b and ψ' separately. The potential vorticity field for the basic state vortex is chosen in the form

$$\begin{aligned}\nabla^2 \psi^v &= q_v(z) \mathcal{H}(1-r) \\ \psi^v &\rightarrow 0 \quad \text{as } r \rightarrow \infty,\end{aligned}\tag{3.4}$$

which represents a spherical vortex with potential vorticity $q = q_v(z)$ inside, $q = 0$ outside. Next, the streamfunction for the background flow ψ_b is defined by

$$\nabla^2 \psi_b = q_b = \text{a constant}.\tag{3.5}$$

Since the background flow is not required to vanish far from the the vortex, ψ_b will be a quadratic function of x, y , and z , and the associated flow will have constant shear. Using the above equations for ψ^v and ψ_b , it follows from (3.2) that the perturbation streamfunction must satisfy ³:

$$\begin{aligned}\nabla^2 \psi' &\equiv \nabla^2 \psi - \nabla^2 \psi^v - \nabla^2 \psi_b \\ &= q_b + q_v(z) \mathcal{H}(1+\eta-r) - q_v(z) \mathcal{H}(1-r) - q_b \\ &= \eta(\theta, \phi, t) q_v(z) \frac{\mathcal{H}(1+\eta-r) - \mathcal{H}(1-r)}{\eta} \\ &\sim \eta(\theta, \phi, t) q_v(z) \delta(r-1), \quad (\eta \rightarrow 0)\end{aligned}\tag{3.6}$$

$$\psi' \rightarrow 0 \quad \text{as } r \rightarrow \infty.$$

It can be readily verified that the solution to (3.4) is

$$\psi^v = \begin{pmatrix} r^2/6 - 1/2 \\ -1/3r \end{pmatrix} + b \begin{pmatrix} zr^2/10 - z/6 \\ -z/15r^3 \end{pmatrix} \quad \begin{matrix} r < 1 \\ r > 1 \end{matrix},\tag{3.7}$$

and the associated flow field is of the form

$$u^v(\theta) = \frac{1}{3}r \sin \theta \begin{pmatrix} 1 \\ 1/r^3 \end{pmatrix} + \frac{1}{10}br^2 \sin 2\theta \begin{pmatrix} 1 \\ 1/r^5 \end{pmatrix},\tag{3.8}$$

³The delta function notation in (3.6) may be understood if we consider $\delta(r-1)$ to be the limit as $\eta \rightarrow 0$ of a sequence of 'tophat' functions of width η and height η^{-1} .

where θ is in this case the polar angle (For the details of the calculation leading to (3.8), the reader is referred to Appendix 1.). Thus, the monopolar potential vorticity component is associated with a flow which is in solid body rotation within the core, and which decays like $1/r^2$ outside. The baroclinic potential vorticity component induces a vertically sheared flow within the core, which falls off like $1/r^3$ outside the core. Figure 3.2a shows a cross section of the basic state flow field for the case in which $b = 0$, and Figure 3.2b shows the flow field when $b = 1.0$. In Figure 3.2a the rotation frequency is the same at all depths inside the core; in Figure 3.2b the rotation frequency varies by a factor of four over the depth of the core.

Notice that $\nabla^2 \psi'$ vanishes everywhere except in the narrow region between $r = 1$ and $r = 1 + \eta$. In the limit as $\eta \rightarrow 0$, then, the problem of finding ψ' reduces to solving Laplace's equation in the regions $r < 1$ and $r > 1$ separately:

$$\nabla^2 \psi' = 0 \quad r < 1 \quad (3.9)$$

$$\nabla^2 \psi' = 0 \quad r > 1,$$

and then matching the two solutions across $r = 1$, so that (3.6) is satisfied. The appropriate matching conditions may be obtained by integrating the field equation (3.6) (written here in spherical coordinates) across the interface:

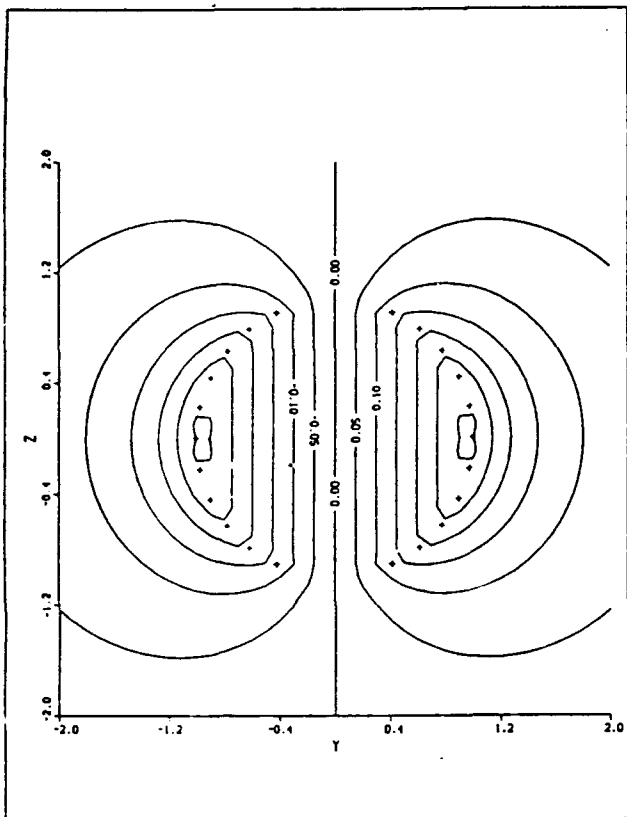
$$\begin{aligned} \int_{1-\epsilon}^{1+\epsilon} \frac{1}{r^2} ((r^2 \psi'_r)_r + \frac{1}{\sin \theta} (\sin \theta \psi'_\theta)_\theta + \frac{1}{\sin^2 \theta} \psi'_{\phi\phi}) dr &= \int_{1-\epsilon}^{1+\epsilon} \eta(\theta, \phi, t) q_v(z) \delta(r-1) dr \\ &= \eta(\theta, \phi, t) q_v(z). \end{aligned} \quad (3.10)$$

Letting $\epsilon \rightarrow 0$ gives the first matching condition

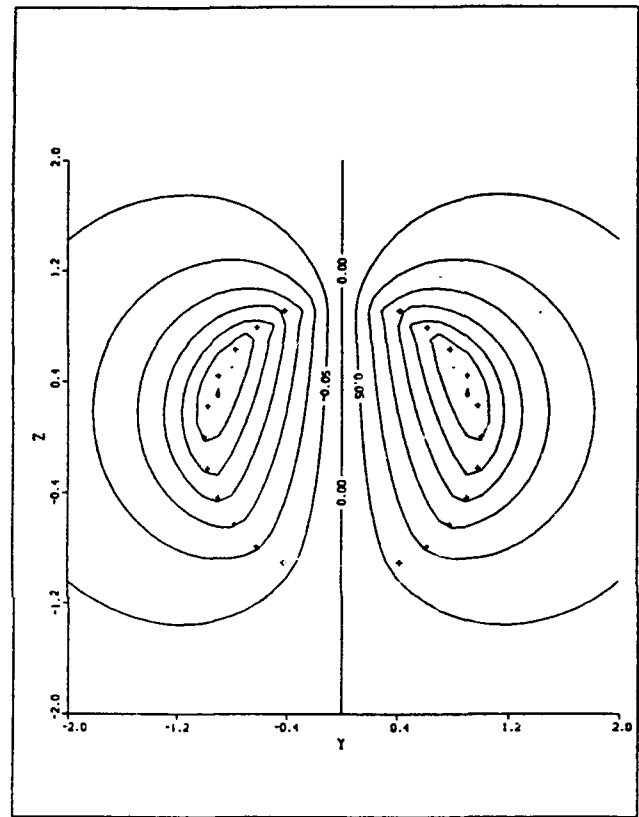
$$[\psi'_r]_{r=1} = \eta(\theta, \phi, t) q_v(z), \quad (3.11)$$

so that the gradient of the streamfunction is *discontinuous* across the surface $r = 1$. This condition guarantees that the total amount of anomalous potential vorticity remains constant as $\eta \rightarrow 0$, or, equivalently, that the velocity is continuous across the interface. A second integration gives the second matching condition

$$[\psi']_{r=1} = 0, \quad (3.12)$$



a



b

Figure 3.2: Contour plot showing basic state vortex flow field for $b = 0.0$ (a) and $b = 1.0$ (b). When $b = 0$ the core is in solid body rotation, while when $b > 0$ the rotation rate increases with z inside the core. In either case speeds in the far field decrease like $\sin(\theta)/r^2$, according to (3.8).

which ensures continuity of the pressure field.

As discussed in Chapter 1, a kinematic boundary condition must be applied on the vortex boundary to determine the evolution of the flow. This will ensure that the boundary of the vortex is a material interface. In a reference frame translating with constant speed u_0 , the kinematic condition is

$$B_t + (u - u_0)B_x + vB_y = 0 \quad \text{on } B = 0, \quad (3.13)$$

where the boundary is given by ⁴

$$B = 1 + \eta(\theta, \phi, t) - r = 0. \quad (3.14)$$

It will be convenient to rewrite (3.13) in a spherical coordinate system. Using the results $\partial_x = \sin \theta \cos \phi \partial_r + \frac{1}{r} \cos \theta \cos \phi \partial_\theta - \frac{1}{r} \frac{\sin \phi}{\sin \theta} \partial_\phi$, and $\vec{u} \cdot \vec{\nabla} B = (\hat{z} \times \vec{\nabla} \psi) \cdot \vec{\nabla} B = -\psi_\phi/r + \cot \theta \psi_\phi \eta_\theta / r^2 - (\cos \theta \psi_\theta / r + \sin \theta \psi_r) \eta_\phi / r \sin \theta$, it follows that (3.13) may be rewritten:

$$\begin{aligned} \eta_t + u_0(\sin \theta \cos \phi - \frac{1}{r} \cos \theta \cos \phi \eta_\theta + \frac{1}{r} \frac{\sin \phi}{\sin \theta} \eta_\phi) + \psi_\phi / r - \cot \theta \psi_\phi \eta_\theta / r^2 + \\ + (\cos \theta \psi_\theta / r + \sin \theta \psi_r) \eta_\phi / r \sin \theta = 0 \quad \text{on } B = 0. \end{aligned} \quad (3.15)$$

Recalling that $\psi = \psi^v + \psi' + \psi_b$, and invoking the scaling assumptions $\psi^v(\theta) = O(1)$, $u_0 \sim \eta \sim \psi' \sim \psi_b \ll 1$ ⁵, gives the linearized kinematic condition

$$\eta_t + u^v(\theta) \eta_\phi / \sin \theta + \psi'_\phi = -u_0 \sin \theta \cos \phi - \psi_{b,\phi} + O(\eta^2) \quad \text{on } r = 1, \quad (3.16)$$

where

$$u^v(\theta) = \cos \theta \psi_\theta^v + \sin \theta \psi_r^v.$$

Equation (3.16) simply states that in a frame of reference translating with speed u_0 , the rate of change of η following the basic flow is balanced by the flow normal to the boundary, which is due to the combined effects of the external flow and the uniform translation.

⁴ η is thus constrained to be a single-valued function of θ and ϕ .

⁵This assumes that η and ψ' don't vary too rapidly in θ and ϕ .

Notice that (3.15) is to be applied on the boundary $r = 1 + \eta$ of the vortex, while (3.16) is applied on $r = 1 - \eta$ - the boundary of the basic state vortex. This simplification can be justified by expanding each of the terms in (3.15) in a Taylor series in r , and neglecting terms of $O(|\eta|^2)$. The terms representing the external flow and the translation effect appear as a forcing on the right hand side of (3.16), and hence they fix the magnitude of the boundary deformation ⁶. Finally, note that the value of u_0 has *not* been specified, and it might therefore seem that we could choose any value we liked for u_0 . However, it turns out that the translation speed is related to integral properties of the potential vorticity distribution, and it is fully determined once α and b are specified. u_0 will be determined shortly as a solvability requirement for our solution expansion, and found to depend linearly upon both the shear α and the baroclinicity b .

Normal Modes on a Spherical Vortex

In this section the behavior of a monopolar vortex ($b = 0$) in a fluid at rest at infinity will be examined. The basic state potential vorticity field is thus of the form

$$q_v = \mathcal{H}(1 + \eta - r). \quad (3.17)$$

As there is no imposed background flow, we may without loss of generality set

$$\psi_b = 0, \quad (3.18)$$

and with $b = 0$, the basic state vortex streamfunction (3.7) becomes

$$\psi^v = \begin{cases} r^2/6 - 1/2 & r < 1 \\ -1/3r & r > 1 \end{cases}. \quad (3.19)$$

The associated basic state flow field is of the form

$$\vec{u}^v = \frac{1}{3} r \sin \theta \begin{pmatrix} 1 \\ 1/r^3 \end{pmatrix} \hat{\phi} \quad \begin{matrix} r < 1 \\ r > 1 \end{matrix}, \quad (3.20)$$

⁶Without these terms, (3.16) is homogeneous in η , as it may be written as a forced integro-differential equation for η :

$$\eta_t + (\cos \theta \psi_\theta^v + \sin \theta \psi_r^v) \eta_\phi / \sin \theta + \partial_\phi \int \int_{\text{sphere}} G(\vec{r} | \vec{r}_0) \eta q \sin \theta_0 d\theta_0 d\phi_0 = -u_0 \sin \theta \cos \phi - \psi_{b,\phi}.$$

so that the core is in solid body rotation, with speeds decreasing rapidly outside the core (see Figure 3.2a).

The equation for the perturbation streamfunction ψ' is given by (3.9), with the matching conditions

$$[\psi'_r]_{r=1} = \eta(\theta, \phi, t), \quad (3.21)$$

$$[\psi']_{r=1} = 0.$$

Because $\psi_b = \psi'_\theta = 0$, the kinematic condition takes the simple form

$$\eta_t + \psi'_\phi + \psi'_r \eta_\phi = -u_0 \sin \theta \cos \phi \quad \text{on } r = 1. \quad (3.22)$$

The spherical geometry of the problem posed by (3.9), (3.21), and (3.22) suggests an expansion in terms of spherical harmonics, so we look for solutions of the form

$$\psi' = \sum_{n=0}^{\infty} \sum_{m=-n}^n R_{mn}(r) Y_n^m(\theta, \phi) e^{-i\omega t} \quad (3.23)$$

$$\eta = \sum_{n=0}^{\infty} \sum_{m=-n}^n c_{mn} Y_n^m(\theta, \phi) e^{-i\omega t}.$$

The problem then reduces to one of choosing the complex expansion coefficients R_{mn} and c_{mn} such that (3.21) and (3.22) are satisfied. Notice that the spherical harmonics are defined by

$$Y_n^m(\theta, \phi) = \sqrt{\frac{2n+1}{4\pi} \frac{(n-m)!}{(n+m)!}} P_n^m(\cos \theta) e^{im\phi}, \quad (3.24)$$

where the P_n^m are associated Legendre polynomials. The superscript m therefore determines the azimuthal (ϕ) behavior of a harmonic, while the polar (θ) structure depends on both m and n . For future reference, the first few spherical harmonics are listed here:

$$\begin{aligned} Y_1^1 &= -\sqrt{\frac{3}{8\pi}} \sin \theta e^{i\phi} \\ Y_1^{-1} &= +\sqrt{\frac{3}{8\pi}} \sin \theta e^{-i\phi} \\ Y_2^1 &= -3\sqrt{\frac{5}{24\pi}} \sin \theta \cos \theta e^{i\phi} \\ Y_2^{-1} &= +3\sqrt{\frac{5}{24\pi}} \sin \theta \cos \theta e^{-i\phi} \end{aligned} \quad (3.25)$$

$$Y_2^2 = +3\sqrt{\frac{5}{96\pi}} \sin^2 \theta e^{2i\phi}$$

$$Y_2^{-2} = +3\sqrt{\frac{5}{96\pi}} \sin^2 \theta e^{-2i\phi}.$$

For further information concerning spherical harmonics, the reader is referred to the excellent discussion in the book by Arfken (1966).

Putting (3.23) into (3.9) gives an equation for the R_{mn} :

$$r^2 R_{mn}'' + 2r R_{mn}' - n(n+1)R_{mn} = 0, \quad (3.26)$$

which has the solution

$$R_{mn} = A_{mn}^+ r^{k_+} + A_{mn}^- r^{k_-}, \quad (3.27)$$

$$k_{\pm} \equiv (-1 \pm \sqrt{1 + 4n(n+1)})/2 = -\frac{1}{2} \pm (n + \frac{1}{2}).$$

It follows that the solution to (3.9) which is continuous across $r = 1$ (and which is everywhere bounded) may be written in the form

$$\psi' = \sum_{n=0}^{\infty} \sum_{m=-n}^n A_{mn} \begin{pmatrix} r^{k_+(n)} \\ r^{k_-(n)} \end{pmatrix} Y_n^m(\theta, \phi) e^{-i\omega t} \quad \begin{matrix} r < 1 \\ r > 1 \end{matrix}. \quad (3.28)$$

The next step is to satisfy the derivative condition in (3.21). Putting the expression for the streamfunction into (3.21) and setting $r = 1$ gives

$$\sum_{n=0}^{\infty} \sum_{m=-n}^n A_{mn} (k_- - k_+) Y_n^m(\theta, \phi) e^{-i\omega t} = \sum_{n=0}^{\infty} \sum_{m=-n}^n c_{mn} Y_n^m(\theta, \phi) e^{-i\omega t}. \quad (3.29)$$

Multiplying both sides by $Y_n^{m'*}$ and integrating over the surface of the sphere gives

$$-A_{mn}(2n+1) = c_{mn}, \quad (3.30)$$

so there is a very simple relationship between the expansion coefficients for ψ' and those for η . Putting (3.30) into (3.28) gives:

$$\psi' = -\sum_{n=0}^{\infty} \sum_{m=-n}^n \frac{c_{mn}}{2n+1} \begin{pmatrix} r^{k_+(n)} \\ r^{k_-(n)} \end{pmatrix} Y_n^m(\theta, \phi) e^{-i\omega t} \quad \begin{matrix} r < 1 \\ r > 1 \end{matrix}. \quad (3.31)$$

Putting the expressions for ψ' and η into the kinematic condition (3.22) gives

$$(-\omega - \frac{m}{2n+1} + \frac{1}{3}m)ic_{mn}e^{-i\omega t} + \int \int_{\text{sphere}} u_0 \sin \theta \cos \phi Y_n^{m*} d\sigma = 0. \quad (3.32)$$

Evaluating the integral in (3.32) (see Appendix 3 for the details) gives

$$\int \int_{\text{sphere}} u_0 \sin \theta \cos \phi Y_n^{m*} d\sigma = u_0 \sqrt{2\pi/3} (\delta_{m,-1} - \delta_{m,+1}) \delta_{n,1}, \quad (3.33)$$

where $\delta_{m,n}$ is the Kronecker delta function, defined by $\delta_{m,n} = 1$ when $m = n$, $\delta_{m,n} = 0$ if $m \neq n$. Notice that this integral does not depend on time, and it is only nonzero when $m = \pm 1$, $n = 1$. When the integral is nonzero, it appears that there must be a steady component to the response to counterbalance it. However, putting $\omega = 0$, $m = n = 1$ shows that (3.32) can *only* be satisfied if $u_0 = 0$. It follows that all modes must obey the dispersion relation

$$\frac{\omega}{m} = \frac{1}{3} - \frac{1}{2n+1}, \quad (3.34)$$

where m and n are integers

$$m = 0, \pm 1, \pm 2, \pm 3, \dots, \pm n$$

$$n = 0, 1, 2, 3, \dots$$

Notice that ω is always *real*, so that there are no exponentially growing modes, *i.e.*, the basic state vortex is linearly stable. The normal mode dispersion relation is plotted in Figure 3.3. The first term on the right hand side of (3.34) represents the advection by the basic state vortex flow field, while the second term represents the propagation tendency of the modes with respect to the basic flow. The normal modes try to propagate *against* the basic state flow, with the lowest ($n = 1$) mode stationary, and with higher modes being increasingly carried along by the mean flow. Finally, all $m = 0$ modes are symmetric about the z axis, and (3.34) shows that they must therefore be stationary. It follows that any vortex with a boundary which is axisymmetric about the vertical axis will be an exact steady solution, as it may be synthesized from the $m = 0$ modes. The shapes of the first few normal mode boundary perturbations are sketched in Figure 3.4.

The $(1, 2)$ mode is associated with boundary perturbations of the form $\eta = c_{12} Y_2^1 + c_{-12} Y_2^{-1} \sim \sin 2\theta \sin \phi$, and may be thought of as the continuous analog of the point

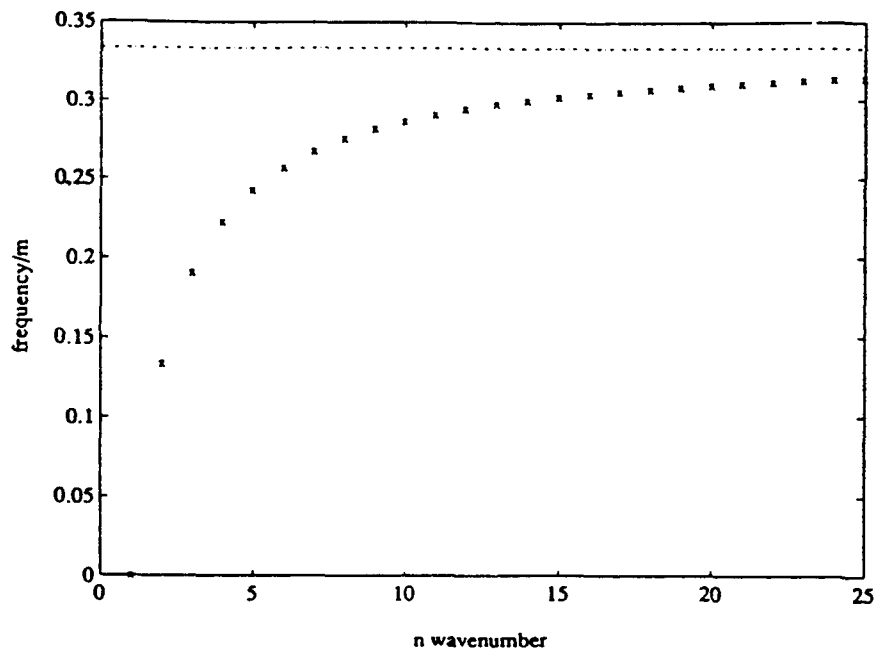
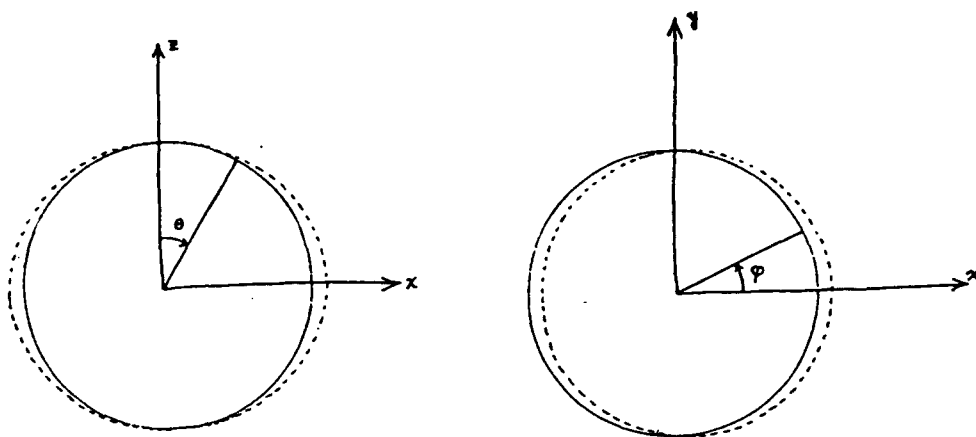
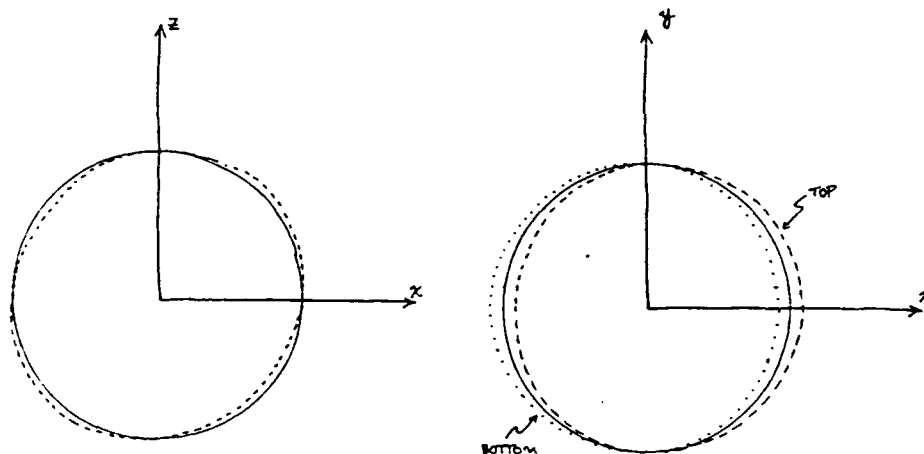


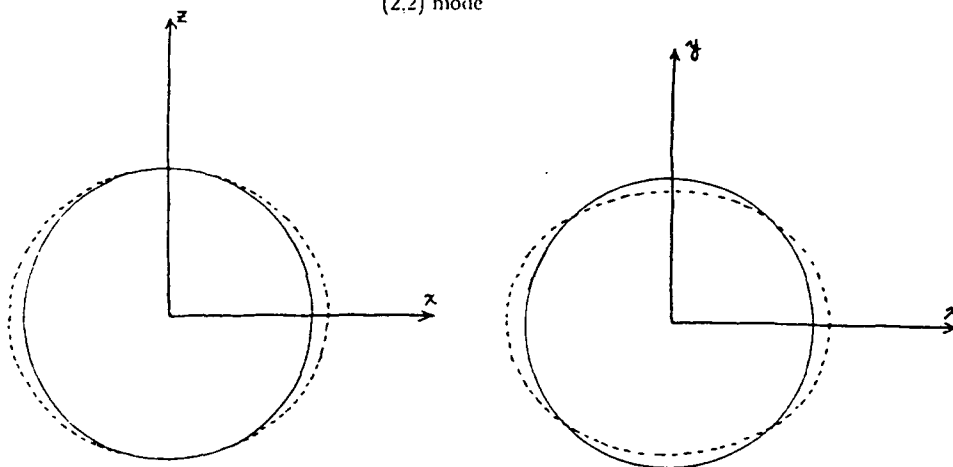
Figure 3.3: Normal mode dispersion relation: $\frac{\omega}{m} = \frac{1}{3} - \frac{1}{2n+1}$. The normal modes propagate against the basic state flow. The $n = 1$ mode is stationary, since its propagation speed exactly counterbalances the advection by the basic flow. Higher modes propagate more slowly, and are thus increasingly carried along by the basic state flow.



(1,2) mode



(2,2) mode



Side View

Top View

Figure 3.4: The shapes of the first few spherical harmonic boundary perturbations $\eta_n^m \sim c_{mn} Y_n^m + c_{-mn} Y_n^{-m}$. The orientation of the boundary perturbations in the (x, y) plane is determined by the phase of the complex expansion coefficients. Here we have arbitrarily chosen these such that the deformed vortex is aligned with the z axis. Superimposing the (1, 1) mode on a unit sphere simply shifts the basic state vortex horizontally, giving a shifted sphere. Superimposing the (1, 2) mode gives a 'tilted' sphere, while the (2, 2) mode produces an ellipsoidal perturbation. As drawn here, $\eta_1^1 \sim \sin \theta \cos \phi$, $\eta_2^1 \sim \sin 2\theta \cos \phi$, and $\eta_2^2 \sim \sin^2 \theta \cos 2\phi$.

vortex solution discussed in Chapter 2. The point vortex analog consists of a pair of point vortices of equal strength at different depths, which are initially 'tilted' from the vertical. The tilted vortex pair rotates steadily about a vertical axis, just as the boundary perturbation does in the continuous model. The higher mode disturbances do not have direct analogs in the point vortex model for the simple reason that there aren't enough point vortices to adequately represent their structure.

A Monopolar Vortex in External Shear: Steady States

The results of the last section will now be generalized to include the effects of a background flow with constant horizontal and vertical shear. The streamfunction of the background flow is chosen to be of the form

$$\psi_b = -\alpha yz + \frac{1}{2}q_b y^2, \quad (3.35)$$

which represents a zonal flow with constant shear given by

$$u_b = \alpha z - q_b y. \quad (3.36)$$

Notice that the average flow speed over the core region ($r \leq 1$) is precisely zero, so there cannot be a bulk advection of the vortex by the background flow.

The form of the basic state streamfunction ψ^v , and the equation for ψ' are the same as in the last section, so that part of the calculation will be skipped. The difference shows up in the kinematic condition, which takes the form

$$\eta_t + \psi_r^v \eta_\phi + \psi'_\phi + \psi_{b,\phi} + u_0 \sin \theta \cos \phi = 0 \quad \text{on } r = 1. \quad (3.37)$$

As before, the solutions are assumed to be of the form

$$\begin{aligned} \psi' &= \sum_{n=0}^{\infty} \sum_{m=-n}^n R_{mn}(r) Y_n^m(\theta, \phi) e^{-i\omega t} \\ \eta &= \sum_{n=0}^{\infty} \sum_{m=-n}^n c_{mn} Y_n^m(\theta, \phi) e^{-i\omega t}, \end{aligned}$$

and after making use of the orthogonality properties of the spherical harmonics, there follows

$$(-i\omega c_{mn} + imA_{mn} + \frac{1}{3}imc_{mn})e^{-i\omega t} + \int \int_{\text{sphere}} (u_0 \sin \theta \cos \phi + \psi_{b,\phi}) Y_n^{m*} d\sigma = 0. \quad (3.38)$$

Making use of the derivative jump condition (3.21) from the last section, this may be rewritten in the form

$$\left(-\omega - \frac{m}{2n+1} + \frac{1}{3}m\right)ic_{mn}e^{-i\omega t} + \int \int_{\text{sphere}} (u_0 \sin \theta \cos \phi + \psi_{b,\phi})Y_n^{m*} d\sigma = 0. \quad (3.39)$$

There are two cases which need to be examined. First consider the case in which m and n are chosen such that the integral in (3.39) vanishes. This implies that the background flow does not project onto the spherical harmonic Y_n^m . For the background flow considered here this happens when $n > 2$. In this case the expression in parentheses on the left side of (3.39) must also vanish. Comparing this with (3.34) shows that these modes satisfy the dispersion relation for free modes on a sphere found in the last section, and thus are unaffected by the external flow. Because these modes are unforced, their amplitudes are completely arbitrary. It is clear that a solution may contain an arbitrary number of such modes, and the combination of these modes constitutes the homogeneous solution to the problem. If the integral does not vanish, then the response must also contain a steady component to balance this term, since the integral is independent of time. The forced response is described by (3.39), with ω set equal to zero

$$\left(\frac{1}{3} - \frac{1}{2n+1}\right)imc_{mn} + \int \int_{\text{sphere}} (u_0 \sin \theta \cos \phi + \psi_{b,\phi})Y_n^{m*} d\sigma = 0, \quad (3.40)$$

so the coefficients for the forced component of the response are uniquely determined by the background flow. Recalling the definition of ψ_b , the integral in (3.40) may be evaluated (see Appendix 3) to get:

$$\begin{aligned} \int \int_{\text{sphere}} (u_0 \sin \theta \cos \phi + \psi_{b,\phi})Y_n^{m*} d\sigma &= u_0 \sqrt{2\pi/3}(\delta_{m,-1} - \delta_{m,+1})\delta_{n,1} + \\ &+ \frac{1}{3}\alpha \sqrt{6\pi/5}(\delta_{m,1} - \delta_{m,-1})\delta_{n,2} + \frac{1}{12}q_b i \sqrt{96\pi/5}(\delta_{m,-2} - \delta_{m,+2})\delta_{n,2}, \end{aligned} \quad (3.41)$$

where the primes have been dropped. Thus, only the $m = \pm 1, \pm 2$, $n = 1, 2$ harmonics will 'feel' the background flow. Notice that when $n = 1$ the first term on the left side of (3.40) vanishes, while (3.41) shows that the integral contributes a term proportional to u_0 . Clearly, the only way that the equality can be satisfied is if u_0 vanishes, implying that the vortex does not translate.

Now the form of the boundary deformations induced by the external flow will be examined. As we are concerned here with the equilibrium response of the vortex, only modes which are directly forced by the external shear will be discussed. Specifically, the free modes discussed in the last paragraph will not be considered. Using (3.40) and (3.41), it is easy to solve for the coefficients $c_{\pm 1,2}$, $c_{\pm 2,2}$ in terms of the background flow parameters:

$$\begin{aligned} c_{12} &= c_{-12} = +\frac{5}{2}i\alpha\sqrt{6\pi/5} \\ c_{22} &= c_{-22} = +\frac{5}{16}q_b\sqrt{96\pi/5}. \end{aligned} \quad (3.42)$$

The form of the boundary perturbation is given by

$$\eta_F = c_{12}Y_2^1 + c_{-12}Y_2^{-1} + c_{22}Y_2^2 + c_{-22}Y_2^{-2}. \quad (3.43)$$

After a bit of manipulation we find that the deformation induced by the external flow is of the form

$$\eta_F = +\frac{15}{4}\alpha \sin 2\theta \sin \phi + \frac{15}{8}q_b \sin^2 \theta \cos 2\phi, \quad (3.44)$$

where the vortex boundary is of course given by $r = 1 + \eta_F$. The term proportional to α causes the core to 'tilt' at right angles to the external flow. The direction of the tilt is determined by the sign of α . The term proportional to q_b represents an ellipsoidal perturbation which is associated with the external horizontal shear. The major axis for this deformation may be either parallel or perpendicular to the external flow, depending on the sign of q_b . The shape of these boundary deformations is sketched in Figure 3.5.

The shapes of the steady solutions shown in Figure 3.5 can be understood by considering the pressure field due to the background flow on the surface $r = 1$. In a study of two layer vortices in shear, Yano and Flierl (*in press*) found that the steady boundary shapes were determined by two competing effects: (1) the adjustment of the boundary in response to the externally imposed pressure field, and (2) the adjustment of the perturbation flow in response to the deformation of the boundary. They found that the nature of the boundary deformation depended upon which of these two effects was

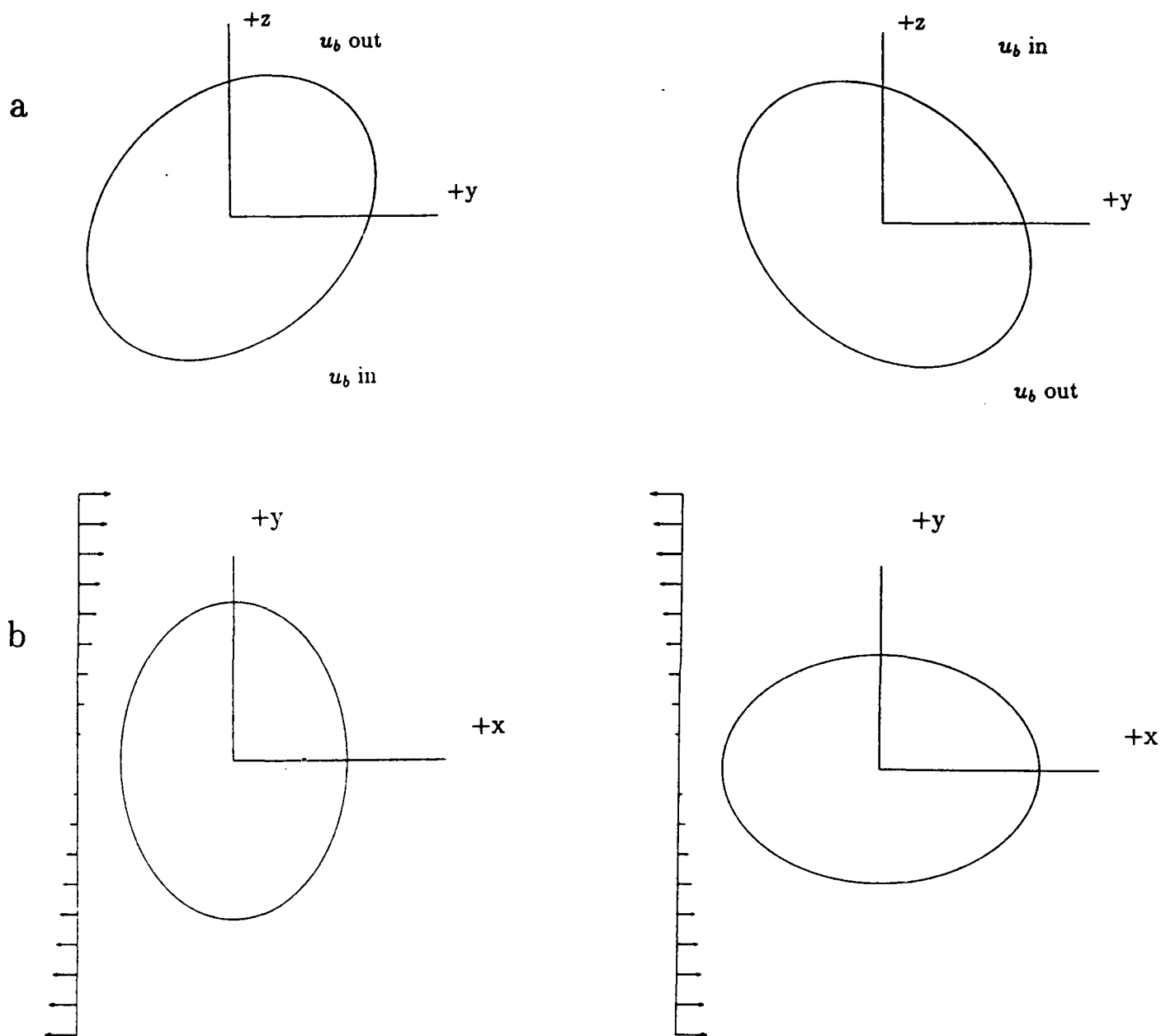


Figure 3.5: Sketch of the possible steady state boundary perturbations for a monopolar vortex ($b = 0$) in an external flow with constant shear. 5a shows the case in which the external flow is vertically sheared, and the vortex is 'tilted' in a direction perpendicular to the background flow. The direction of tilt is determined by the sign of the external vertical shear. 5b shows the horizontally sheared case (viewed from above). In this case the boundary deformation is ellipsoidal, and the orientation of the ellipsoid with respect to the x, y axes is determined by the sign of the external shear.

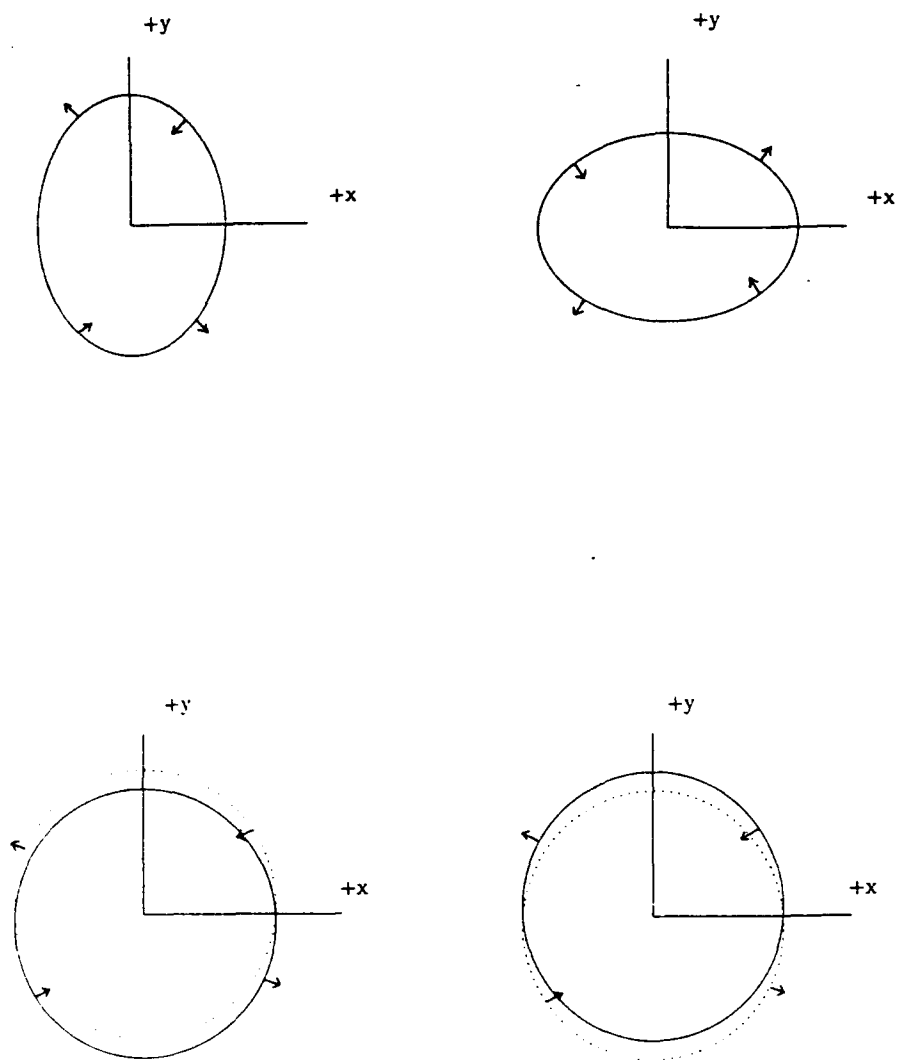
larger. For vortices which were small compared to the deformation radius the first effect dominated, while for large vortices the second effect was most important. In the present work the model vortex is 'small' ($R = ND/f_0$), and the first effect determines the shape of the boundary in the steady limit. Thus, the boundary shape can be predicted by considering the pressure field associated with the background flow. In the steady limit, the pressure at any depth is constant on the vortex boundary. Therefore, if the external flow induces a negative pressure anomaly at some point on the surface ($r = 1$), then the steady boundary shape is obtained (qualitatively) by moving the boundary of the vortex in the direction of lower external pressures. In the context of Figure 3.5a this implies that a cyclonic eddy in vertical shear will tend to 'tilt' toward lower external pressures. The relationship between the pressure field ψ_b and the boundary deformation can be shown more clearly if η_F is written in the form:

$$\eta_{F,\phi} = -\psi_{b,\phi} / \left(\frac{1}{3} - \frac{1}{2n+1} \right), \quad (3.45)$$

where we have used (3.19), (3.37), and (3.30), together with fact that the motion is steady and the vortex does not translate ($u_0 = 0$). Integrating once in ϕ shows that for a given n , η_F is proportional (to within an arbitrary function of theta) to the negative of the external pressure field ψ_b .

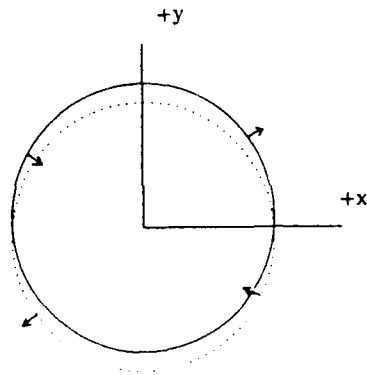
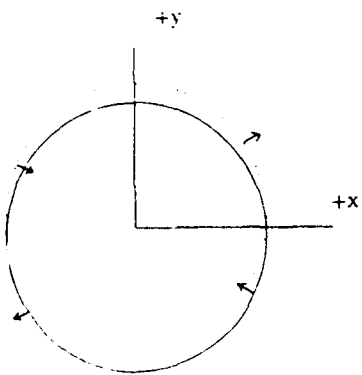
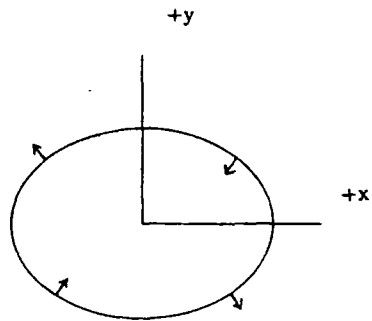
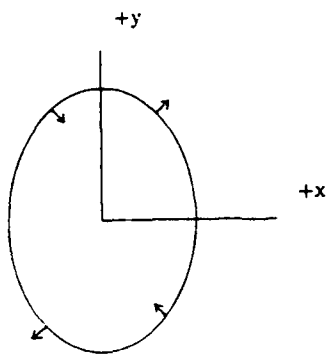
Alternatively, the steady boundary shapes can be understood by considering *separately* the precession tendency of the vortex, and the tendency of the external flow to deform the boundary. With no external flow, each of the vortices in Figure 3.5 will precess in a cyclonic sense ⁷. In Figure 3.6a the arrows show the precession tendency for the four solutions in Figure 3.5. For the vertical shear solutions the solid line shows a horizontal cross section of the vortex core near the top; the dashed line shows a horizontal section near the bottom. Figure 3.6b illustrates the tendency of the external flow to deform the boundary for each of the vortices shown in Figure 3.5. In this case the arrows represent the normal component of the external flow field at a given point on the

⁷Although the wave propagates in an anticyclonic sense *relative to the fluid*, the strong cyclonic flow in the core overwhelms this effect, leading to a cyclonic precession.



a

Figure 3.6: Plot showing how the steady solutions in Figure 3.5 can be understood in terms of a balance between the natural tendency of the vortices to precess cyclonically, and the advection of the vortex boundary by the external flow. In Figure 3.6a the arrows show the precession tendencies for the four solutions shown in Figure 3.5; in 3.6b the arrows show the sense of the normal component of the external flow field for these solutions. A comparison of 3.6a and 3.6b shows how the two effects can cancel in the steady limit.



b

boundary. A comparison of Figure 3.6a with 3.6b shows that the tendency of the core to precess cyclonically tends to offset the effect of the advection of the boundary by the external flow. In the steady limit these effects exactly counterbalance one another.

A Baroclinic Vortex in Shear: Translation

In this section the behavior of a baroclinic vortex in a uniformly sheared background flow is examined. The baroclinic core introduces the possibility of propagation with respect to the external fluid, as was found for the baroclinic point vortex pairs in Chapter 2. Because this propagation is perhaps the most fundamental result of this section, attention will be focused on the mechanisms responsible for it. In the present model, propagation is a consequence of the interaction between the external vertical shear and the depth dependent potential vorticity in the core. Thus, the majority of the discussion will be directed toward the influence of vertical (rather than horizontal) shear. The potential vorticity of the model vortex is given by $q_v(z) = 1 + bz$, and it is easy to show that the associated streamfunction is of the form:

$$\psi^v = \begin{pmatrix} r^2/6 - 1/2 \\ -1/3r \end{pmatrix} + b \begin{pmatrix} zr^2/10 - z/6 \\ -z/15r^3 \end{pmatrix} \begin{matrix} r < 1 \\ r > 1 \end{matrix} . \quad (3.46)$$

It is shown in Appendix 1 that the flow in the core associated with this streamfunction is given by

$$\vec{u}^v = \left(\frac{1}{3} + \frac{1}{5}bz \right) r \sin \theta \hat{\phi} . \quad (3.47)$$

This shows that the circulation in the core may be of the same sign everywhere even if the potential vorticity changes sign ($|b| > 1$). The circulation does not change sign unless $|b| > 5/3$.

In solving for the perturbation quantities, it is again assumed that separable solutions exist of the form

$$\psi' = \sum_{n=0}^{\infty} \sum_{m=-n}^n R_{mn}(r, t) Y_n^m(\theta, \phi) , \quad (3.48)$$

$$\eta = \sum_{n=0}^{\infty} \sum_{m=-n}^n c_{mn}(t) Y_n^m(\theta, \phi) .$$

Notice that the expansion coefficients c_{mn} and R_{mn} are explicit functions of time. Putting (3.48) into (3.9) gives an equation for the R_{mn} :

$$r^2 R''_{mn} + 2r R'_{mn} - n(n+1)R_{mn} = 0, \quad (3.49)$$

so that the R_{mn} are given (as in (3.27)) by

$$\begin{aligned} R_{mn} &= A_{mn}^+ r^{k_+} + A_{mn}^- r^{k_-}, \\ k_{\pm} &\equiv -\frac{1}{2} \pm (n + \frac{1}{2}). \end{aligned} \quad (3.50)$$

The solution which is continuous across the boundary may be written

$$\psi' = \sum_{n=0}^{\infty} \sum_{m=-n}^n A_{mn} \begin{pmatrix} r^{k_+(n)} \\ r^{k_-(n)} \end{pmatrix} Y_n^m(\theta, \phi) \quad \begin{matrix} r < 1 \\ r > 1 \end{matrix}, \quad (3.51)$$

where the A_{mn} must be determined such that the velocity field is continuous across the boundary. This is done by putting the expression for ψ' into (3.11) and setting $r = 1$, which gives the additional constraint:

$$\sum_{n=0}^{\infty} \sum_{m=-n}^n A_{mn} (k_- - k_+) Y_n^m(\theta, \phi) = q_v(z) \sum_{n=0}^{\infty} \sum_{m=-n}^n c_{mn} Y_n^m(\theta, \phi). \quad (3.52)$$

Multiplying both sides by $Y_n^{m'*}$ and integrating over the surface of the sphere gives

$$-A_{m'n'}(k_+(n') - k_-(n')) = \sum_{n=0}^{\infty} \sum_{m=-n}^n c_{mn} \int \int (1 + b \cos \theta) Y_n^m Y_n^{m'*} d\sigma, \quad (3.53)$$

which leads to

$$\begin{aligned} -A_{m'n'}(2n' + 1) &= c_{m'n'} + b \{ c_{m',(n'+1)} \sqrt{\frac{(n' - m' + 1)(n' + m' + 1)}{(2n' + 1)(2n' + 3)}} + \\ &+ c_{m',(n'-1)} \sqrt{\frac{(n' - m')(n' + m')}{(2n' - 1)(2n' + 1)}} \}, \end{aligned} \quad (3.54)$$

where the integration of the right hand side was performed using the result found in Arfken (p. 456). Thus, (3.51) satisfies the equation for ψ' (3.6) as long as the A_{mn} and the c_{mn} are related by (3.54).

To solve for ψ' or η , an additional relation is needed between the c_{mn} and the A_{mn} . This is provided by the kinematic condition, i.e., by the requirement that the

vortex boundary be a material surface. The linearized kinematic condition for unsteady motions in a reference frame translating with constant speed u_0 is

$$u_0 \sin \theta \cos \phi + \psi'_\phi + \psi_{b,\phi} + \eta_t + (\cos \theta \psi_\theta^v + \sin \theta \psi_r^v) \eta_\phi / \sin \theta = O(\eta^2). \quad (3.55)$$

Substituting the expansions for η and ψ' into the kinematic condition, and utilizing the orthogonality properties of the spherical harmonics, it follows that

$$im'A_{m'n'} + \frac{dc_{m'n'}}{dt} + \frac{1}{3}im'c_{m'n'} + \frac{1}{5}\Sigma imc_{mn} \int \int_{\text{sphere}} \cos \theta Y_n^m Y_{n'}^{m'*} d\sigma + F_{m'n'} = 0, \quad (3.56)$$

where the inhomogeneous term $F_{m'n'}$ is given by

$$F_{m'n'} = \int \int_{\text{sphere}} (u_0 \sin \theta \cos \phi + \psi_{b,\phi}) Y_{n'}^{m'*} d\sigma. \quad (3.57)$$

After some further manipulation, (3.56) becomes

$$\begin{aligned} im'A_{m'n'} + \frac{dc_{m'n'}}{dt} + \frac{1}{3}im'c_{m'n'} + \\ + \frac{1}{5}im'b\{c_{m',(n'+1)}\sqrt{\frac{(n'-m'+1)(n'+m'+1)}{(2n'+1)(2n'+3)}} + \\ + c_{m',(n'-1)}\sqrt{\frac{(n'-m')(n'+m')}{(2n'-1)(2n'+1)}}\} + F_{m'n'} = 0, \end{aligned} \quad (3.58)$$

again using the result from Arfken (p.456). Eliminating the $A_{m'n'}$ between (3.54) and (3.58) (and dropping the primes) gives a recursion relation for the c_{mn} coefficients:

$$\begin{aligned} \frac{dc_{mn}}{dt} + imc_{mn}\left(\frac{1}{3} - \frac{1}{2n+1}\right) + \\ + imb\left(\frac{1}{5} - \frac{1}{2n+1}\right) \underbrace{\left\{c_{m,(n+1)}\sqrt{\frac{(n-m+1)(n+m+1)}{(2n+1)(2n+3)}} + c_{m,(n-1)}\sqrt{\frac{(n-m)(n+m)}{(2n-1)(2n+1)}}\right\}}_{\text{coupling term}} \\ + F_{mn} = 0. \end{aligned} \quad (3.59)$$

Choosing the same uniformly sheared background flow used in the last section

$$\psi_b = -\alpha yz + \frac{1}{2}qby^2, \quad (3.60)$$

it follows that the inhomogeneous term F_{mn} is given once again by the integral (3.41):

$$F_{mn} = u_0 \sqrt{2\pi/3} (\delta_{m,-1} - \delta_{m,+1}) \delta_{n,1} + \frac{1}{3} \alpha \sqrt{6\pi/5} (\delta_{m,1} - \delta_{m,-1}) \delta_{n,2} \\ + \frac{1}{12} q_0 i \sqrt{96\pi/5} (\delta_{m,-2} - \delta_{m,+2}) \delta_{n,2} . \quad (3.61)$$

Equation (3.59) is a differentio-difference equation for the c_{mn} coefficients. It is interesting to note that allowing the core potential vorticity to be depth dependent has coupled the spherical harmonics in the wavenumber domain, which complicates the situation considerably⁸. This implies that the spherical harmonics are no longer the optimal set of basis functions. If the recursion relation is truncated at some $n = N$, then the problem can be simplified by writing (3.59) in matrix form:

$$\frac{dc_m}{dt} + iM_m c_m + F_m = 0 , \quad (3.62)$$

where c_m and F_m are column vectors, and M_m is an $N \times N$, real, tridiagonal matrix. The solution to (3.62) is then

$$c_m(t) = iM_m^{-1}F_m + a_1 V_1 e^{i\lambda_1 t} + a_2 V_2 e^{i\lambda_2 t} + \dots + a_N V_N e^{i\lambda_N t} , \quad (3.63)$$

where the a_n are arbitrary constants, the V_n are the eigenvectors of M_m , and the λ_n are its eigenvalues. To solve an initial value problem, the a_n must be chosen to satisfy the given initial conditions. Using a low order (4×4) truncation of the matrix equation (3.62) the λ_n were obtained analytically, and found to be real, implying that (3.62) has no exponentially growing modes. This result has been verified numerically for various values of b using 20×20 truncations of the matrix M_m . It is found that the first four eigenvalues are well described by the 4×4 truncation. The fact that the eigenvalues are all real is significant, since it shows that the basic state vortex is linearly stable. Given that b can become large enough that the circulation in the core can change sign, it is reasonable to expect that the solutions could become baroclinically unstable. Several authors have found solutions representing unstable baroclinic vortices. Using a 'heton'

⁸This presents the interesting possibility that η and ψ' may vary rapidly in θ even when the background flow field varies quite slowly.

model, Hogg and Stommel (1985) found that a baroclinic vortex becomes unstable if its radius is larger than 1.27 deformation radii. Pedlosky (1985) obtained a similar result using a two layer model of a baroclinic vortex. Flierl (1990) and Helfrich and Send (1988) found that columnar baroclinic vortices can be unstable if they are large enough and do not have too much barotropic circulation. It is likely that the stability of the basic state flow is due to the fact that the horizontal dimension is fixed at $R = ND/f_0$. Instabilities might become possible if the horizontal scale of the lens were allowed to be larger than this.

Instead of solving the matrix problem (3.62) directly, it is useful to try to deduce certain aspects of the solution behavior directly from (3.59). As mentioned earlier, primary attention will be given to the $m = 1$ harmonics, which are excited by the external vertical shear. Equation (3.59) has the interesting property that the equations for the $c_{m,1}$ and $c_{m,2}$ coefficients are decoupled from those for the rest of the c_{mn} . This makes it possible to compute both c_{12} and the speed u_0 in terms of the parameters of the problem, without solving (3.59) in its entirety. To do this, we will use (3.59) and (3.61) to obtain equations for c_{11} and c_{12} . Putting $m = n = 1$ gives

$$\frac{dc_{11}}{dt} - u_0\sqrt{2\pi/3} = ic_{12}\frac{2b}{15\sqrt{5}}, \quad (3.64)$$

and setting $m = 1, n = 2$ gives

$$\frac{dc_{12}}{dt} + \frac{2i}{15}c_{12} = -\frac{1}{3}\alpha\sqrt{6\pi/5}. \quad (3.65)$$

Notice that the external shear q_b does not appear in (3.64) or (3.65), implying that the $m = 1$ harmonics don't 'feel' the external horizontal shear⁹. Equation (3.65) may be easily solved to get

$$c_{12} = +\frac{5\alpha}{2}i\sqrt{6\pi/5}(1 - e^{-2it/15}) + c_{12}(0)e^{-2it/15}. \quad (3.66)$$

This is equal to the steady result found in (3.42) for a monopolar vortex, plus a periodic component of arbitrary amplitude. The periodic component constitutes the homogeneous

⁹It is easily seen from (3.61) that q_b appears only in the equations for the $m = 2$ spherical harmonics.

solution to (3.65), which obeys the dispersion relation (3.34) for free modes on a sphere. Next, notice that the value of c_{12} is independent of the parameter b . However, it turns out that the value of b has an important influence on the asymptotic behavior of the c_{mn} , and hence determines the convergence properties of the solution expansion (3.23). It will be seen shortly that the solution expansion does not converge if the vortex is too baroclinic ($|b| \geq 5/3$).

Translation

Substituting (3.66) into the equation for c_{11} gives

$$\frac{dc_{11}}{dt} = \{-\alpha b \sqrt{6\pi}/15 + u_0 \sqrt{2\pi/3}\} + e^{-2it/15} \left(\frac{2ib}{15\sqrt{5}} c_{12}^{(0)} + \alpha b \frac{\sqrt{6\pi}}{15} \right). \quad (3.67)$$

In order to avoid secular growth of c_{11} , the expression in curly braces must vanish, implying that the vortex moves with speed ¹⁰

$$u_0 = \frac{1}{5} \alpha b. \quad (3.68)$$

Therefore, the translation speed u_0 is directly proportional to the vertical shear α , and to the baroclinicity b . Notice that although there are $O(1)$ variations in potential vorticity within the core, the translation speed is very small ($u_0 = O(\alpha) \ll 1$). This is because the basic state potential vorticity varies only in z , and the smallness of the tilt induced by the external flow therefore causes the self propagation effect to appear at higher order. For a steady flow, recall that the shear α is linearly related to the amplitude of the $(1, 2)$ coefficient. Thus, the translation speed can be expressed as a function of b and the amplitude of this harmonic ¹¹:

$$u_0 = \frac{2}{25} \sqrt{\frac{5}{6\pi}} b |c_{12}|. \quad (3.69)$$

This shows that the translation speed is directly related to the *amplitude* of the boundary perturbation. It should be emphasized that, even if the motion of the boundary is a

¹⁰This choice of u_0 corresponds to choosing the appropriate frame of reference for the problem, which is of course the one which translates with the vortex.

¹¹If the flow is unsteady, then the time average of $|c_{12}|$ should be used in (3.69).

complicated function of time, the vortex moves at the *constant* rate given by (3.68). The propagation is due to the self propagation tendency of the dipole component of the potential vorticity field, while the shear balances the precession tendency of the barotropic component of the potential vorticity field.

There is a strong parallel between this translating vortex solution and the point vortex solutions presented earlier. In Chapter 2, solutions were obtained representing translating point vortex pairs when two point vortices with potential vorticities $1 + \Delta$ and $1 - \Delta$ were placed in a background flow with constant shear. The vortex pair was found to translate with speed

$$u_0 = \frac{\Delta}{2}(u_b(\vec{x}_1) - u_b(\vec{x}_2)) + \frac{1}{2}(u_b(\vec{x}_1) + u_b(\vec{x}_2)). \quad (3.70)$$

The second term on the right side of (3.70) is simply the average of the background flow advecting the two vortices. There is no analogous term in (3.68) because the average background flow speed over the core is exactly zero *by construction*. In the case in which the vortices are in a pure vertical shear, and the coordinate system is chosen such that the average background flow vanishes, (3.70) takes the particularly simple form

$$u_0 = Z\alpha\Delta, \quad (3.71)$$

where Z is the constant vertical separation between the vortices. The qualitative similarity between (3.68) and (3.71) is striking - in both cases the speed is proportional to the external vertical shear, and to a parameter measuring the baroclinicity of the pair. The major difference between the two is that in (3.71) the speed is a function of the vertical separation Z between the point vortices, while (3.70) contains no analogous term. This is due to the fact that the parameter S has been assigned a value of one, so that the half height D of the lens has the fixed value $D = f_0 R/N$.

In both the point vortex and the continuous vortex models background shear and potential vorticity variation within the core are essential to the propagation effect. The external shear serves to keep the eddy tilted (in a time average sense) in some

fixed direction, so that the baroclinic component of the potential vorticity field can self-propagate. Put somewhat differently, the external shear counterbalances the tendency of the barotropic component of the potential vorticity field to precess, which enables the baroclinic component of the potential vorticity field to self-propagate. Increasing the external shear causes a larger deformation of the eddy, allowing the baroclinic component of the potential vorticity field to interact with itself more strongly, which in turn leads to a greater propagation speed.

It is important to try to relate the translation speed u_0 to some integral property of the potential vorticity field. This will demonstrate that the propagation found here is not specific to the particular problem we have studied, but instead is a rather general phenomenon which can be expected in a large class of problems of this sort. It will be convenient to consider the potential vorticity equation in integral form:

$$\frac{d}{dt} \int_{\text{core}} q(z) x d\tau / \int_{\text{core}} q(z) d\tau = \int_{\text{core}} q(z) u d\tau / \int_{\text{core}} q(z) d\tau, \quad (3.72)$$

which may be obtained using the properties of material integrals (see, e.g., Batchelor, pp. 131–134). Now, $\int_{\text{core}} q(z) x d\tau / \int_{\text{core}} q(z) d\tau$ is just the x coordinate of the center of potential vorticity of the lens, which we shall denote by $\langle x \rangle$. Thus, (3.72) can be rewritten in the form

$$\frac{d \langle x \rangle}{dt} = \int_{\text{core}} q(z) u d\tau / \int_{\text{core}} q(z) d\tau \equiv \langle u \rangle, \quad (3.73)$$

This simply states that the center of potential vorticity of the lens moves at a rate given by the potential vorticity weighted average of the flow speed over the core. In the present case, this integral can be evaluated, and it will be shown in Appendix 2 that it is equal to $\frac{1}{5} \alpha b$ - exactly the speed found earlier by other means. In addition, it is shown by direct calculation that the speed u_0 of the vortex is equal to the *external* flow speed at the center of potential vorticity of the lens. In Chapter 4 (see pages 104–106) it will be demonstrated that both of these results are readily generalized to large amplitude, nonlinear solutions. This issue is also addressed in Appendix 2, using a somewhat different approach. In

these two sections it will be shown that in the absence of external flow, the center of potential vorticity *cannot* move, and that therefore the only component of the flow field that contributes to the integral in (3.73) is the background flow u_0 . From this result it follows fairly readily that the propagation speeds of the nonlinear solutions have the *same* dependence on α and b as was found for the linear solutions, and thus are precisely given by the relation (3.68).

It should be emphasized that the result $u_0 = \alpha b/5$ does not depend upon whether the solution is steady, or even upon whether steady solutions exist. It is similar to the result discussed in Chapter 2, where it was shown that the center of potential vorticity of a vortex pair translates steadily even when the motion of the vortices is unsteady. Notice that this is generally *not* the case for the center of *mass* (*i.e.*, the geometric center) of the vortex pair: if the motion of the individual vortices is unsteady, the velocity of their center of mass is also unsteady ¹². Only in the steady limit will the velocity of the center of mass coincide with that of the center of potential vorticity. This can be seen quite simply by considering the motion of two point vortices of different strengths in a quiescent fluid. In this case the vortex trajectories are concentric circles. From the results of Chapter 2 it is clear that the potential vorticity weighted average velocity $(Q_1 u_1 + Q_2 u_2, Q_1 v_1 + Q_2 v_2)/(Q_1 + Q_2)$ vanishes, while the average velocity $(u_1 + u_2, v_1 + v_2)/2$ is a periodic function of time. These considerations imply that picking u_0 to satisfy the solvability condition (3.68) is equivalent to choosing a coordinate system which translates with the center of potential vorticity of the lens:

$$u_0 = \frac{d \langle x \rangle}{dt} . \quad (3.74)$$

Steady Behavior

In principle it is a straightforward matter to integrate (3.59) directly using standard numerical techniques. This will not be done here, as many interesting results can be obtained from (3.59) by examining the possible steady solutions. The steady be-

¹²This is why a q -weighted average is used in the definition of u_0 .

havior of the vortex also has application to the unsteady behavior, since (3.63) shows that the unsteady solutions are made up of a steady part which is in equilibrium with the forcing, plus an unsteady component. A major result of this section is that there is a maximum baroclinicity b beyond which no solutions exist unless the external shear vanishes identically.

Setting $\frac{dc_{mn}}{dt} = 0$ gives a three term recursion relation:

$$\begin{aligned} & imc_{mn}\left(\frac{1}{3} - \frac{1}{2n+1}\right) + \\ & + imb\left(\frac{1}{5} - \frac{1}{2n+1}\right)\left\{c_{m,n+1}\sqrt{\frac{(n-m+1)(n+m+1)}{(2n+1)(2n+3)}} + c_{m,n-1}\sqrt{\frac{(n-m)(n+m)}{(2n-1)(2n+1)}}\right\} \\ & + F_{mn} = 0. \end{aligned} \quad (3.75)$$

Notice that any $m = 0$ (z axisymmetric) mode satisfies (3.75) exactly. This demonstrates that the solutions are nonunique, as adding any axisymmetric mode to a given solution produces another solution different from the first. In what follows, attention will be focused on those modes which are directly forced by the external vertical shear - the $m = \pm 1$ modes in this case, which filters the $m = 0$ modes out. Evaluating (3.75) for $m = n = 1$ and $m = 1, n = 2$ gives

$$\begin{aligned} c_{12} &= +\frac{5}{2}i\alpha\sqrt{6\pi/5} \\ c_{12} &= +\frac{15}{2}\frac{iu_0}{b}\sqrt{10\pi/3}, \end{aligned} \quad (3.76)$$

from which it follows that the translation speed is again given by (3.68). In principle, it seems as if all of the coefficients could be generated by simply substituting different values of m and n into (3.75). It turns out that this is not the case, since only one term in the sequence (c_{12} , for the $m = 1$ sequence) can be specified.

To compute the remainder of the c_{mn} we therefore write (3.75) as a matrix equation, which, when truncated, can be solved for the c_{mn} . Fortunately, when b is not too large the coupling terms in (3.75) are small, so that the c_{mn} decay rapidly, and satisfactory results can be obtained using a low order truncation. In matrix form, (3.75) takes

the form

$$iM_m c_m + F_m = 0, \quad (3.77)$$

which is the steady form of (3.62). The coefficient vector c_m is obtained by inverting the matrix M_m , which gives

$$c_m = iM_m^{-1} F_m. \quad (3.78)$$

Figure 3.7a shows the steady boundary shape obtained for the case in which $b = 1$, $\alpha = 0.1$, and $q_b = 0$. The plot shows a vertical cross section through the vortex taken along the $+y$ axis. Figure 3.7b shows the steady boundary shape when $\alpha = 0.1$, $q_b = 0$, and $b = 4$. Notice the discontinuity in η , indicating that the solution expansion is locally nonconvergent.

To find the cause of this nonconvergence, consider the large n limit of the recursion relation (3.75). It is easy to show that in this case (3.75) is approximated by

$$c_{m,n+1} + \Omega c_{mn} + c_{m,n-1} \sim 0, \quad (3.79)$$

where

$$\Omega \equiv \frac{10}{3b}.$$

This is a second order homogeneous difference equation with constant coefficients, which may be solved by looking for solutions of the form $c_{mn} \sim \gamma^n$, where γ is a complex number to be determined. Substituting into (3.79), it follows that there are solutions of the assumed form provided that γ satisfies

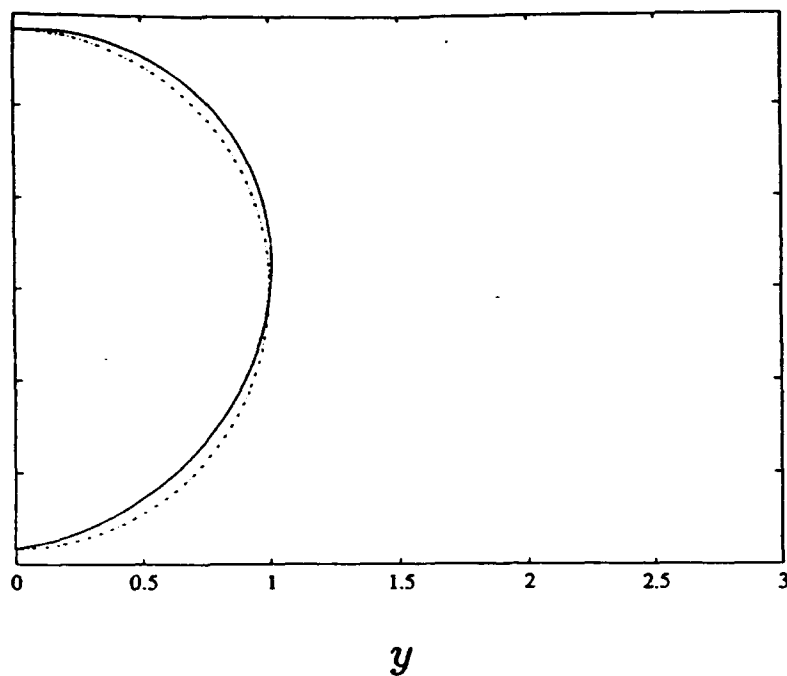
$$\gamma^2 + \Omega \gamma + 1 = 0, \quad (3.80)$$

so that

$$\gamma = \frac{1}{2}(-\Omega \pm \sqrt{\Omega^2 - 4}). \quad (3.81)$$

When $|\Omega| > 2$ there are two real roots, one of which is greater than one, and another which is less than one, as shown in Figure 3.8. Thus, there is one sequence in which the c_{mn} grow with n , and another in which they decay with n . The increasing sequence gives

a

 z 

b

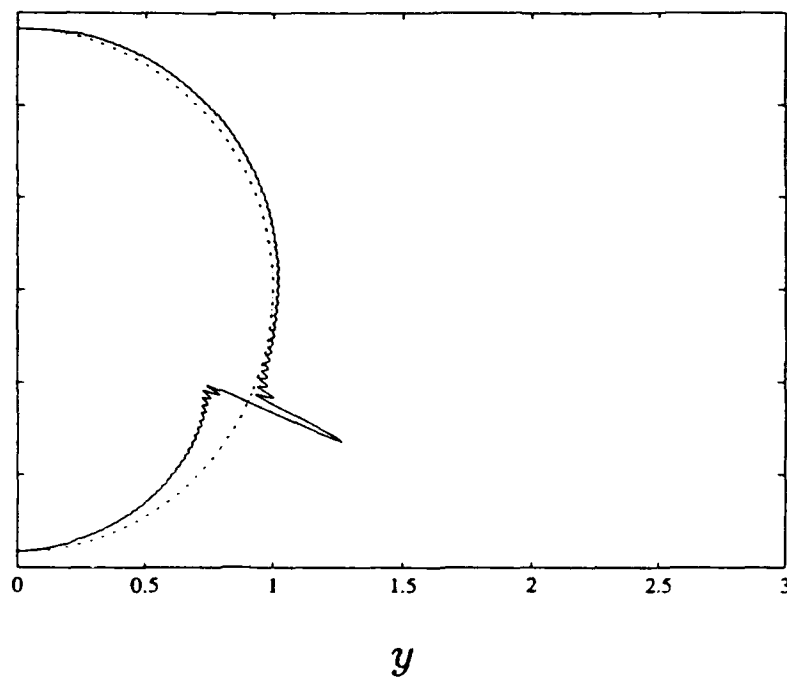
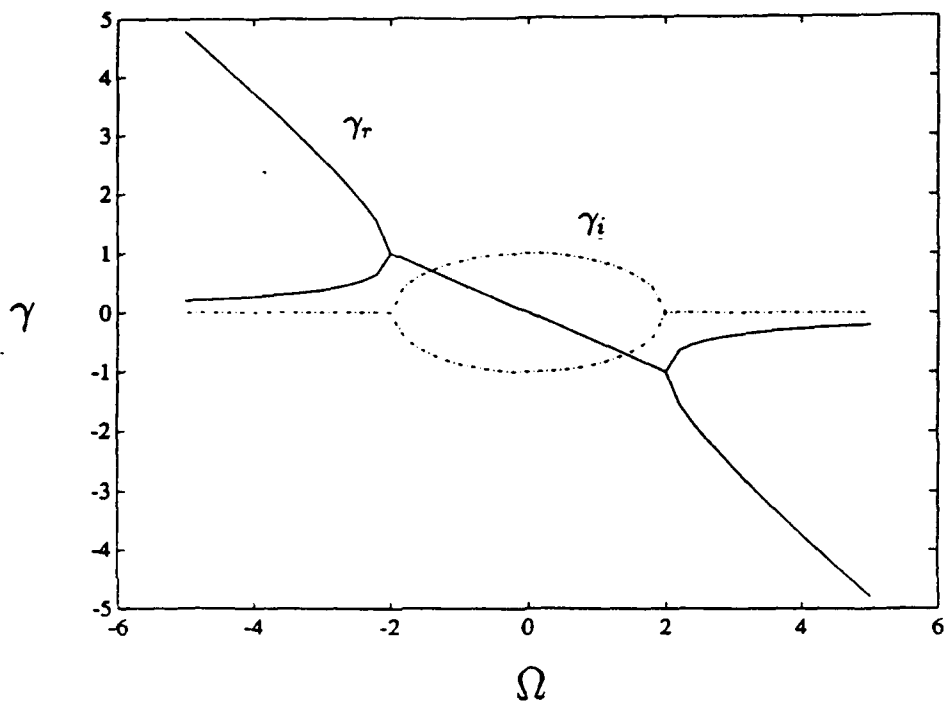
 z 

Figure 3.7: Plot of the steady boundary shape when $\alpha = 0.10$, $b = 1.0$ (7a), and when $\alpha = 0.10$, $b = 4.0$ (7b). In the first case the series converges rapidly, and only a few terms in the expansion (3.23b) are needed. Ten terms have been kept here. In the second case the series converges slowly, and 200 terms have been kept. Notice the singularity in η when b is large, indicating that the solution expansion is invalid. The solution breaks down when the basic flow within the core vanishes at some depth, which happens when $|b| \geq 5/3$.

a



b

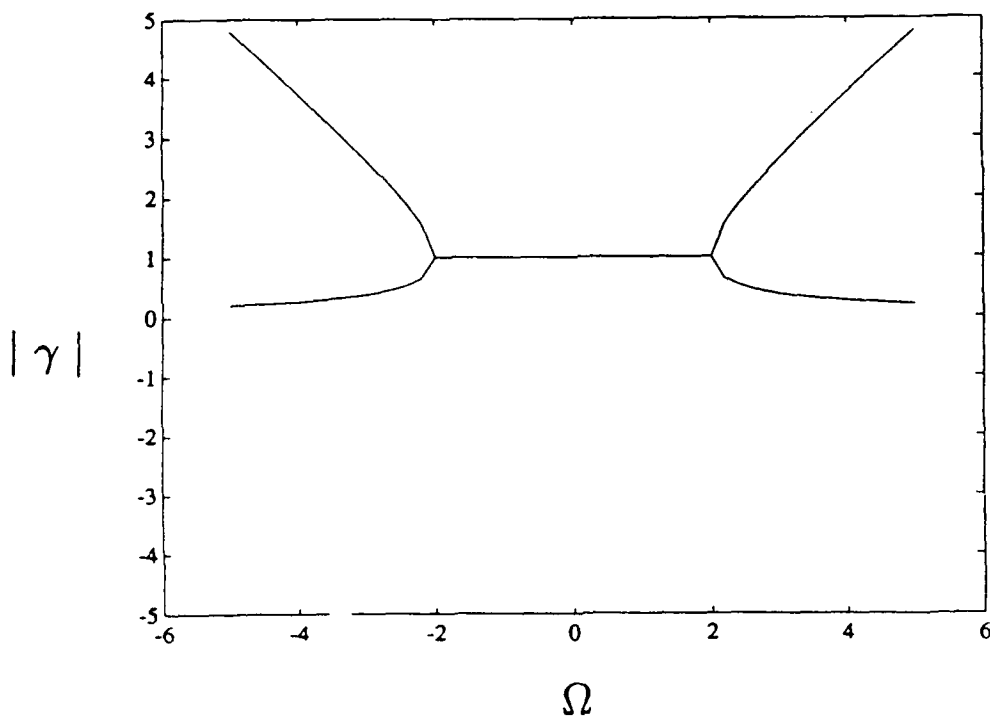


Figure 3.8: Plot of γ as a function of $\Omega \equiv \frac{10}{3b}$. Notice that Ω is small for baroclinic vortices and $\Omega \rightarrow \pm\infty$ in the monopolar limit. (8a) shows the real and imaginary parts separately, while (8b) shows the magnitude of γ . The asymptotic behavior of the c_{mn} as $n \rightarrow \infty$ is given by $c_{mn} \sim \gamma^n$, so that solutions for which $\gamma > 1$ are divergent solutions. The solution also breaks down when $|\gamma| = 1$, which occurs when $-2 \leq \Omega \leq 2$ (as discussed in the text).

solutions which are unbounded, and it is therefore eliminated in favor of the sequence which decays as $n \rightarrow \infty$.

When $|\Omega| \leq 2$, γ is complex and has magnitude one, implying that as $n \rightarrow \infty$ the magnitude of the c_{mn} approaches some constant value. In this case the ratio test is insufficient to determine the convergence properties of the solution expansion. We take the approach of plotting the solutions to see the form they take. Using (3.8) it can be shown that $|\Omega| \leq 2$ implies that the vortex is sufficiently baroclinic that $u^v(\theta)$ vanishes at some depth inside the core. It turns out that the expansion converges everywhere *except* where the basic state flow $u^v(\theta)$ vanishes. This nonconvergence is manifested by a discontinuity in η , as shown in Figure 3.7b. Thus, when $|\Omega| \leq 2$ (or, equivalently, $|b| \geq 5/3$), the only convergent solution is the trivial one in which the vortex is spherical and the external shear vanishes identically.

The singular behavior of the boundary is similar to that noted by Flierl (1988) in a study of columnar geostrophic vortices, where it was found that steady boundary deformations became infinite if there was counter-rotating flow in the vortex core. In the present case, it is apparent that when the basic flow $u^v(\theta)$ vanishes at some depth within the core, no steady solutions (in nonvanishing shear) exist which are consistent with the model assumptions. This behavior is evidently due to the presence of a steering level at the depth where the basic flow changes sign. Recall that a steering level is a level at which the phase speed c_r of a stable wave is equal to the mean flow speed $U(z)$ (see, e.g., Pedlosky, 1987). To apply these ideas in the present case, consider the motion of a particle on the vortex boundary. For simplicity, assume that the boundary is almost spherical ($r \approx 1$), as in Chapter 3. Now, if there is a wave on the vortex boundary, then the motion of the particle is approximately given by the linearized evolution equations

$$\begin{aligned} \frac{d\phi}{dt} &\approx u_{(\phi)}^v(\theta) \\ \frac{d\eta}{dt} &= u_{(r)}(\theta, \phi(t)) . \end{aligned} \tag{3.82}$$

where θ and ϕ represent the polar and azimuthal coordinates of the particle in a spherical coordinate system. $u_{(\phi)}^v(\theta)$ represents the basic state azimuthal flow

$$u_{(\phi)}^v(\theta) = \left(\frac{1}{3} + \frac{1}{5}b \cos \theta\right) \sin \theta, \quad (3.83)$$

and $u_{(r)}(\theta, \phi)$ represents the horizontal flow across $r = 1$ associated with the boundary wave. The equations (3.82a,b) show that the ϕ coordinate of the water particle changes as a result of advection by the basic state azimuthal flow, while the η coordinate of the parcel changes in response to the weak flow normal to the boundary of the lens (Since the flow is horizontal to lowest order, the θ coordinate of each parcel remains fixed.). Solving (3.82a) shows that ϕ is a linear function of t , and therefore (3.82b) becomes

$$\frac{d\eta}{dt} = u_{(r)}(\theta, \phi_0 + u_{(\phi)}^v(\theta)t). \quad (3.84)$$

In any stable, steadily translating configuration, $u_{(r)}$ must be a periodic function of time, and it follows from (3.84) that η will be also. To show this, recall from Chapter 3 that the velocity normal to the boundary can be written as a sum of spherical harmonics. For steady solutions, this summation can be written

$$u_{(r)} = \sum_n \sum_m K_{mn} P_n^m(\theta) e^{im\phi}, \quad (3.85)$$

where it is assumed that the K_{mn} are known. Now, in a stationary frame of reference (3.84) can be rewritten

$$\frac{\partial \eta}{\partial t} + \frac{u_{(\phi)}^v(\theta)}{\sin \theta} \frac{\partial \eta}{\partial \phi} = u_{(r)}(\theta, \phi_0 + u_{(\phi)}^v(\theta)t), \quad (3.86)$$

and it follows that when the rotation frequency is nonzero everywhere within the core, steady solutions to (3.84) can be found of the form

$$\frac{\partial \eta}{\partial \phi} = \frac{\sin \theta}{u_{(\phi)}^v(\theta)} \sum_n \sum_m K_{mn} P_n^m(\theta) e^{im\phi} \quad (u_{(\phi)}^v(\theta) \neq 0 \quad \forall \theta). \quad (3.87)$$

This expression can be integrated term by term to show that η is periodic in ϕ (and hence also in t , since $\phi(t)$ is a linear function of t). At the steering level, however, such a

steady balance is impossible, since $u_{(\phi)}^v(\theta)$ vanishes. In this case η evolves according to

$$\frac{\partial \eta}{\partial t} = \Sigma_n \Sigma_m K_{mn} P_n^m(\theta) e^{im\phi_0}, \quad (3.88)$$

where ϕ_0 is a constant. The right hand side of (3.88) is a function of θ alone, so that η grows linearly with time in the vicinity of the steering level. It follows that no small amplitude steady solutions are possible in the presence of a steering level.

Summary

A simple model of a lens-shaped quasigeostrophic vortex in external shear has been investigated. Approximate analytical solutions were obtained for the weak shear limit. Steadily precessing solutions were found representing a monopolar vortex in a quiescent fluid. Steady and unsteady solutions were found representing a vortex in the presence of external shear. Finally, translating solutions were found representing a baroclinic vortex in a shear flow. Both external shear and baroclinicity are essential to the translation effect. It is demonstrated that the translation may be simply understood as a self propagation effect, which is due to the self interaction of the *baroclinic* component of the potential vorticity field. The propagation speed represents the speed of the center of potential vorticity of the lens, which was shown to be equal to the external flow speed at the center of potential vorticity of the lens. The behavior of the solutions can often be qualitatively described by a model consisting of a pair of point potential vortices in an external flow. No solutions were found for which the basic state flow within the vortex core changed sign with depth, unless the external shear vanished identically. In the next chapter a series of numerical integrations will be discussed, which extend the present results to include aspects of the behavior of nonlinear solutions. The results of this chapter will help in understanding the numerical results in the next chapter. It is felt that the model discussed here provides a qualitatively correct description of certain aspects of the behavior of a Mediterranean Salt Lens in an oceanic shear flow. In Chapter 5 this idea will be examined in some detail, when the Meddy float data are examined and compared with the model predictions.

Chapter 4

Numerical Calculations

Introduction

In this chapter, the steady configurations which are possible for an anticyclonic vortex of fixed volume in an external flow with uniform shear will be examined. In Chapter 3 this problem was considered for the case in which the external shear was very small, so that analytical techniques could be used to solve the problem. These linear solutions will now be extended into the nonlinear regime, and the stability of the solutions examined numerically. The analysis will allow a determination of the area of the (α, b) ¹ plane in which steady solutions can be found. In addition, the behavior of highly baroclinic vortices characterized by $|b| \geq 5/3$ can be examined using this numerical approach. As in the last section of Chapter 3, the investigation will concentrate on the influence of external vertical shear and variable core baroclinicity. It is found that when the shear is not too large the steady solutions are stable, as perturbing them leads only to a periodic modulation of the original steady solution. Thus, in this regime the behavior of the solutions is accurately given by the linearized solutions in Chapter 3. If the external shear is large, parts of the core can be torn off by the external flow. The idea that fluid can be torn from the core is consistent with the observations of Armi *et al.* (1988), who reported numerous blobs of anomalously salty water outside the core of Meddy Sharon.

Only steadily translating solutions will be examined, since an exhaustive treatment of all possible behaviors is beyond the scope of this work. However, it was shown in Chapter 3 that any unsteady solution is made up of a steady component in equilibrium with the external forcing (*i.e.*, the steady background shear) plus a time dependent component. Therefore, the solutions represent the time-mean behavior of a family of unsteady solutions. The analysis is therefore more general than it might appear, since the

¹Recall that the strength of the external vertical shear is given by α , while b measures the baroclinicity of the flow in the core.

steady solutions can presumably be obtained from the unsteady ones through a suitable averaging procedure. For example, the analysis in the next Chapter shows how average 'tilt' of the core of a Meddy can be inferred by averaging the trajectories of floats at different depths within the core.

The method by which the steady solutions are found is a modified contour dynamics technique like that used by Polvani (1988) and Meacham (*personal communication*). The contour dynamics technique is fairly standard now, and has been used for studies of 2D flow by a number of authors (*e.g.*, Zabusky *et al.*, 1979). It is a Lagrangian numerical scheme, which follows particles on vorticity fronts as they are advected by the flow. Pratt and Stern (1985) have applied the technique to $1\frac{1}{2}$ layer quasigeostrophic flow. The application of the technique to stratified quasigeostrophic flow was first suggested by Kozlov (1985), and the idea has since been used by Meacham (*personal communication*). Briefly, the idea is that if the quasigeostrophic potential vorticity field in a stratified fluid is horizontally piecewise constant, then the velocity at any point in the fluid can be expressed as a surface integral over the potential vorticity interfaces in the problem. Thus, the position of the interfaces uniquely characterizes the entire flow field. A numerical algorithm was developed which calculates the velocity at each point on the vortex boundary by discretizing the boundary and performing a numerical surface integration at each time-step. In a forward integration, the velocity data are used to advect the boundary; when searching for steady solutions, the velocity data are used to iterate towards a steady configuration in a way that will be described shortly.

Derivation of the Contour Dynamics Equations

The numerical algorithm used is designed to solve a field equation of the form

$$\nabla^2 \psi = q \quad (4.1)$$

$$\psi \rightarrow \psi_b, \text{ as } r \rightarrow \infty$$

to obtain the instantaneous flow field. The particles on the boundary are then advected by the flow according to the kinematic relations

$$\begin{aligned}\frac{dx}{dt} &= -\frac{\partial\psi}{\partial y}, \\ \frac{dy}{dt} &= +\frac{\partial\psi}{\partial x}.\end{aligned}\tag{4.2}$$

For simplicity the streamfunction is divided into two components:

$$\psi = \psi_v + \psi_b,\tag{4.3}$$

where ψ_v and ψ_b satisfy

$$\begin{aligned}\nabla^2\psi_v &= \begin{pmatrix} q_v(z) & \text{inside} \\ 0 & \text{outside} \end{pmatrix} \\ \psi_v &\rightarrow 0 \text{ as } r \rightarrow \infty \\ \nabla^2\psi_b &= q_b = \text{a constant}.\end{aligned}\tag{4.4}$$

To facilitate comparisons with the Meddy data, the eddy potential q_v is in this case taken in the form ²

$$q_v(z) = -1 - bz.\tag{4.5}$$

Because q_b is a constant, the equation for ψ_b can be solved easily, while that for ψ_v can be solved using a Green's function integral. To do this, we shall make use of the free space Green's function for the Poisson equation

$$G(x, y, z | x_0, y_0, z_0) = -\frac{1}{4\pi}((x - x_0)^2 + (y - y_0)^2 + (z - z_0)^2)^{-1/2},\tag{4.6}$$

which satisfies

$$\nabla^2 G = \delta(x - x_0, y - y_0, z - z_0)\tag{4.7}$$

$$G \rightarrow 0, \text{ as } r \rightarrow \infty.$$

²The factor of -1 in (4.5) will give solutions which are anticyclonic, and which therefore tilt in a direction opposite to that of the solutions in Chapter 3, but will not otherwise qualitatively affect their behavior.

Using (4.1) and (4.7), it is easy to obtain an integral expression for ψ using the 'multiply and subtract' technique. This is done by multiplying (4.7) by ψ_b , (4.4) by G , and subtracting the resulting equations. If the result is then integrated over all space and the background streamfunction ψ_b added, an integral expression for ψ is obtained. The solution to (4.1) can therefore be written

$$\psi(x, y, z) = \psi_b + \int \int \int q_v(z_0) G(x, y, z | x_0, y_0, z_0) d\tau_0 + \int \int (G \vec{\nabla} \psi - \psi \vec{\nabla} G) d\sigma_0, \quad (4.8)$$

where the integration is over all space, because the fluid is assumed to be unbounded³. The surface integral in (4.8) vanishes if the fluid is unbounded (since the integrand goes like r^{-3} while the bounding area increases as r^2), so that the integral vanishes like $1/r$ as $r \rightarrow \infty$. Thus, ψ is given by

$$\psi(x, y, z) = \psi_b + \int \int \int q_v(z_0) G(x, y, z | x_0, y_0, z_0) d\tau_0, \quad (4.9)$$

where the integration is carried out over the region in which $q_v(z_0)$ is nonzero (i.e., the core). Taking the gradient of (4.8) gives

$$\vec{\nabla}_{xyz} \psi = \vec{\nabla}_{xyz} \psi_b + \int \int \int q_v(z_0) \vec{\nabla}_{xyz} G d\tau_0. \quad (4.10)$$

Because $\vec{\nabla} G$ is antisymmetric with respect to an interchange of x, y, z and x_0, y_0, z_0 , we may write $\vec{\nabla}_{xyz} G = -\vec{\nabla}_{x_0 y_0 z_0} G$. It follows that

$$\vec{\nabla}_{xyz} \psi = \vec{\nabla}_{xyz} \psi_b - \int \int \int q_v(z_0) \vec{\nabla}_{x_0 y_0 z_0} G d\tau_0, \quad (4.11)$$

or, equivalently,

$$\vec{\nabla}_{xyz} \psi = \vec{\nabla}_{xyz} \psi_b - \int \int \int \{ \vec{\nabla}_{x_0 y_0 z_0} (q_v G) - G \vec{\nabla}_{x_0 y_0 z_0} q_v \} d\tau_0. \quad (4.12)$$

Using the gradient theorem (see, e.g., Hildebrand, 1980) the first volume integral can be rewritten as a surface integral, giving

$$\vec{\nabla}_{xyz} \psi = \vec{\nabla}_{xyz} \psi_b - \int \int q_v G d\sigma_0 + \int \int \int G \vec{\nabla}_{x_0 y_0 z_0} q_v d\tau_0, \quad (4.13)$$

³ It is a simple matter to include a single horizontal or vertical boundary by including an image vortex in the definition of the Green's function.

where the surface integration is performed over the closed surface bounding the vortex.

Taking x and y components gives

$$\begin{aligned}\frac{\partial \psi}{\partial x} &= - \int \int q_v(z_0) G(x, y, z | x_0, y_0, z_0) dy_0 dz_0 + \frac{\partial \psi_b}{\partial x} \\ \frac{\partial \psi}{\partial y} &= + \int \int q_v(z_0) G(x, y, z | x_0, y_0, z_0) dx_0 dz_0 + \frac{\partial \psi_b}{\partial y},\end{aligned}\quad (4.14)$$

where the volume integral does not appear because q_v depends only on z . Using (4.2) these may be written

$$\begin{aligned}\dot{y}(x, y, z, t) &= - \int \int q_v(z_0) G(x, y, z | x_0, y_0, z_0) dy_0 dz_0 \\ \dot{x}(x, y, z, t) &= - \int \int q_v(z_0) G(x, y, z | x_0, y_0, z_0) dx_0 dz_0 + u_b(z),\end{aligned}\quad (4.15)$$

where it is assumed that the external flow is zonal, and depends only on z , as in the last section of Chapter 3. The equations (4.15) are those on which the contour dynamics algorithm is based. Notice that the velocity at *any* point in space is expressed as a surface integral over the vortex boundary. However, the numerical algorithm solves (4.15) for only those points (x, y, z) on the vortex boundary. Details of the numerical implementation can be found in Appendix 3.

An Algorithm for Finding Steady Solutions

The process of finding steady solutions is conceptually quite simple. The problem may be succinctly stated as follows: given a lens with fixed volume, what are the allowable steady configurations as a function of the external vertical shear? To solve this problem numerically, the boundary of the lens is approximated by a number of horizontal contours, which represent the intersections of a family of horizontal planes with the boundary. The steady configurations are of course the configurations for which the streamfunction is constant on each horizontal contour ⁴. To find these configurations, an iterative algorithm based on the standard Newton-Raphson root finding technique is used. Starting with an imperfect initial guess at the boundary shape (see Figure 4.1), the algorithm uses the calculated value of the streamfunction and its horizontal gradient

⁴in a reference frame translating with speed u_0

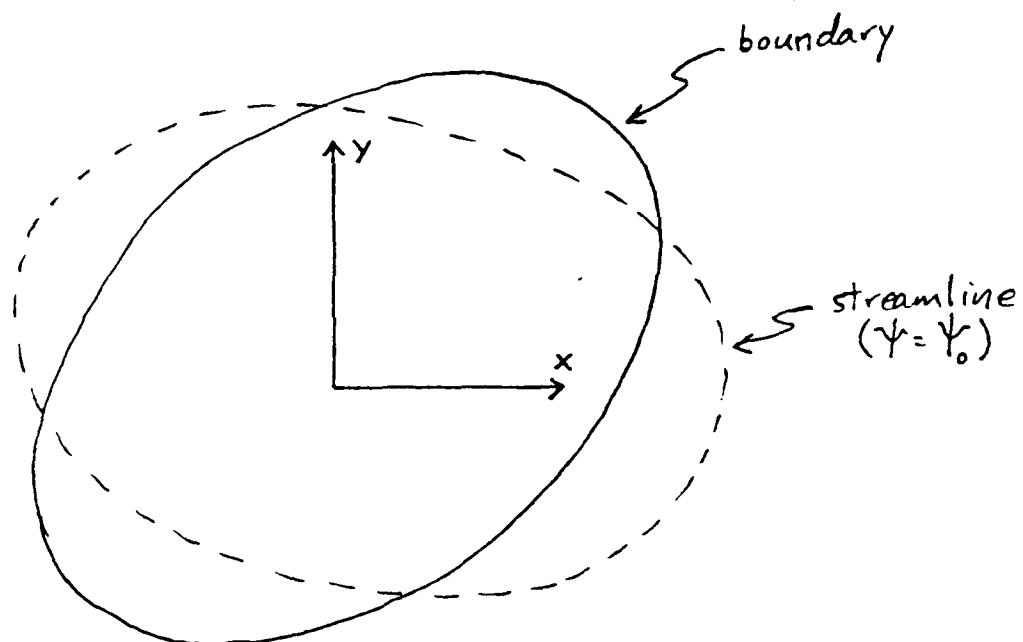


Figure 4.1: Schematic of algorithm for finding steady states. Beginning with an imperfect guess at the steady boundary shape, the value of the streamfunction on the boundary and its normal gradient are used to iterate towards a steady solution.

on a contour to adjust the boundary shape. To find a steady configuration characterized by $\psi = \psi_0$ on the boundary at some depth, the boundary points are moved according to

$$\begin{aligned} x_{\text{new}} &= x_{\text{old}} - \hat{x} \cdot \hat{n}(\psi - \psi_0) / \frac{\partial \psi}{\partial n} \\ y_{\text{new}} &= y_{\text{old}} - \hat{y} \cdot \hat{n}(\psi - \psi_0) / \frac{\partial \psi}{\partial n} . \end{aligned} \quad (4.16)$$

where ψ_0 is in general different at each depth, and is chosen such that the area within each contour is preserved through the iteration process. The normal gradient of the streamfunction is just the velocity along a streamline, which is computed using the contour dynamics algorithm discussed earlier. The value of the streamfunction on the boundary is obtained (to within an arbitrary function of z) by integrating the velocity along a horizontal contour

$$\psi(s) = \int^s (v dx - u dy) , \quad (4.17)$$

where s measures the arc length along the contour. After each iteration, the velocity field associated with the new boundary shape is computed, and the whole process repeated until a desired degree of accuracy is obtained, that is, until the summed root-mean-square deviation of the streamfunction from its expected value is sufficiently small. In most of the solutions to be shown, adequate convergence was obtained after only 15 or 20 iterations. Due to the nature of these numerical solutions, they are not exact, and some small time variations are inevitable. Each of the steady solutions can therefore be thought of as the true steady solution plus some small time dependent anomaly.

There are several potential problems with the procedure used, largely resulting from the fact that the solution space is very large. Therefore, the solution space has been constrained in a way which will be described momentarily. The problem is analogous to that of searching for roots in a multidimensional space – the root found depends upon the initial guess that is made. In its most general form the problem is underconstrained, as there are infinitely many possible steady configurations for a vortex of fixed volume in a specified external shear. To see why this is so, recall that in Chapter 3 it was found that, for a given α and b , the possible steady solutions were given by a forced

component plus an arbitrary distribution $m = 0$ (z -axisymmetric) free modes. Each of these $m = 0$ modes was found to be an exact steady solution. The form of the steady solutions can therefore be altered by varying the distribution $m = 0$ modes. Because of this nonuniqueness, it was necessary to constrain the solutions so that the area within each horizontal contour was preserved through the iteration process, which effectively fixes the distribution of free modes in the solution. This is justified if the steady solutions are regarded as representing the time-mean behavior of unsteady solutions, as discussed earlier. The constraint is stronger than merely requiring that the volume of the vortex be preserved, and it places very strong limitations on the ways in which the profile of the vortex can change. In particular, it ensures that the free modes are carried through the iteration process essentially unaltered, so that initial conditions with two lobed vertical structure result in two lobed steady states, and spherical initial conditions give solutions with one lobe, as shown in Figure 4.2. From the above discussion, it is apparent that by an appropriate choice of the initial boundary shape, one could readily generate solutions which were vertically stretched, vertically squashed, pear shaped, etc. Because in the absence of external flow *any* axisymmetric potential vorticity distribution is an exact steady solution to the potential vorticity equation (3.1), there will be a unique family of steady solutions branching out from each of the many possible initial shapes. Each of these families is characterized by the θ dependence of the initial boundary shape. In this work, attention will be focused on the spherical family (*i.e.*, the solutions obtained from a vortex which is initially spherical), as these are more representative of Meddy-like vortices than are solutions with multi-lobed vertical structure.

Steady Solutions

Some simple numerical solutions are shown in Figure 4.3. As in linear theory, all steady solutions are tilted transversely. In the present case, however, the boundary deformations may be quite large. The figure shows a sequence of steady configurations for a monopolar vortex ($b = 0$) as the vertical shear parameter α is varied from 0

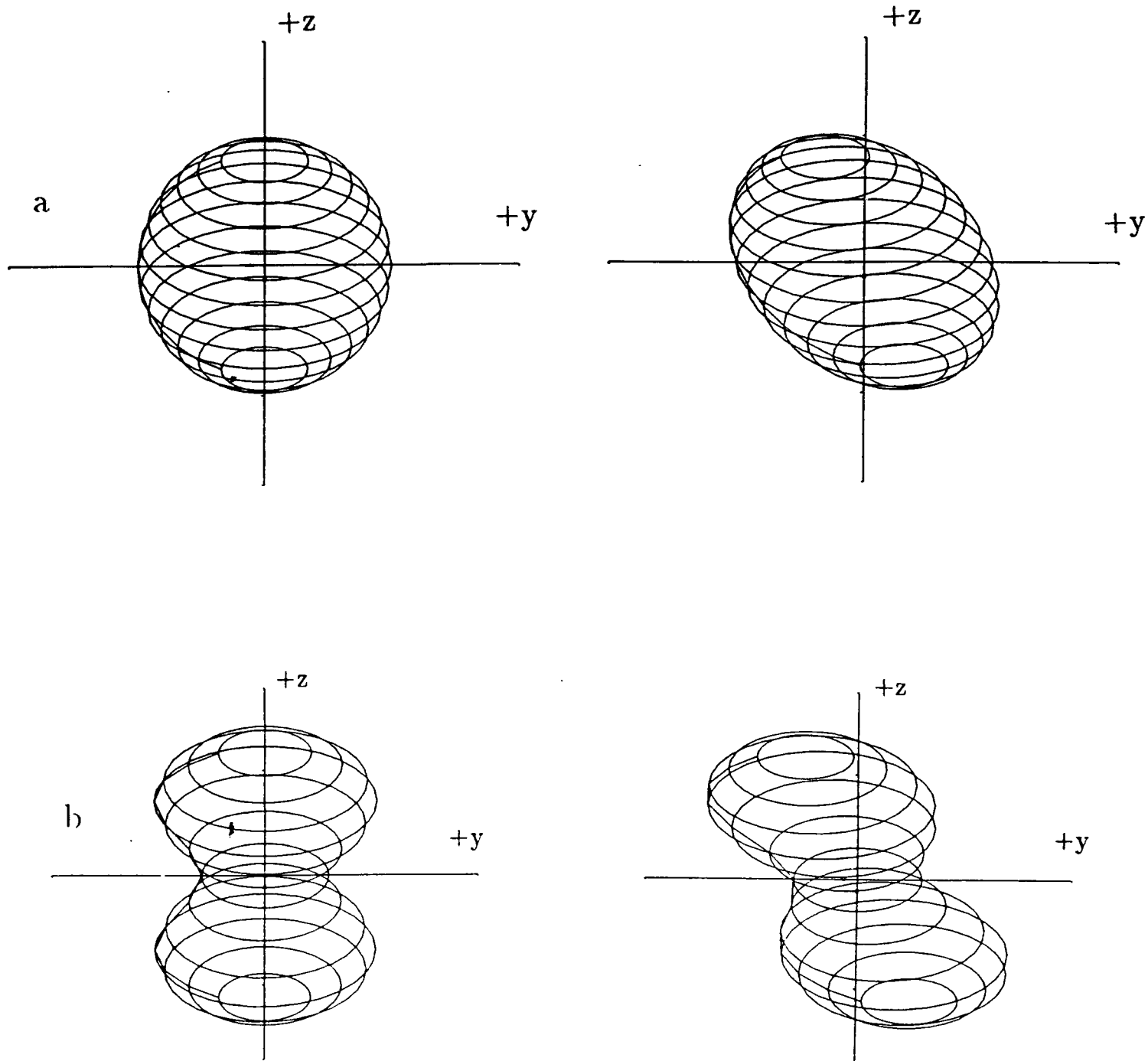


Figure 4.2: Plot showing how the initial guess influences the final steady solution which is found, due to the requirement that the area within each contour be preserved through the iteration process. In 4.2a, a spherical initial guess results in a spheroidal steady solution, while in 4.2b a two lobed initial guess gives a two lobed steady solution.

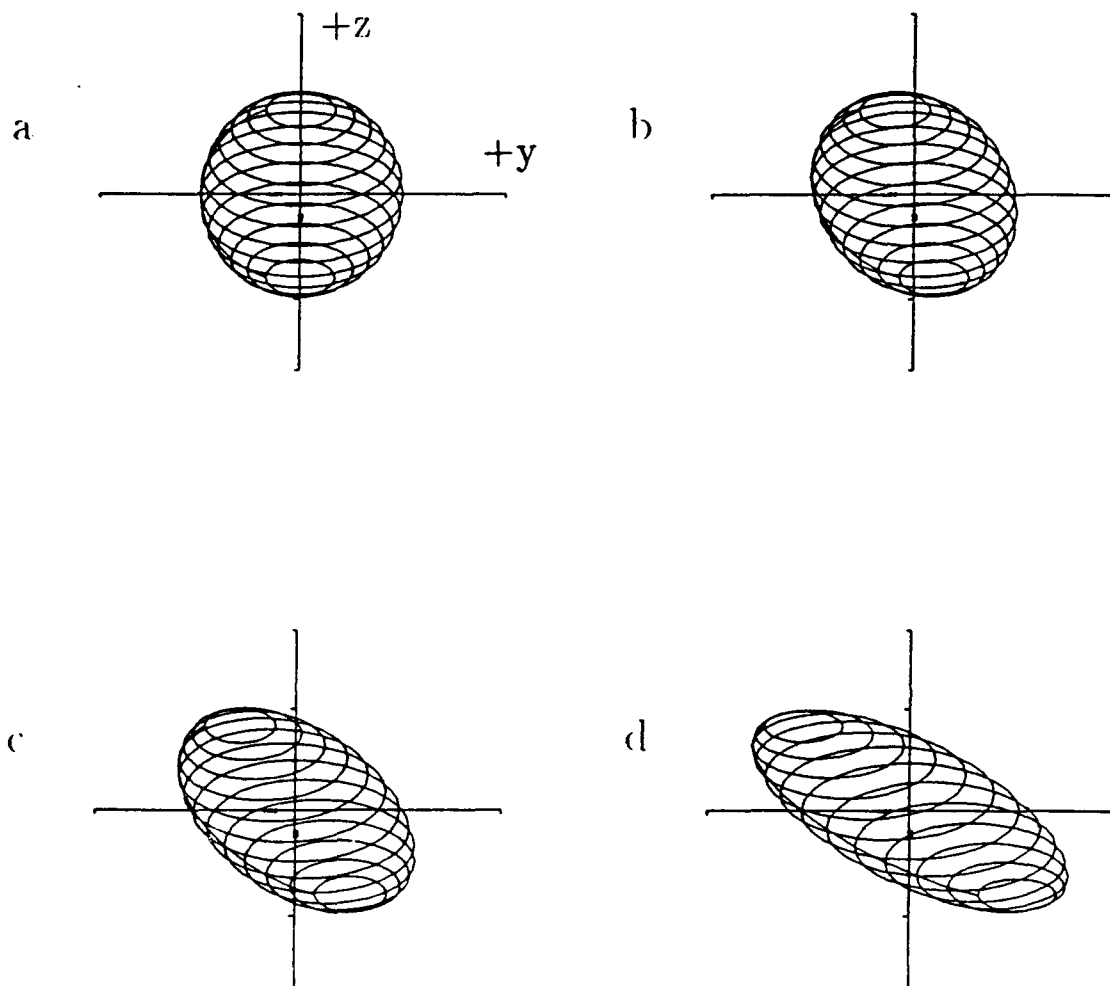


Figure 4.3: A sequence of steady solutions for an anticyclonic monopolar vortex ($b = 0$) in external vertical shear given by $u_s = \alpha z$. The shear, and hence the size of the boundary deformation increase from 4.3a to 4.3d. In 4.2a the shear parameter α is 0.0, in 4.2b it is 0.04, in 4.2c it is 0.08, and in 4.2d it has a value of 0.12. Notice that the steady configurations are planar antisymmetric with respect to both the (x, y) and the (x, z) planes.

through 0.12⁵. In the solutions shown the boundary of the vortex is approximated by 13 horizontal contours, each containing 30 points. The solutions look qualitatively like tilted ellipsoids. The form of the boundary deformations agrees well with that predicted by linear theory (see equation (3.44)). These results are not new, as similar solutions have been obtained analytically by Zhmur *et al.* (1989) for a vortex with uniform core potential vorticity. They are shown primarily to relate the numerical results to the linear solutions which were discussed in the last chapter. Notice that all solutions are transversely tilted, as predicted by linear theory. For small external shears, the boundary deformations are small, and the shapes of the numerical solutions agree quite well with the analytical solutions discussed in Chapter 3. In this simple case (in which the vortex is purely monopolar), the steady solutions can be shown to be ellipsoids, and exact analytic solutions have been found by Meacham *et al.* (*manuscript in preparation*).

Next consider the situation in which the core potential vorticity is a function of depth ($b \neq 0$). In this case the rotation frequency varies along the rotation axis of the lens, and the solutions are more strongly deformed near the bottom, where rotation rates are quite small. This is consistent with equation (3.83), which shows that linear theory predicts that the size of the linear perturbations varies inversely as the speed of the basic flow. Figure 4.4 shows a series of solutions in which b is fixed ($b = 1$) and α is varied. In (a) there is no vertical shear ($\alpha = 0$), in (b) $\alpha = 0.02$, in (c) $\alpha = 0.04$, in (d) $\alpha = 0.06$, in (e) $\alpha = 0.07$, and in (f) $\alpha = 0.08$. Notice the up/down asymmetry of the solutions, which increases as the external shear grows. There is a critical shear ($\alpha \approx 0.07$) beyond which the solutions do not converge, due to the formation of cusps on the boundary (as discussed by Polvani (1988) in a study of 2D vortices). The azimuthal flow associated with the solutions 4.4a, 4.4c, and 4.4d is shown in Figure 4.5. Notice that as the external shear increases, the axis of rotation becomes increasingly tilted, and velocities on the bottom contour get progressively smaller. Any further increase in α

⁵ $\alpha = 0.12$ corresponds to a jump in the external flow over the depth of the lens which is 36% of the maximum swirl speed.

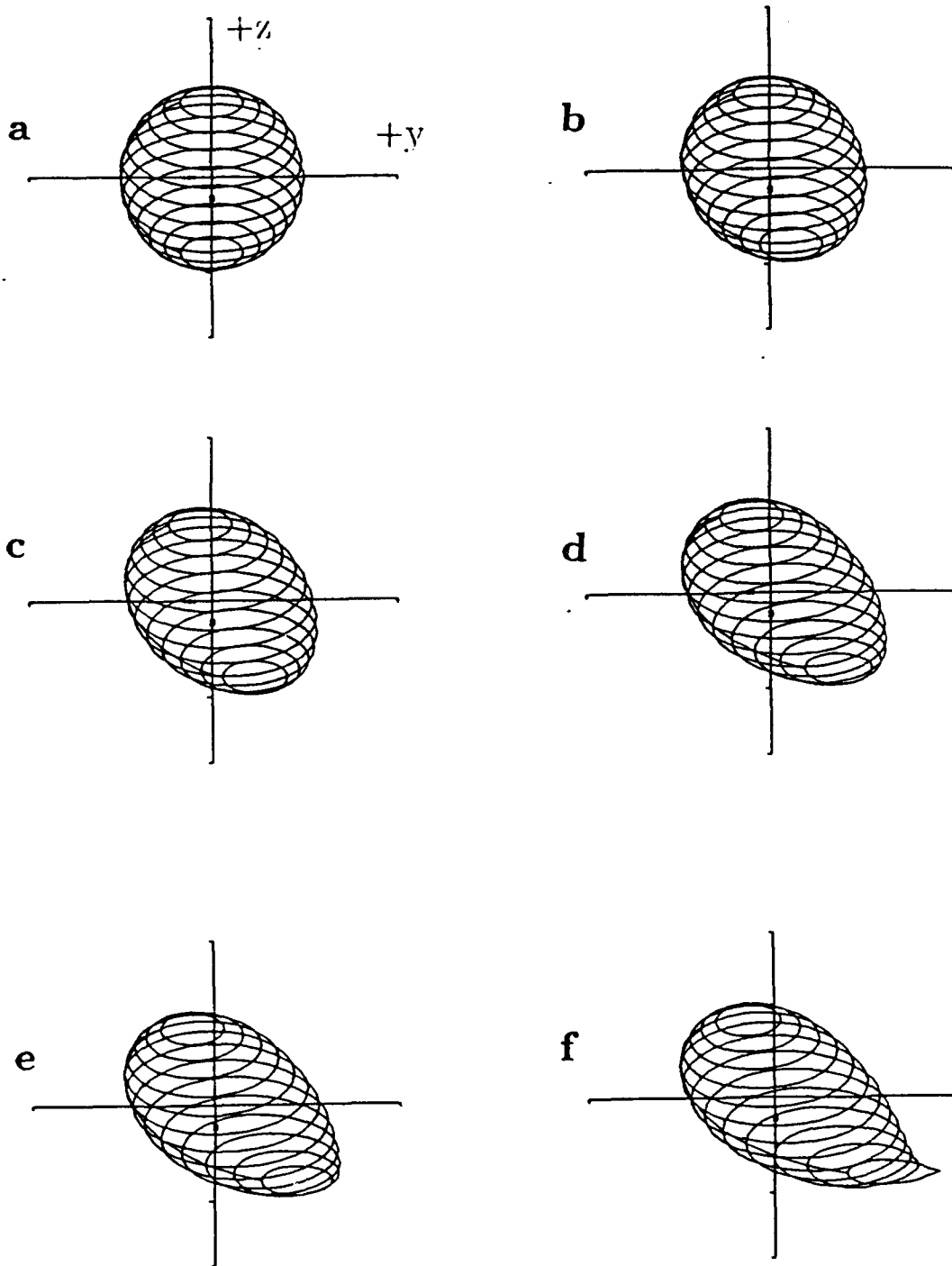


Figure 4.4: A series of steady solutions in which the baroclinicity b is fixed and the vertical shear α is varied. The value of b is set at one, and α is varied from 0.0 to 0.08. In (a) there is no external shear, in (b) $\alpha = 0.02$, in (c) $\alpha = 0.04$, in (d) $\alpha = 0.06$, in (e) $\alpha = 0.07$, and (f) shows the case in which $\alpha = 0.08$. Beyond $\alpha = 0.07$ no solutions were found due to the formation of a cusp on the vortex boundary, which is apparent in 4.4f.

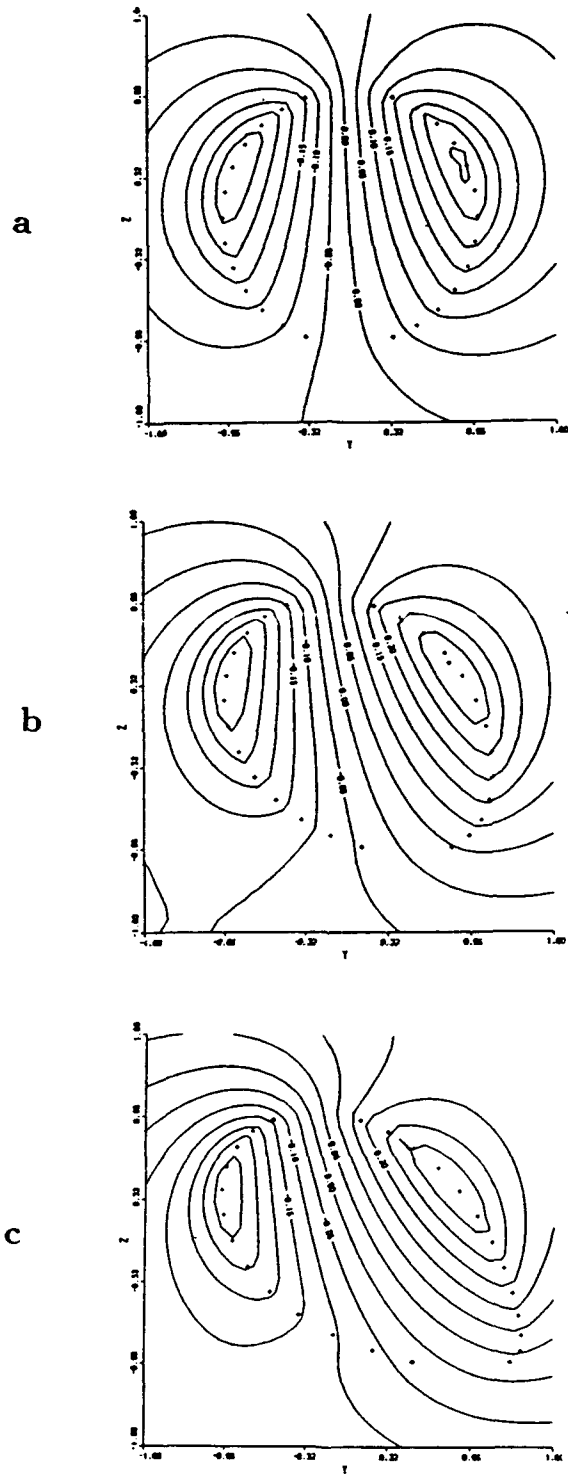


Figure 4.5: Velocity contours showing the azimuthal flow associated with the solutions in 4.4a, 4.4c, 4.4e. The plus signs show the location of the vortex boundary.

beyond $\alpha \approx 0.07$ causes a stagnation point to form on the bottom contour, which has happened in Figure 4.4f.

Figure 4.6 shows a series of solutions in which α is fixed and b is varied. In this case there is little noticeable change in the boundary shape until a critical b is reached ($b \approx 1.7$), beyond which no solutions are found. Figure 4.6h shows an iteration which is in the process of diverging (it 'blows up' after a few more iterations) – notice the sharp boundary deformation near the bottom. This solvability limit appears to be the *same* solvability limit $b < 5/3$ discussed in the linear calculations in Chapter 3. At this limiting b , the basic flow within the core changes sign, and according to linear theory, the boundary perturbation becomes discontinuous. Recall that linear theory predicted impulsive ('spike-like') boundary perturbations, which were of opposite sign above and below the depth at which the basic flow vanished. The fact that the solvability limit is unchanged in the nonlinear calculations indicates that the breakdown of the linear solution is *not* due to the neglect of nonlinear terms, but is a fully nonlinear result, the implication being that the breakdown of the linear solution cannot be remedied by a localized 'patch', as was speculated in the last chapter. Figure 4.7 shows the azimuthal flow for these solutions. Notice that the variation in rotation frequency along the axis of the vortex grows with increasing b . The small rotation frequencies near the bottom of the core are indicated by the spreading of the velocity contours at the bottom.

In Figure 4.8 the region of (α, b) space in which solutions were found is shown. The solution space is bounded by two distinct curves: a horizontal line at the top, and a sloping curve (solid line) to the right. The horizontal line coincides closely with the linear solvability limit $b = 5/3 \approx 1.67$. However, numerical solutions have been found for which b is slightly larger than the limiting value predicted by linear theory ($b \approx 1.70$). This is due to the limited vertical resolution of the numerical solutions. This lack of resolution causes the flow reversal in the core to occur at a slightly different value of b than in the analytical solutions, resulting in a slightly different solvability limit. Numerical runs using variable vertical resolution seem to confirm this hypothesis. Next, for any b there

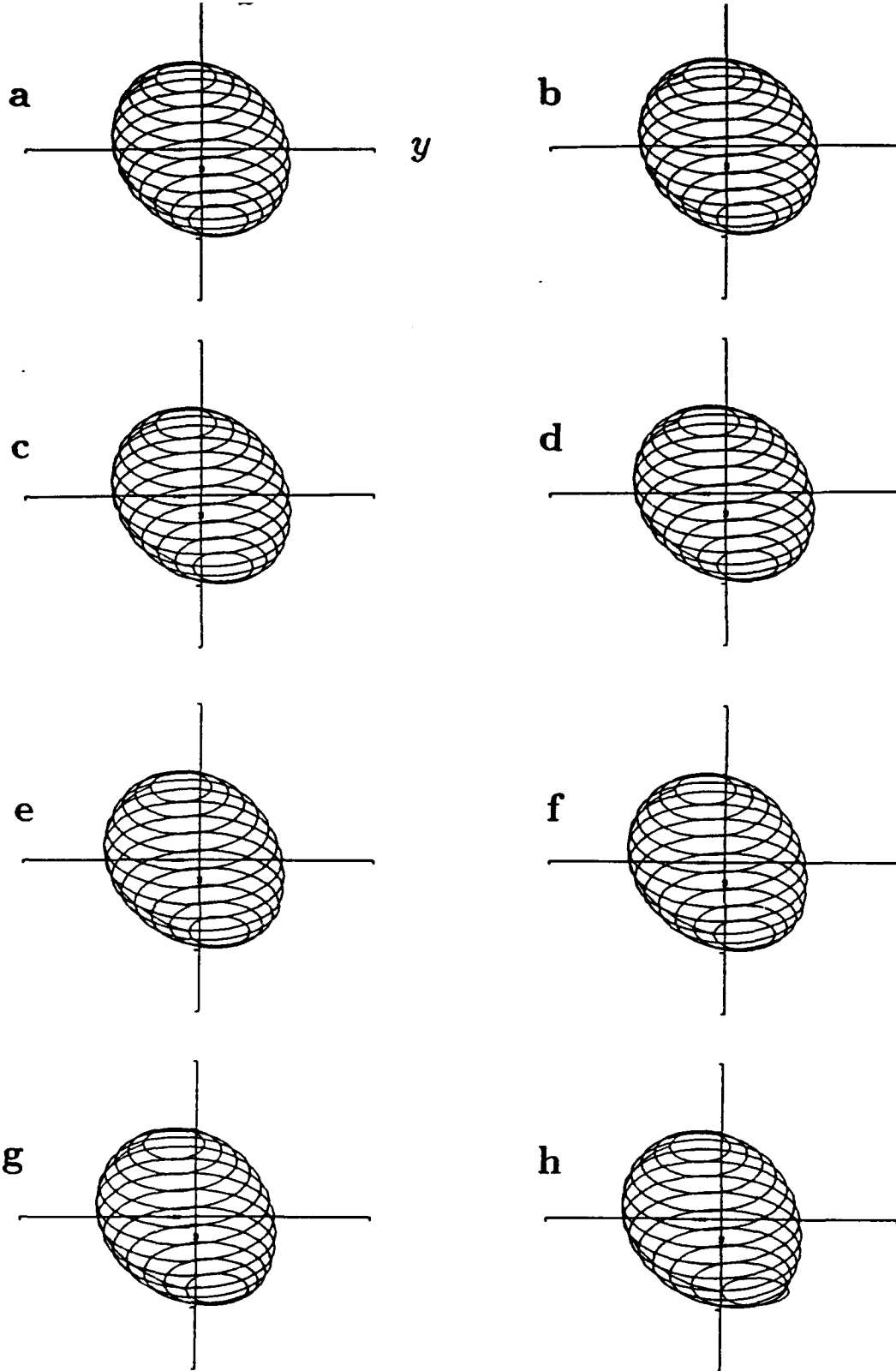
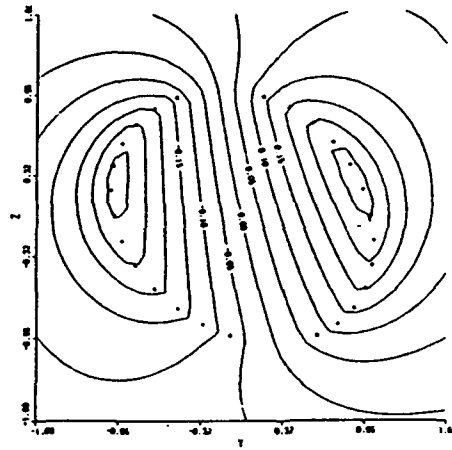
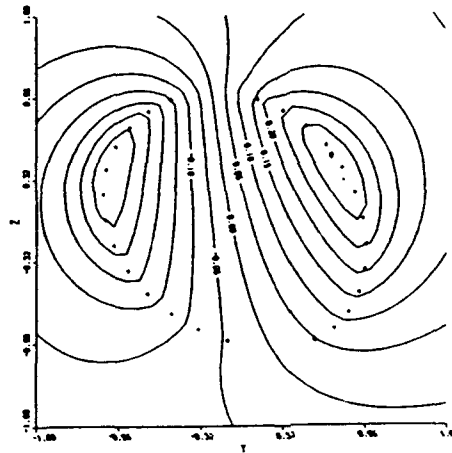


Figure 4.6: Figure 4.6 shows a series of steady configurations for an anticyclonic baroclinic lens in shear. The external vertical shear is fixed at $\alpha = 0.03$, and b is varied from 0.0 to 1.75. In (a) the baroclinicity $b = 0$, in (b) $b = 0.25$, in (c) $b = 0.50$, in (d) $b = .75$, in (e) $b = 1.0$, in (f) $b = 1.25$, in (g) $b = 1.50$, and (h) shows the case in which $b = 1.75$. The last run shown (h) diverged, so this is not a steady solution. The solutions translate through the ambient water as a result of the propagation tendency of the dipolar component of the potential vorticity field.

a



b



c

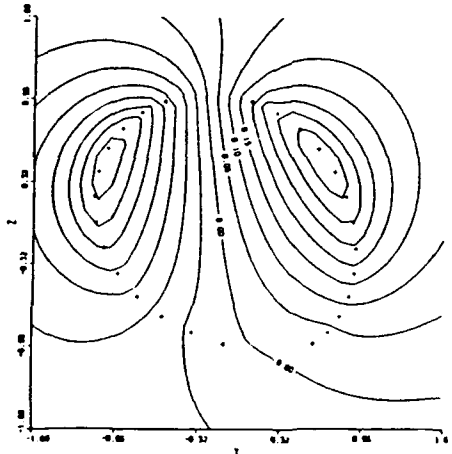


Figure 4.7: The flow associated with the solutions in 4.6c, 4.6e, and 4.6g. The plus signs show the location of the vortex boundary.

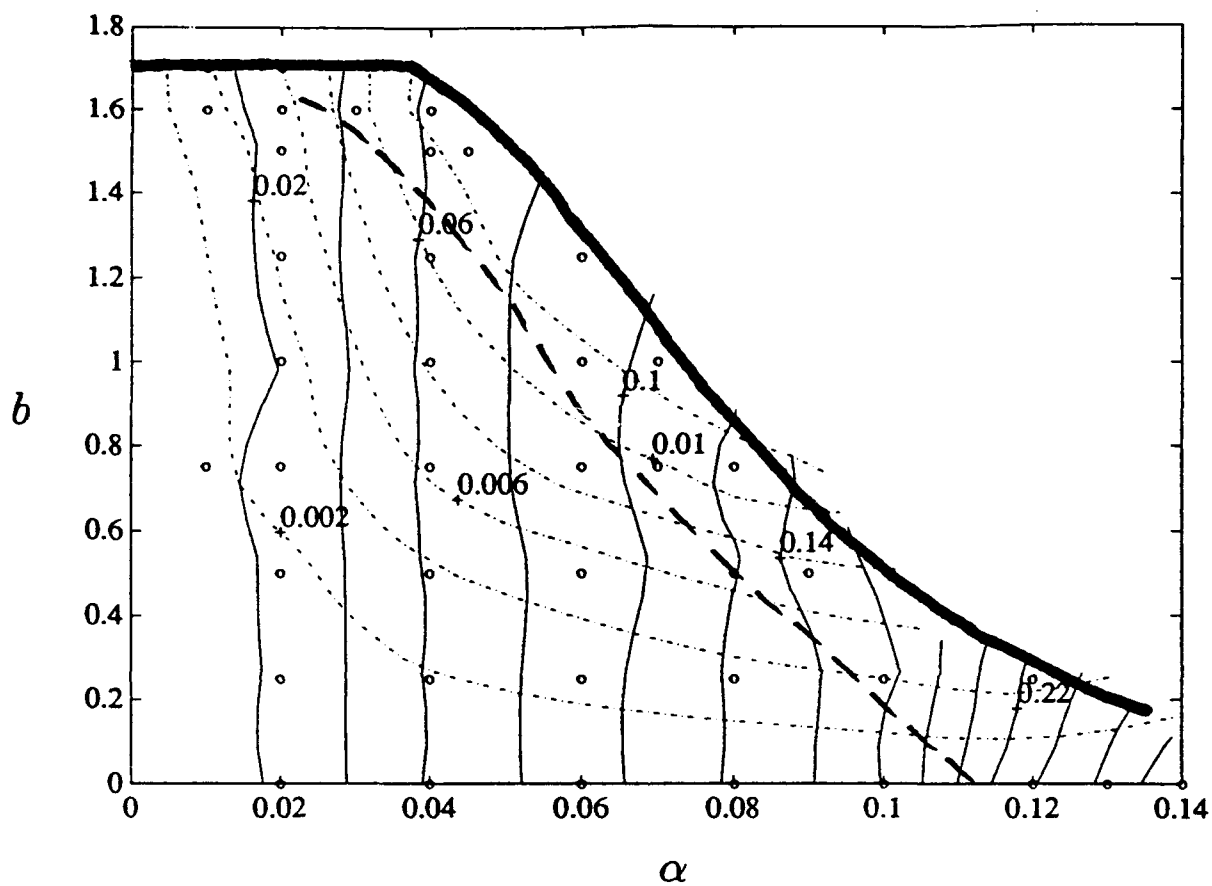


Figure 4.8: Diagram showing the region of the (α, b) plane in which steady solutions have been found. The heavy line represents the solvability limit beyond which no steady solutions can be found; the heavy dashed line is the linear stability limit. The dash/dotted contours show the speeds of the numerical solutions; the solid contour lines show the yz moment of the core volume (see text).

is a maximum shear α beyond which no solutions can be found. This is shown by the sloping line at the right of the figure. A similar solvability limit (maximum shear) was found in the point vortex solutions discussed in Chapter 2, but no limitations on the baroclinicity of the solutions were found. The dashed line shows the location of the linear stability boundary, which will be discussed in detail in the next section. Along the solvability boundary the solutions tend to develop cusps, indicating that a stagnation point has formed on the boundary. The cusps develop first near the depth where the core rotation rate is least – at the bottom of the lens. If the shear is increased beyond this point the external flow dominates the flow within the core, and it is clear that there can be no steady configurations in this case. The tilt of the α solvability limit shown in Figure 4.8 is closely tied to cusp formation: the larger b is, the smaller the rotation frequency at the bottom of the lens will be; the smaller the rotation frequency, the smaller the external flow need be to produce a cusp on the boundary.

The contours shown in Figure 4.8 represent the translation speed of the vortex solutions (dashed lines), and the deformation of the core (solid lines), as measured by the M_{yz} moment of the vortex core. To compare the deformation observed in these solutions with linear theory, a rough integral measure of the boundary deformation is used. In Figure 4.9a the yz moment ($M_{yz} \equiv \tau^{-1} \int_{\text{core}} yz d\tau$) for the numerical solutions is plotted vs that predicted by linear theory. This moment is a measure of the deformation and tilt of the boundary in the yz plane, and is maximum (for a given amplitude) when the boundary is tilted at 45° to the horizontal. Note the good agreement for small α . If α is large, the deformation of the numerical solutions is somewhat larger than linear theory predicts, but no qualitative change in the solution behavior is seen. In Figure 4.9b the speed of the solutions is plotted vs αb . The solid line shows the speed predicted by linear theory: $u_0 = \alpha b/5$. Notice that the agreement with linear theory is very good for all α . The fact that the core deformation is a simple function of α , and the speed a simple function of αb indicates that the speed u_0 can (in principle) be written as a function of the baroclinicity b and the core deformation, in analogy with equation (3.69). The

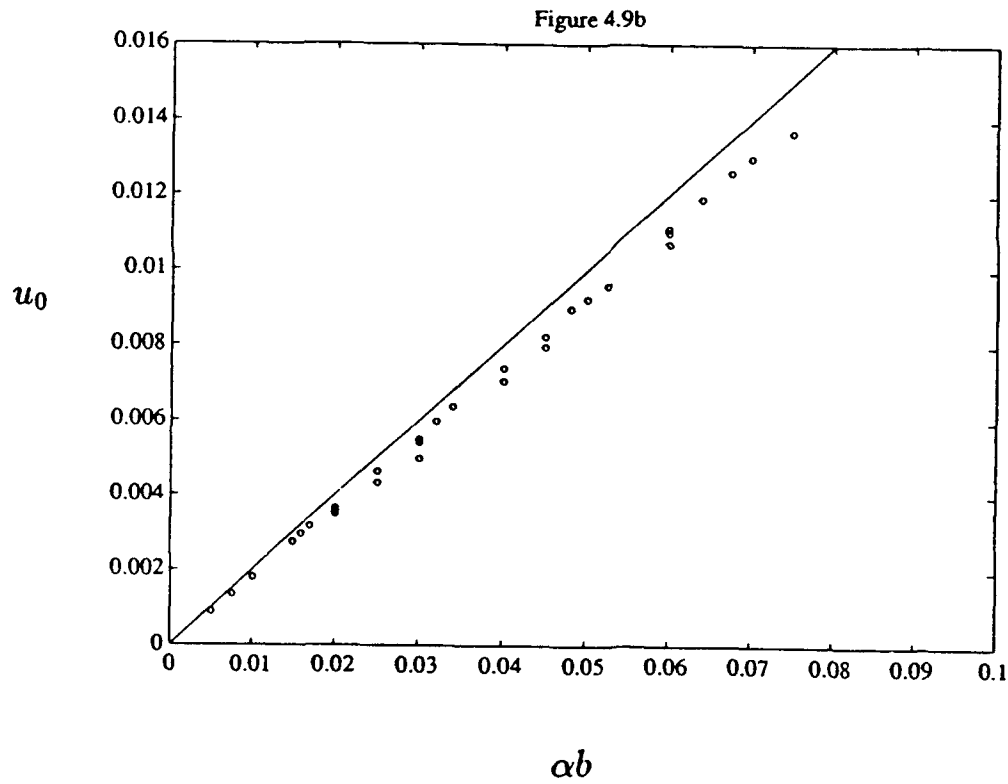
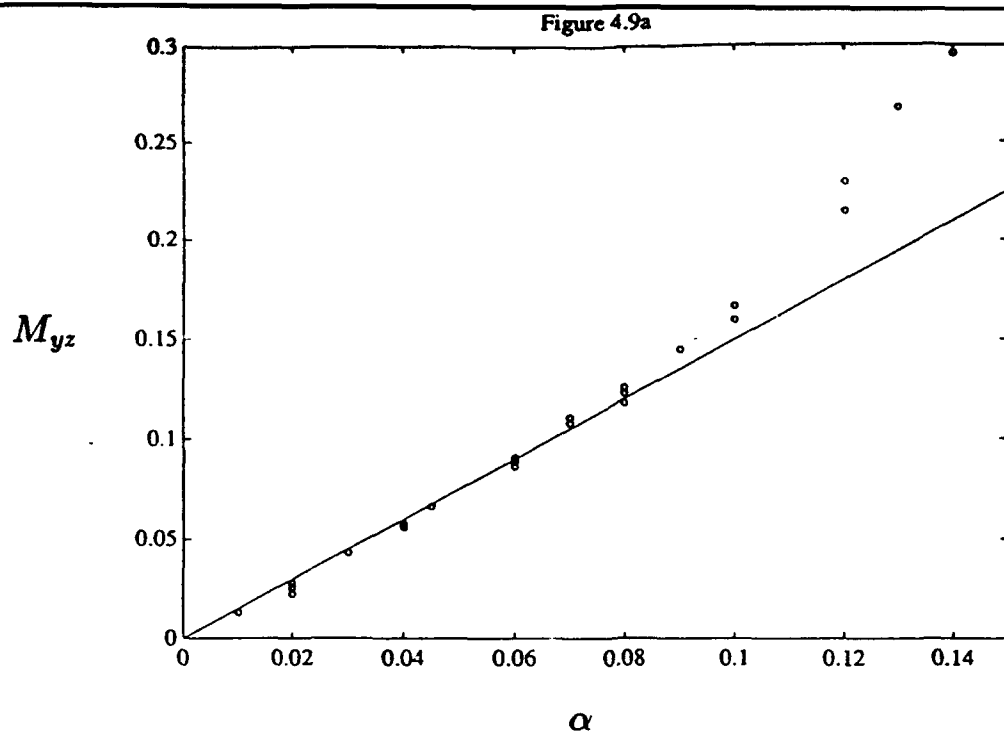


Figure 4.9: In Figure 4.9a the moment M_{yz} (see text) is plotted as a function of α for the numerical and analytical solutions. In 4.9b the vortex translation speed is plotted as a function of the external shear α and the core baroclinicity b . The solid lines represent the predictions of the linear model discussed in Chapter 3.

good agreement between the speeds of the numerical solutions and the predictions of linear theory is surprising, as it extends well into the regime in which nonlinearity might naively be expected to play an important role. This brings into question the role of the nonlinearity in the translation of the vortices. Apparently, either the nonlinearity in the numerical solutions is small enough that they are effectively linear solutions, or else the linear speed is really a fully nonlinear result.

It turns out that the nonlinearity is not necessarily small, which can be shown using the kinematic condition (3.15)

$$\eta_t + u_0(\sin \theta \cos \phi - \frac{1}{r} \cos \theta \cos \phi \eta_\theta + \frac{1}{r} \frac{\sin \phi}{\sin \theta} \eta_\phi) + \psi_\phi / r - \cot \theta \psi_\phi \eta_\theta / r^2 + u_{(\phi)} \eta_\phi / r \sin \theta = 0, \text{ on } r = 1 + \eta. \quad (4.18)$$

Setting $r = 1 + \eta$ and decomposing the streamfunction ψ and the azimuthal velocity $u_{(\phi)}$ into basic state plus perturbation quantities (as in Chapter 3), it follows that (4.18) is given to $O(\eta^2)$ by

$$\eta_t + u_0(\sin \theta \cos \phi - \cos \theta \cos \phi \eta_\theta + \frac{\sin \phi}{\sin \theta} \eta_\phi) + (\psi' + \psi_b)_\phi (1 - \eta) - \cot \theta (\psi' + \psi_b)_\phi \eta_\theta + \underbrace{u_{(\phi)}^\nu \eta_\phi (1 - \eta) / \sin \theta + (u'_{(\phi)} + u_{b(\phi)}) \eta_\phi / \sin \theta}_{= 0} = 0. \quad (4.19)$$

To estimate the nonlinearity of the solutions we can consider the last two (underbraced) terms, which represent the two term expansion of $u_{(\phi)} \eta_\phi / \sin \theta$. In the linear calculations in Chapter 3, this term was represented by the linear term $u_{(\phi)}^\nu \eta_\phi / \sin \theta$. Equation (4.19) shows that the ratio of the nonlinear correction to the linear term is given by

$$\text{MAX}(\eta, u'_{(\phi)} / u_{(\phi)}^\nu(r, \theta)). \quad (4.20)$$

Therefore, the nonlinearity is large if the boundary perturbations are large ($\eta = O(1)$), or if the perturbation velocities are not small compared to the basic flow speeds. It follows that the nonlinearity will be large when the rotation frequency in the core $u_{(\phi)}^\nu / \sin \theta$ is small at some depth, even if the boundary perturbations are not large. This is the case for very baroclinic solutions, in which case the rotation frequency approaches zero near

the bottom. It is clear that $\eta = O(1)$ for some of the solutions shown in Figures 4.3 and 4.4, so that the nonlinearity is of $O(1)$.

It turns out that the good agreement with linear theory apparent in Figure 4.9 is a result of the fact that the linear translation speed $u_0 = \alpha b/5$ is a fully nonlinear result. To show this, recall from Chapter 3 that the speed is defined to be the translation speed of the center of potential vorticity of the lens:

$$u_0 \equiv \frac{d\overline{q_v \bar{x}}}{dt} = \frac{d}{dt} Q^{-1} \int_{\text{core}} q_v \bar{x} d\tau = Q^{-1} \int_{\text{core}} q_v u d\tau, \quad (4.21)$$

where

$$Q \equiv \int_{\text{core}} q_v d\tau. \quad (4.22)$$

It should be emphasized that the speed was defined in this fashion because u_0 (as defined by (4.21)) is a constant – even if the flow is unsteady. Thus (4.21) is the most appropriate definition for the translation speed of the solutions, since it is readily generalized to unsteady flows. If the alternative definition $u_0 \equiv \frac{d\bar{x}}{dt}$ had been used, we would have found that the translation speeds were the same as those given by (4.21) in the steady limit, but that the translation speed would in general have some periodic component superimposed if the flow was unsteady. This can be seen from the relation

$$\bar{x} = -\overline{q_v \bar{x}} - b\bar{x}\bar{z}, \quad (4.23)$$

which is easily derived if one recalls that $q_v = -1 - bz$. Thus, the volumetric center of the core differs from the negative of the ‘center of potential vorticity’ by a term which measures the ‘tilt’ of the boundary in the xz -plane. Because this term is *periodic* in time for unsteady solutions, while $\overline{q_v \bar{x}}$ will be shown momentarily to be secular in time, $\frac{d\bar{x}}{dt}$ will in general be a periodic function of time.

Using the definition (4.21), the close agreement between the numerical solutions and the linear theory can be explained by noticing that only the external flow u_b contributes to the integral (4.21); the contribution from the internal flow vanishes identically.

Using (4.12) the zonal velocity can be written in the form

$$u = u_b - \frac{1}{4\pi} \int \frac{q_v(x_0, y_0, z_0)(y - y_0)}{((x - x_0)^2 + (y - y_0)^2 + (z - z_0)^2)^{3/2}} d\tau_0. \quad (4.24)$$

It follows that the integral in (4.21) can be written

$$Q^{-1} \int_{\text{core}} q_v u d\tau = Q^{-1} \int_{\text{core}} q_v u_b d\tau - \frac{1}{4\pi Q} \int \int_{\text{core}} \frac{q_v(x, y, z) q_v(x_0, y_0, z_0)(y - y_0)}{((x - x_0)^2 + (y - y_0)^2 + (z - z_0)^2)^{3/2}} d\tau_0 d\tau, \quad (4.25)$$

where both volume integrations (with respect to τ and τ_0) are carried out over the core region. The symmetry properties of the integrand show that the second integral on the right side of the equation vanishes. This is due to the fact that the sign of the integrand changes if the subscripted and unsubscripted variables are interchanged. Thus, if the integrand is written as the function $\xi(x, y, z | x_0, y_0, z_0)$, the contribution to the integral from the elemental volume at $(x, y, z | x_0, y_0, z_0)$ exactly cancels that from $(x_0, y_0, z_0 | x, y, z)$ for all $(x_0, y_0, z_0 | x, y, z)$ inside the core⁶. This demonstrates that the contribution to the integral from the mutual interactions of *any* two elemental volumes vanishes. Therefore, the second integral vanishes identically and (4.21) reduces to

$$u_0 = Q^{-1} \int_{\text{core}} q_v u_b d\tau. \quad (4.26)$$

This shows that in the absence of external flow ($u_b = 0$), the 'center of potential vorticity' of the lens must remain fixed. Finally, because the external flow is purely zonal ($v_b = 0$) the lens can only move in a zonal direction, since $Q^{-1} \int_{\text{core}} q_v d\tau$ vanishes identically.

The next step is to show that the expression for u_0 obtained by evaluating (4.26) has the same functional form in the linear and nonlinear cases. Because q_v and u_b depend only on z , carrying out the integrations in x and y gives

$$u_0 = Q^{-1} \int_{-1}^{+1} q_v(z) u_b(z) A(z) dz, \quad (4.27)$$

where $A(z)$ is the area enclosed by the horizontal contour at depth z . Now consider a family of steady solutions in which $q_v(z)$ is fixed and α is varied. Notice that $A(z)$ is the

⁶This result does not depend upon any symmetry properties of the boundary, or upon the solutions being steady, but only upon the fact that both integrations (with respect to τ and τ_0) are carried out over the entire core volume.

same for all of these solutions, since the area within each contour is preserved through the iteration process. Using the definitions $u_b = \alpha z$ and $q_v = -1 - bz$, (4.27) can be rewritten

$$u_0 = -\frac{\alpha}{Q} \int_{-1}^{+1} z A(z) dz - \frac{\alpha b}{Q} \int_{-1}^{+1} z^2 A(z) dz. \quad (4.28)$$

The first integral vanishes because $A(z)$ is symmetric (so the integrand is odd) for the spherical initial boundary shape considered here, so that

$$u_0 = -\frac{\alpha b}{Q} \int_{-1}^{+1} z^2 A(z) dz. \quad (4.29)$$

Notice that neither Q nor the integral in (4.29) change as α is varied, even if the boundary of the vortex boundary becomes very distorted. Therefore, the term $Q^{-1} \int z^2 A(z) dz$ must be as given by linear theory (see the Appendix), and evaluating (4.29) gives

$$u_0 = -\frac{1}{5} \alpha b. \quad (4.30)$$

The minus sign in (4.30) appears because of the minus sign that was introduced into the definition of $q_v(z)$ (see (4.5)). Thus, the translation speed (4.30) is a fully nonlinear result, which explains the good agreement between the linear speeds and those of the numerical solutions.

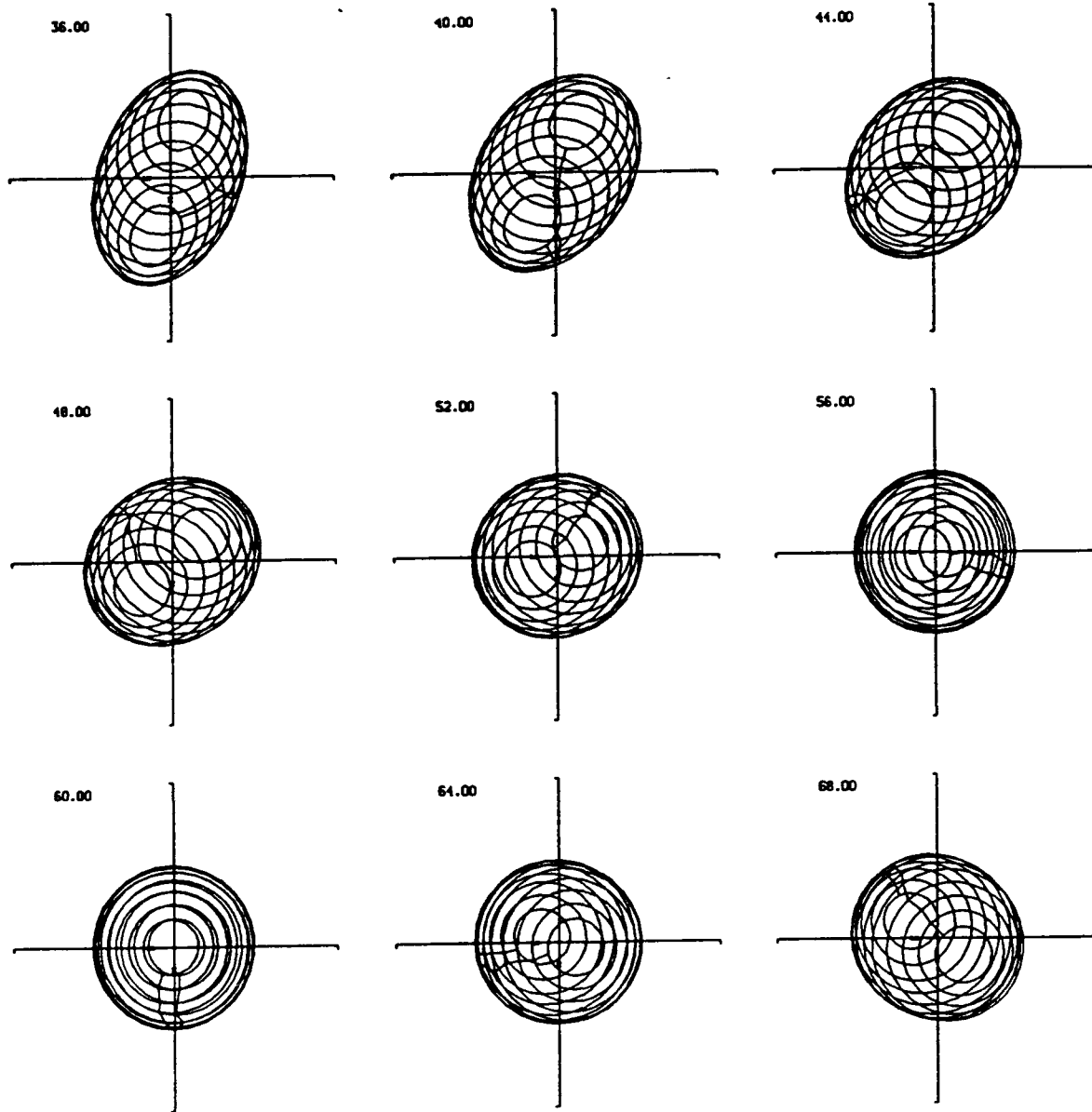
The propagation speed (4.30) may be thought of as a weighted average of the external flow speed over the core region (as in (4.30)), or else as the external flow velocity advecting the center of potential vorticity of the lens. However, the physical reason for the translation is the modon propagation tendency associated with the self-interaction of the baroclinic component of the potential vorticity field, as discussed in Chapter 3. The propagating point vortex pairs considered in Chapter 2 were interpreted in a similar fashion – as barotropic pairs with a dipole component superimposed. It was shown there that the translation of the pairs could be explained by the tendency of the dipolar component of the field to self-propagate. A major difference is that in the present case there is a maximum baroclinicity b for which such solutions can be found, so that the propagation speed of the continuous solutions always lies within the range of the

external flow speeds advecting the core. For large αb values, the propagation speed of the numerical solutions lags very slightly behind the linear speed. This discrepancy is due to a numerical error associated with the fact that at large αb (when the boundary perturbations may become quite sharp) the boundary is consistently less well resolved near the bottom than at the top. This can lead to a systematic computational error in the relative volumes of the upper and lower halves of the vortex, and hence to a slightly different translation speed.

Initial Value Runs: Stability

To investigate the relationship between steady and unsteady behavior, a numerical run will be shown for which the vortex is not initially close to an equilibrium. Figure 4.10 shows an integration in which an initially spherical, anticyclonic monopole ($b = 0$) is placed in an external shear $\alpha = 0.05$. Initially, the evolving boundary perturbation reflects the advection by the external flow. Further along in the integration, the boundary perturbation begins to precess in a clockwise sense, as predicted by linear theory, and is in a tilted configuration qualitatively like those shown in Figure 4.3 after a time $t \approx 30$. The boundary continues to precess, and after a time $t \approx 60$ is once again in its initial configuration. Thus, the motion is apparently periodic, with the lens being alternately stretched out and recompressed by the external flow. The period of the motion is about three times the rotation period of a fluid parcel in the core. On average, however, the lens is tilted in a direction transverse to the external flow, just as the steady solutions are. In Chapter 3 it was shown that such time dependent solutions can be thought of as steady, forced solutions with a freely precessing component superimposed.

The fact that the only steady solutions that exist when $|b| \geq 5/3$ are perfectly spherical vortices with zero external shear leads one to question the stability of these solutions. The analysis in Chapter 3 showed that there were no exponentially growing modes, but the impulsive nature of the boundary perturbations seems to indicate some form of instability. Therefore, the stability of these highly baroclinic solutions will be re-examined numerically. Figure 4.11 shows that when the vortex is given a small initial



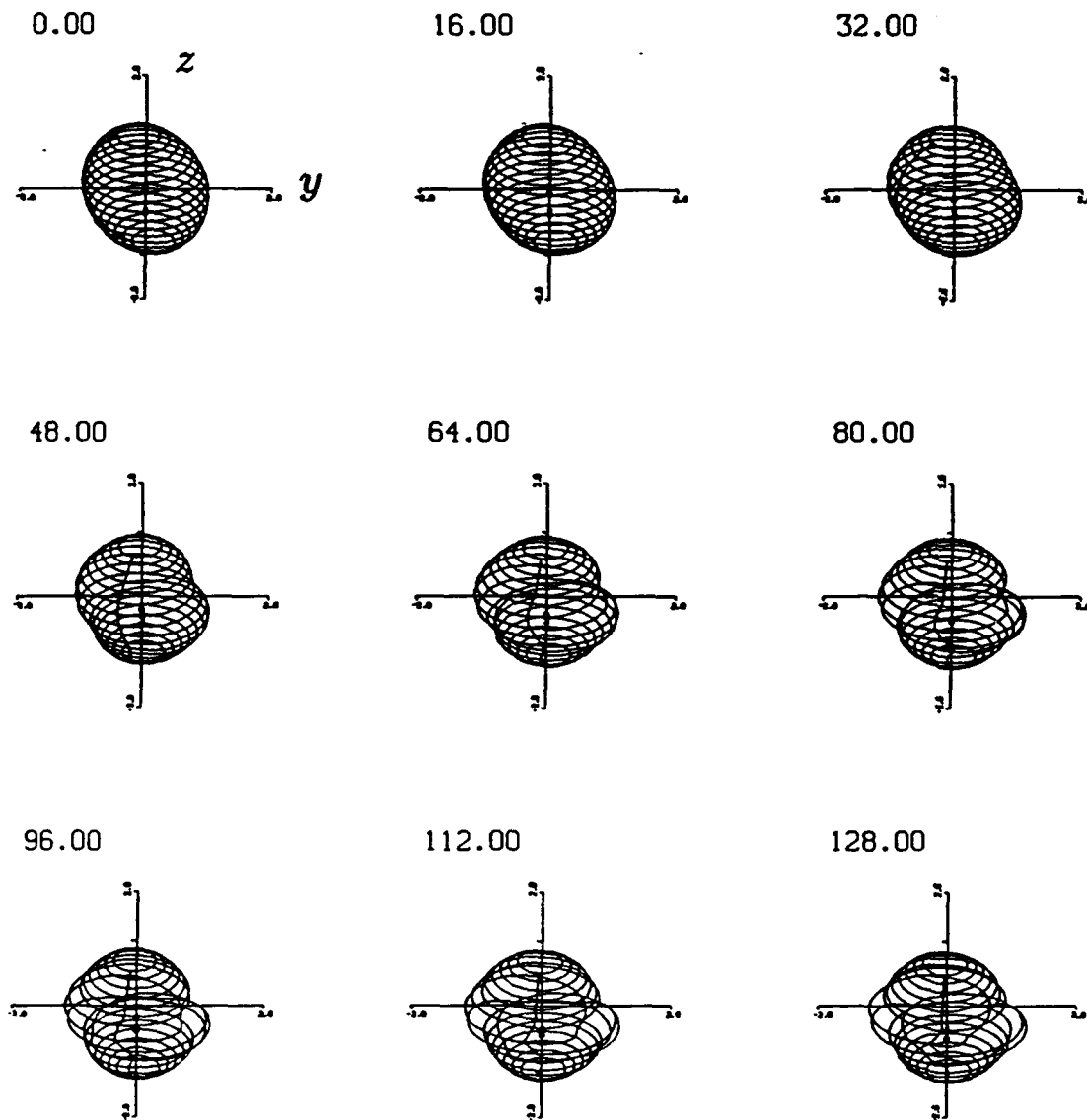
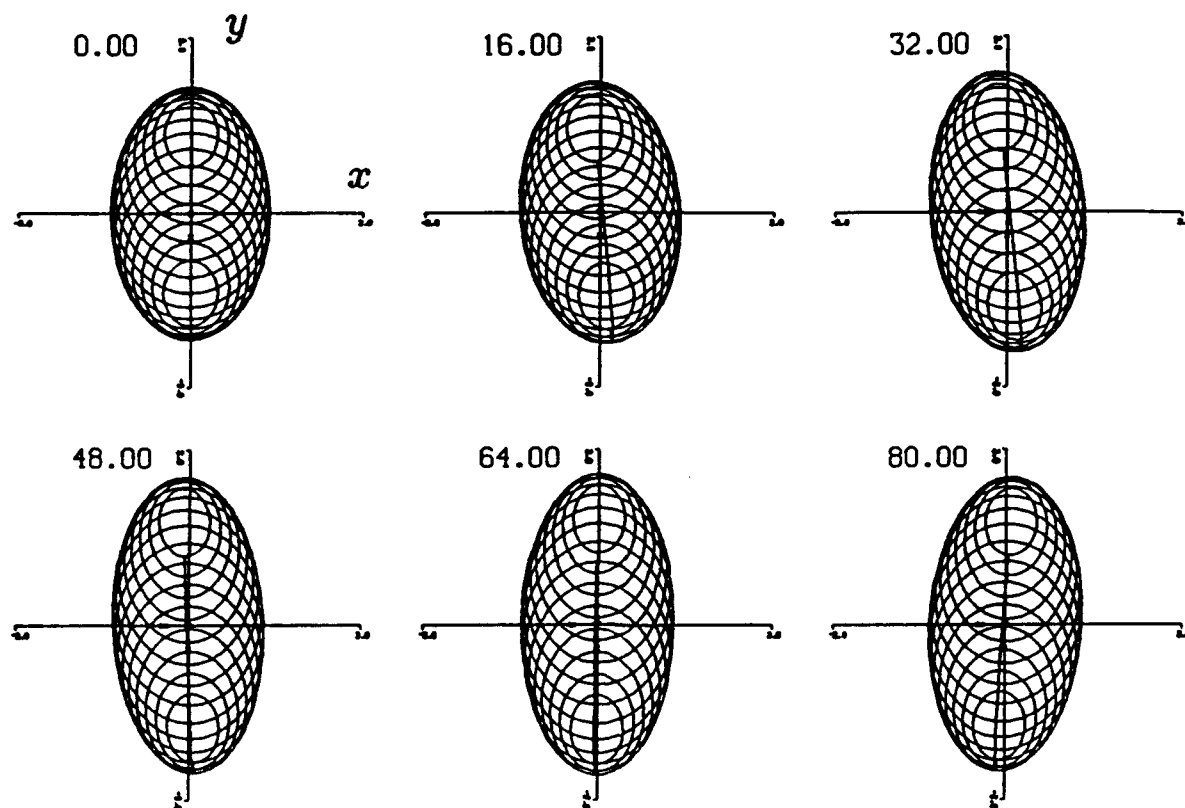


Figure 4.11: Plot of a forward run for a purely baroclinic vortex in a quiescent fluid. When perturbed with a (1,2) boundary perturbation, the vortex quickly evolves into a state qualitatively like that predicted by linear theory, characterized by large boundary deformations near the level at which the basic flow changes sign.

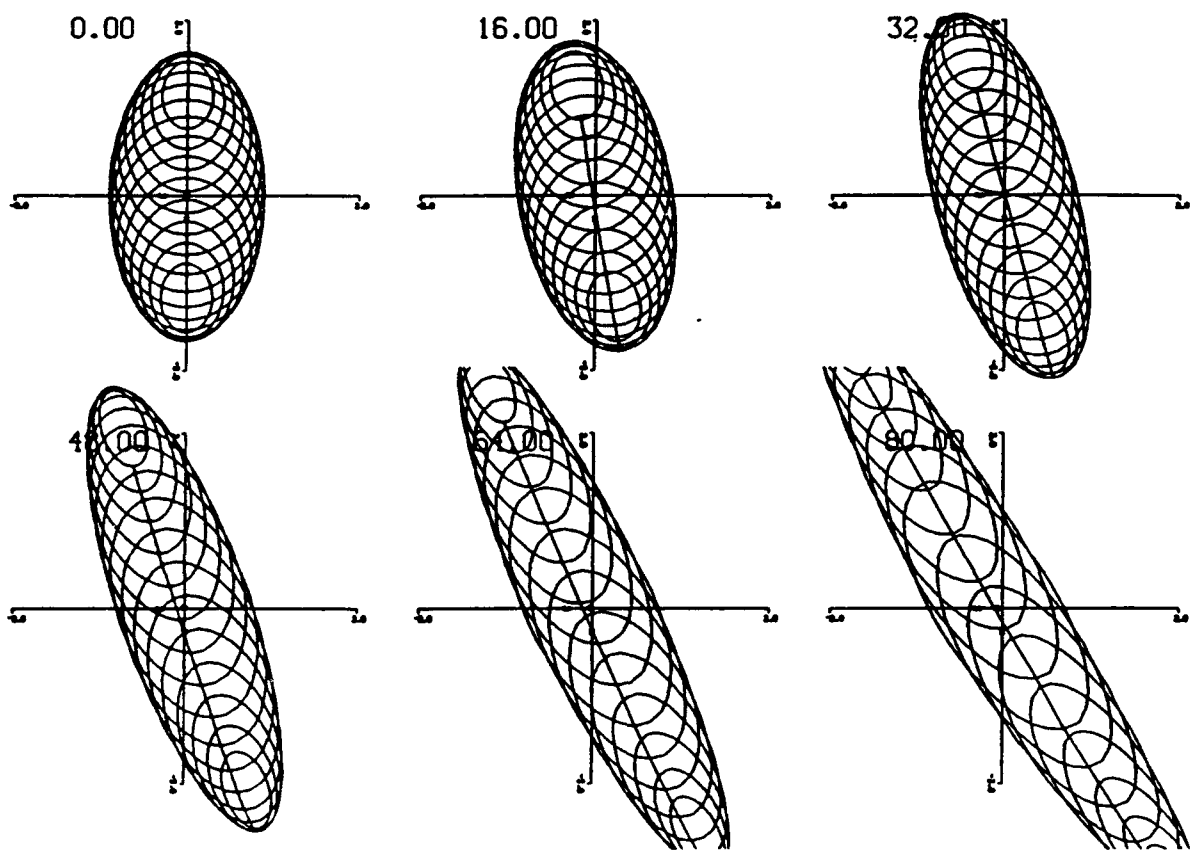
perturbation of the form $\epsilon \sin 2\theta \sin \phi$ (representing a tilted ellipsoidal perturbation), the boundary evolves into one with slab-like extrusions of core fluid near the middle of the lens. As time goes on the boundary becomes increasingly deformed, and eventually appears to be evolving toward a state like that predicted by linear theory (see Figure 3.7b). When the integration is stopped, the boundary perturbations have become large on either side of the point where the basic flow in the core changes sign. As discussed in Chapter 3, this behavior is due to the presence of a steering level at the depth where the basic flow changes sign.

To investigate the stability of the steady solutions with respect to small perturbations, a series of numerical integrations will now be shown. In each of these runs the vortex boundary is represented by 17 layers, with 40 points on each layer. At each time step, the points on each contour are redistributed so that they are evenly distributed. Figure 4.12 shows a series of forward runs which examine the stability of some of the steady solutions. It is found that the perturbed solutions either settle into a periodic motion, or else a certain amount of core fluid is torn off by the external flow before they (presumably) reach some new equilibrium. Limitations of the numerical procedure used do not allow an exploration of the form of the new equilibrium. Attention is focused on solutions which are close to the solvability limit shown in Figure 4.8, as we wish to determine whether there is a linear stability limit within the solvability region. It is found that the stability boundary is different from the solvability boundary, as shown in Figure 4.8. The solutions are perturbed by varying the external shear slightly from the equilibrium value. The perturbations were small in the sense that the variation of the external shear was very much smaller than the equilibrium shear ($\Delta\alpha/\alpha \ll 1$). For a baroclinic vortex, varying the shear produces a boundary perturbation which is a combination of many normal modes, so it is likely that any unstable modes will be present. Because the linear calculations showed the basic state to be stable when $|b| < 5/3$, we have no information on the possible growth rates of unstable modes. Therefore, the integrations were continued until it became reasonably clear that the vortex had (a) settled into a periodic

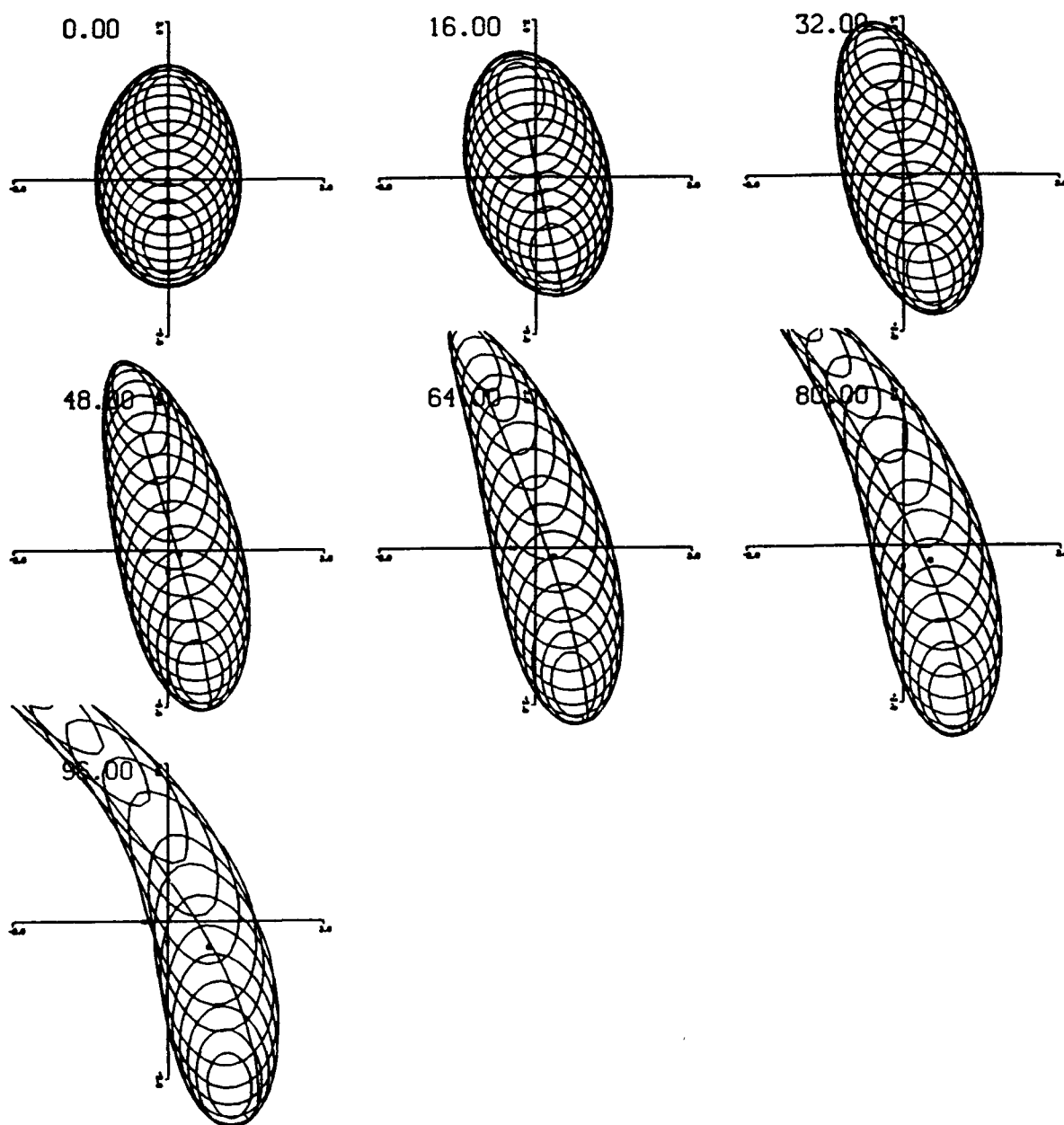


a: $\alpha = 0.10, b = 0.00$

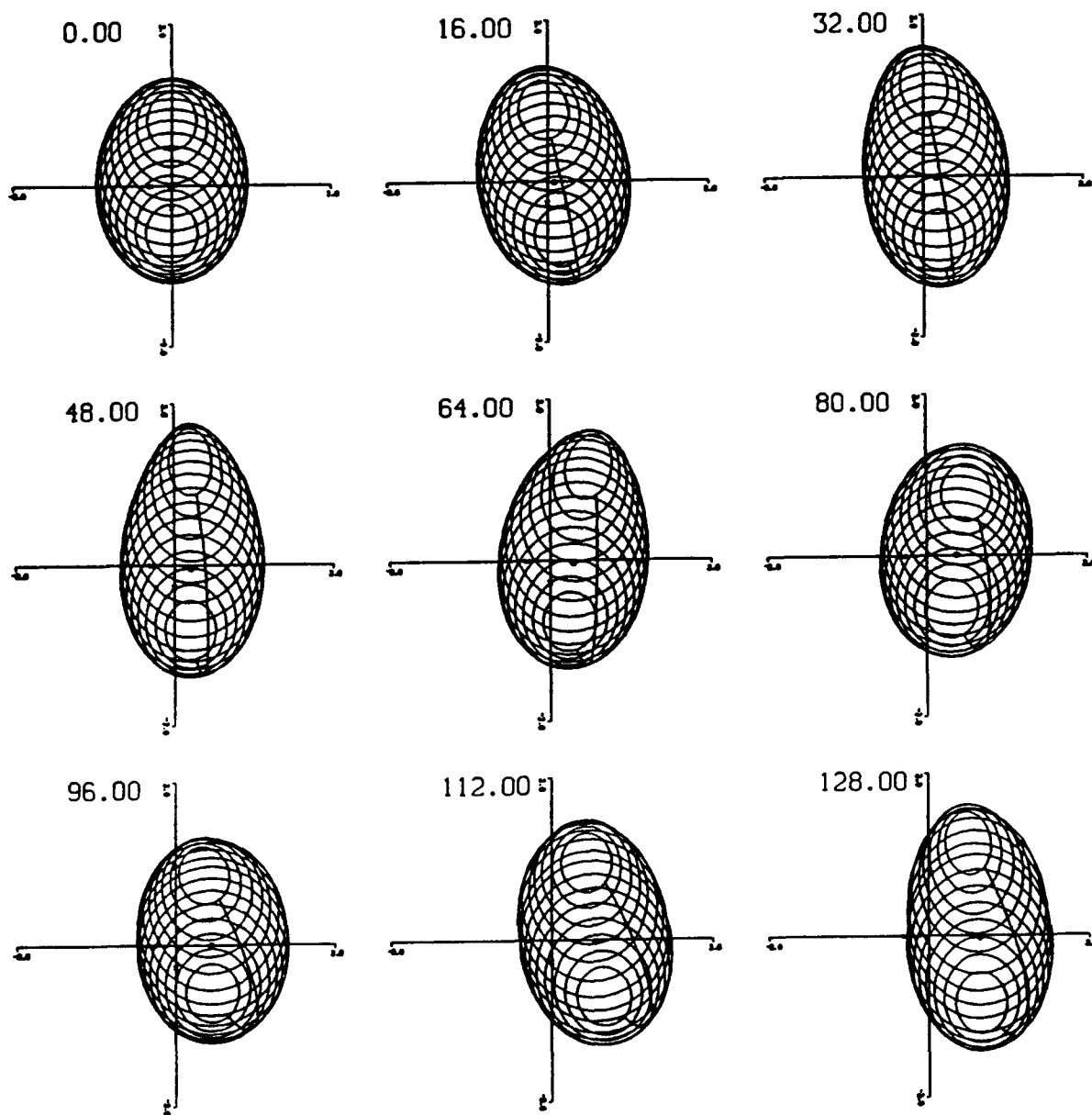
Figure 4.12: A series of forward runs using the numerical steady solutions as initial conditions. The solutions have been perturbed by varying the external shear slightly ($\Delta\alpha/\alpha \ll 1$). The initial conditions for these runs are close to the solvability limit shown in Figure 4.8. The numbers shown beneath each plot give the values of α and b for the basic state solution. The first two frames show runs representing purely monopolar vortices, while the baroclinicity b gets progressively larger in the remaining frames. For small external shears the perturbed numerical solutions behave like the steady solutions, with a small time dependent component superimposed. For larger shears, the perturbed solutions may be unstable, in which case they are 'pulled apart' by the external flow.



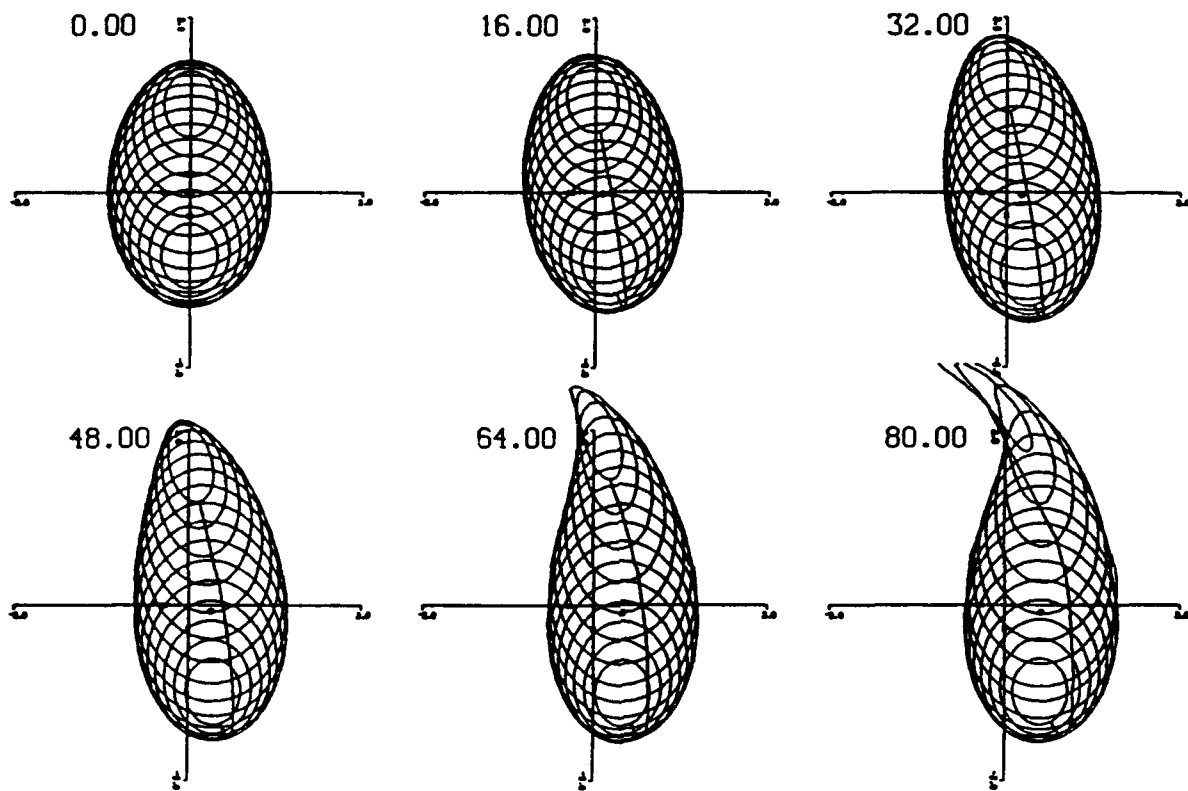
b: $\alpha = 0.12$, $b = 0.00$



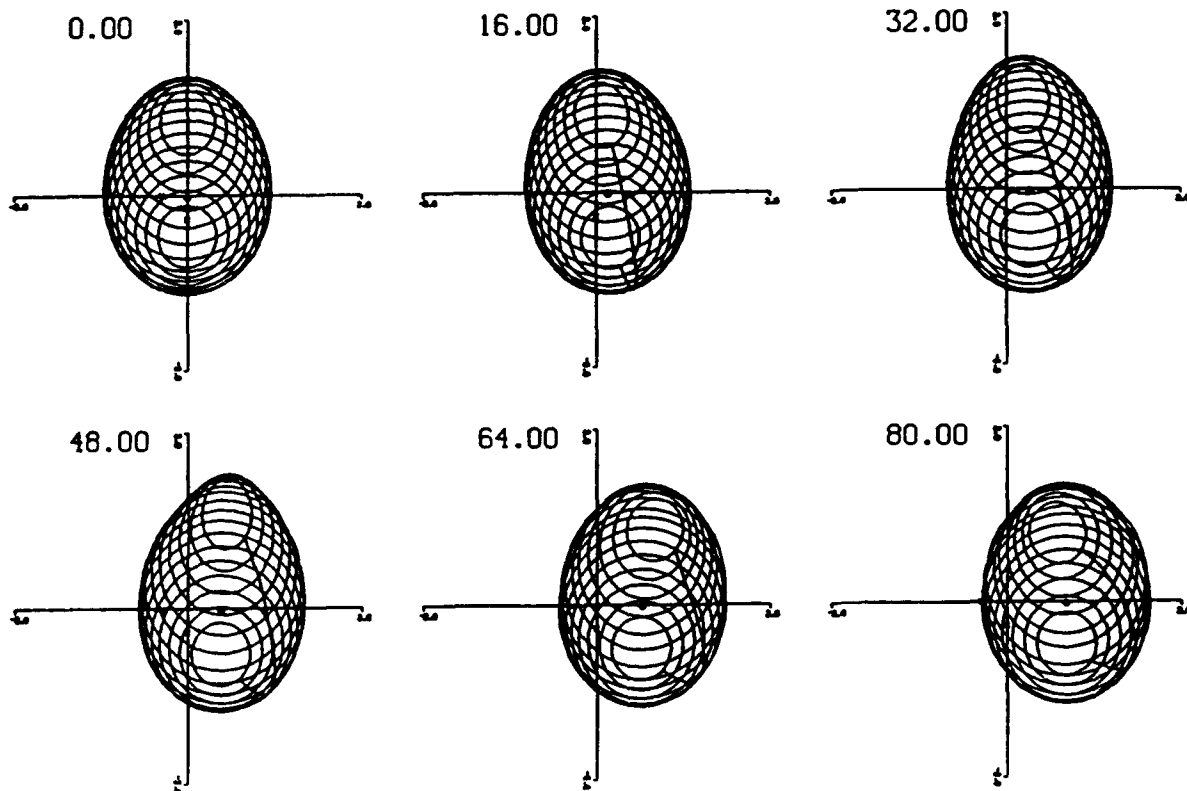
c: $\alpha = 0.11$, $b = 0.10$



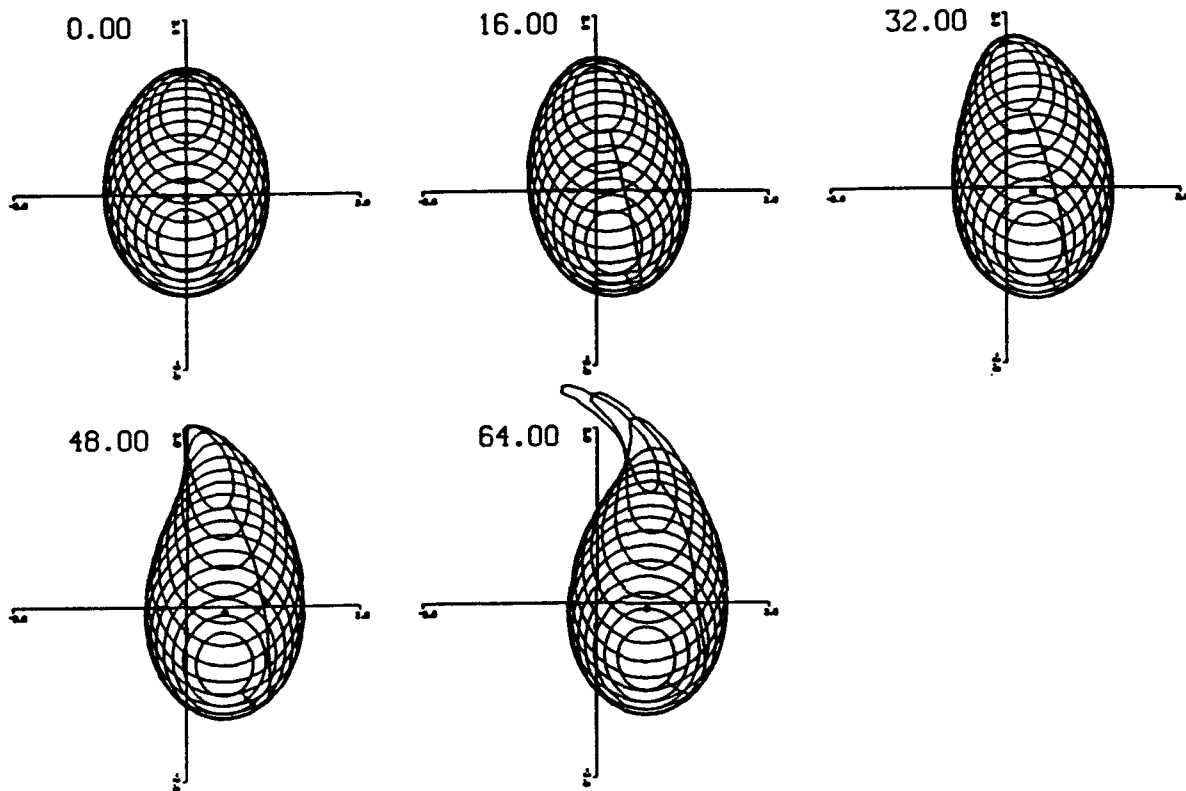
d: $\alpha = 0.09$, $b = 0.25$



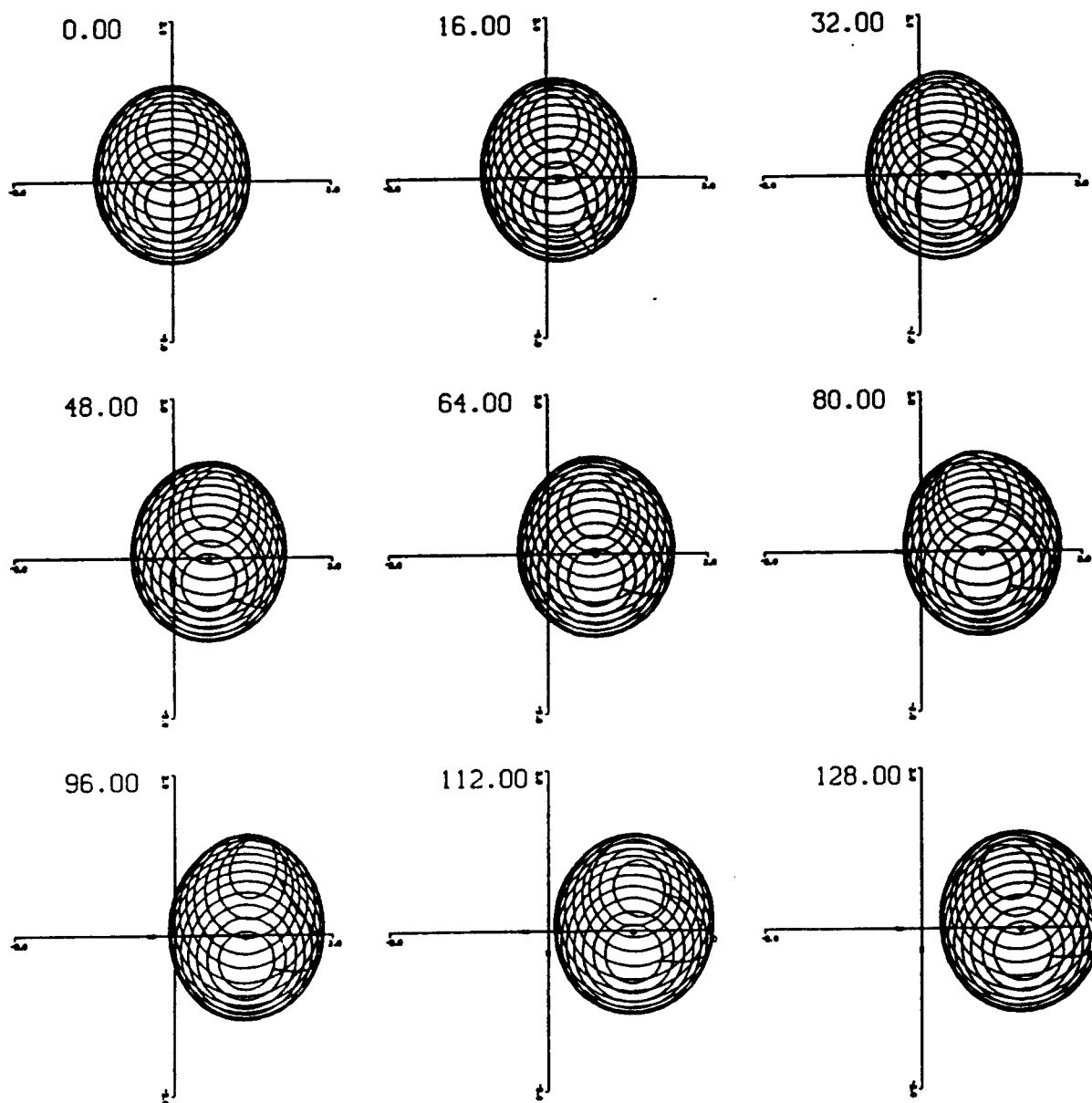
e: $\alpha = 0.10$, $b = 0.25$



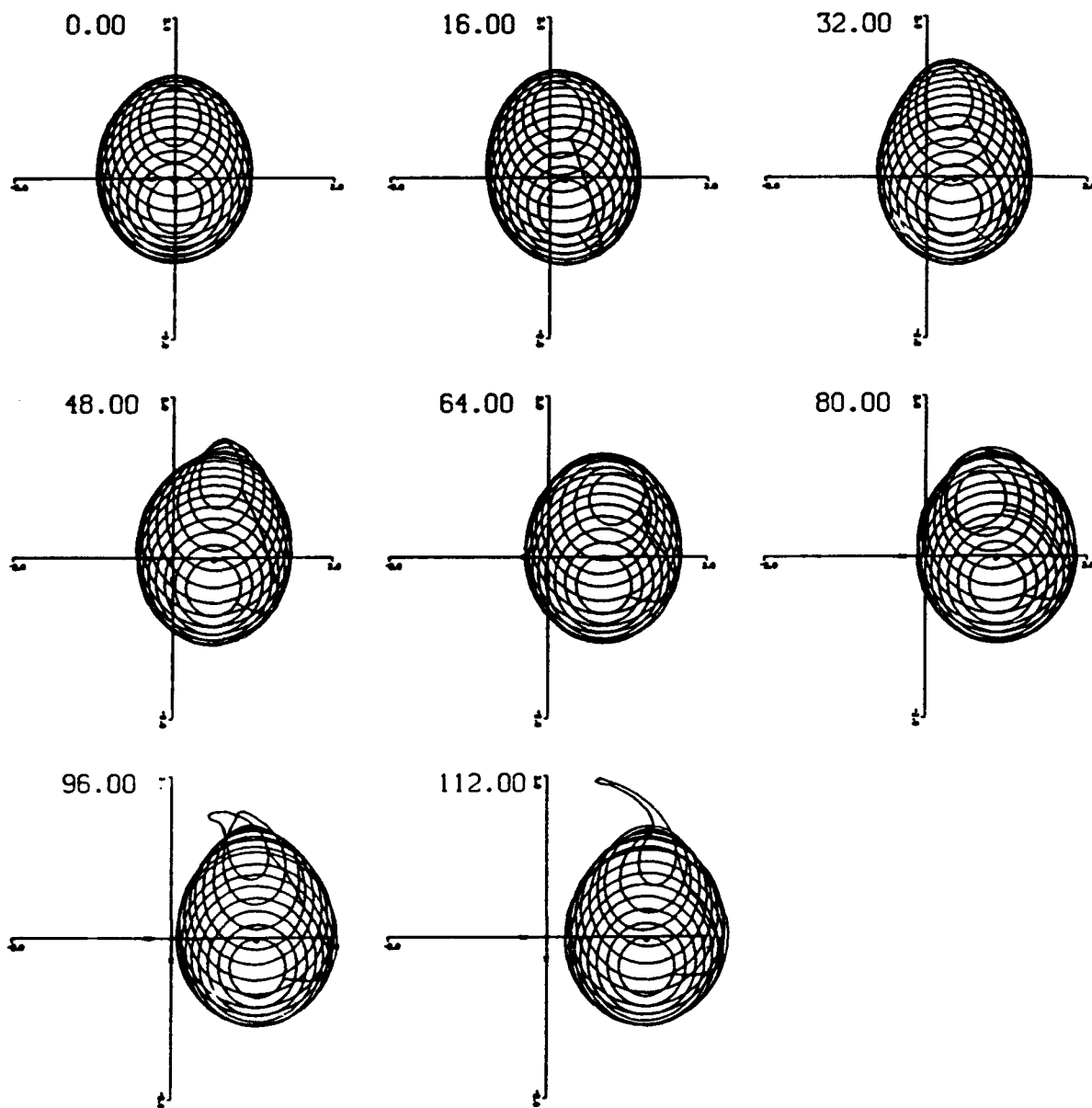
f: $\alpha = 0.08$, $b = 0.50$



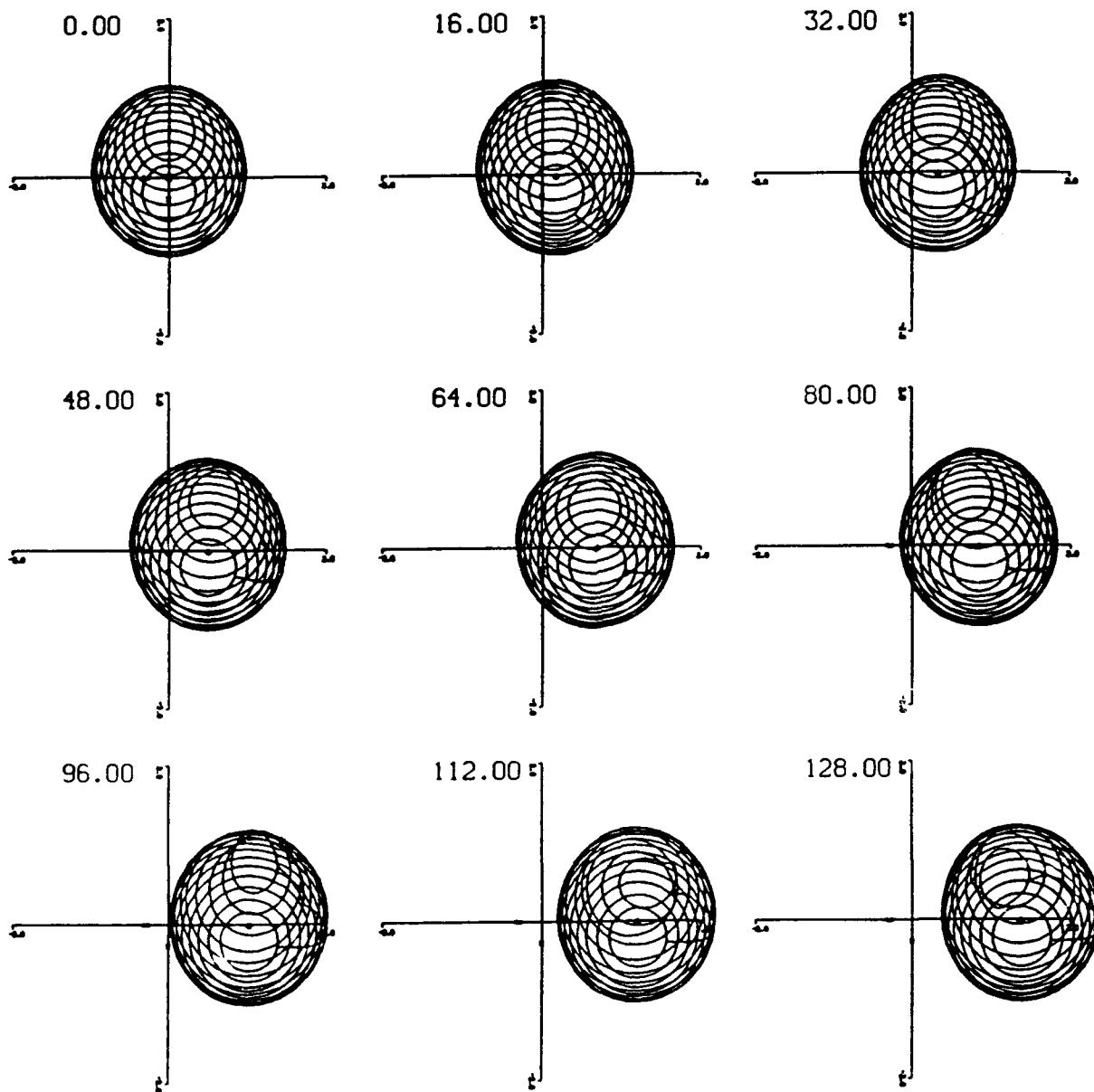
g: $\alpha = 0.09$, $b = 0.50$



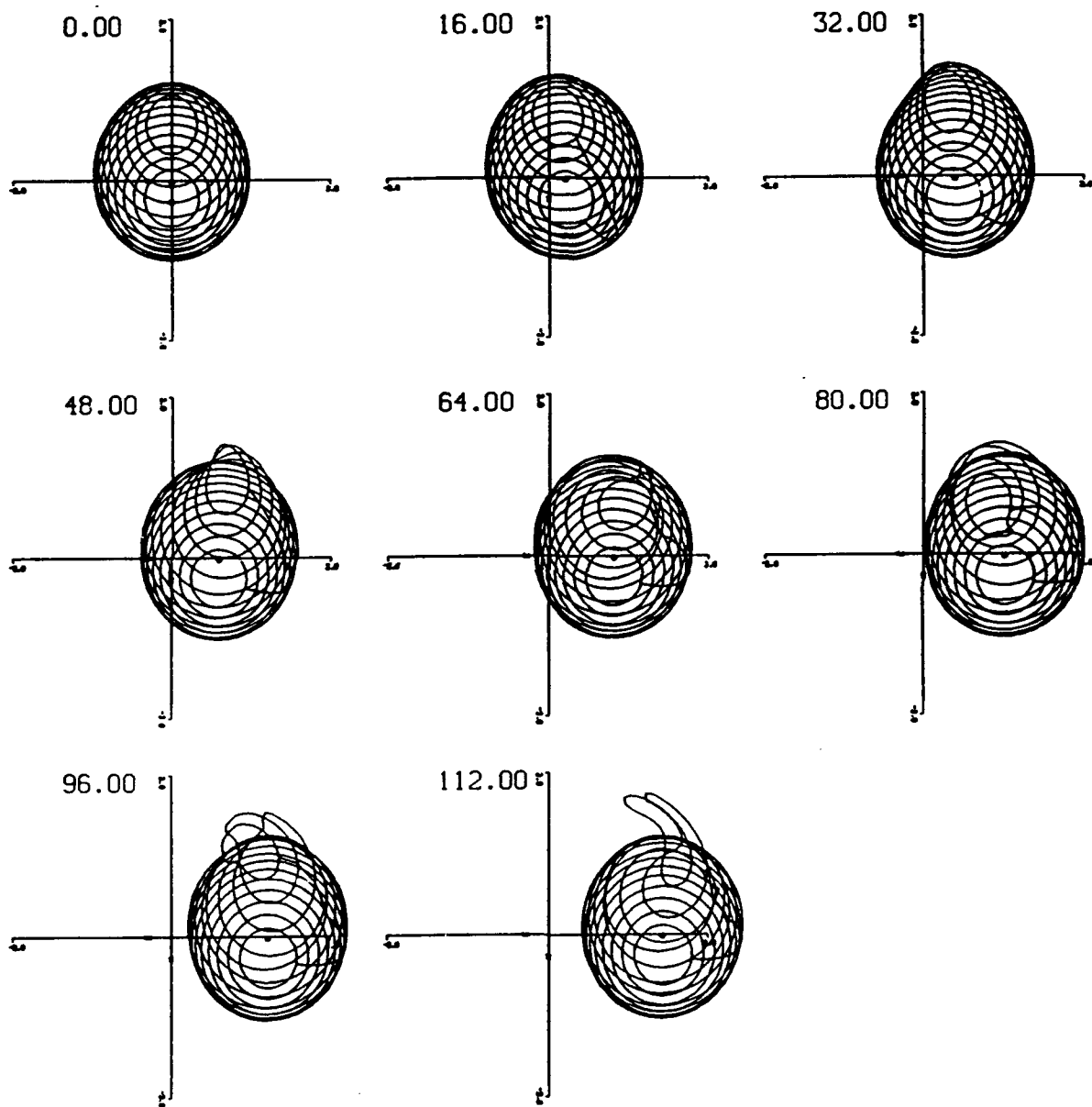
h: $\alpha = 0.06$, $b = 0.75$



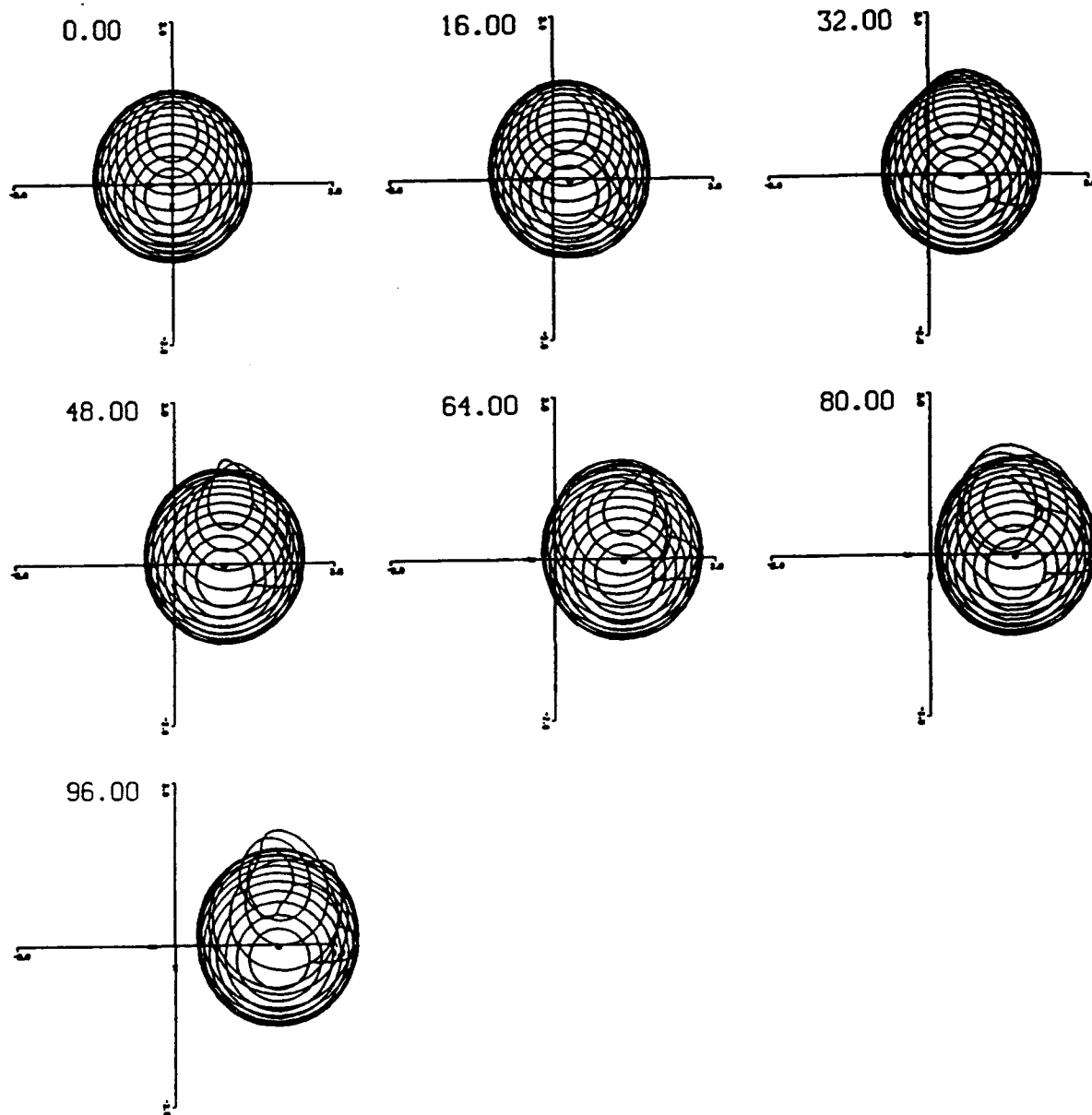
i: $\alpha = 0.07, b = 0.75$



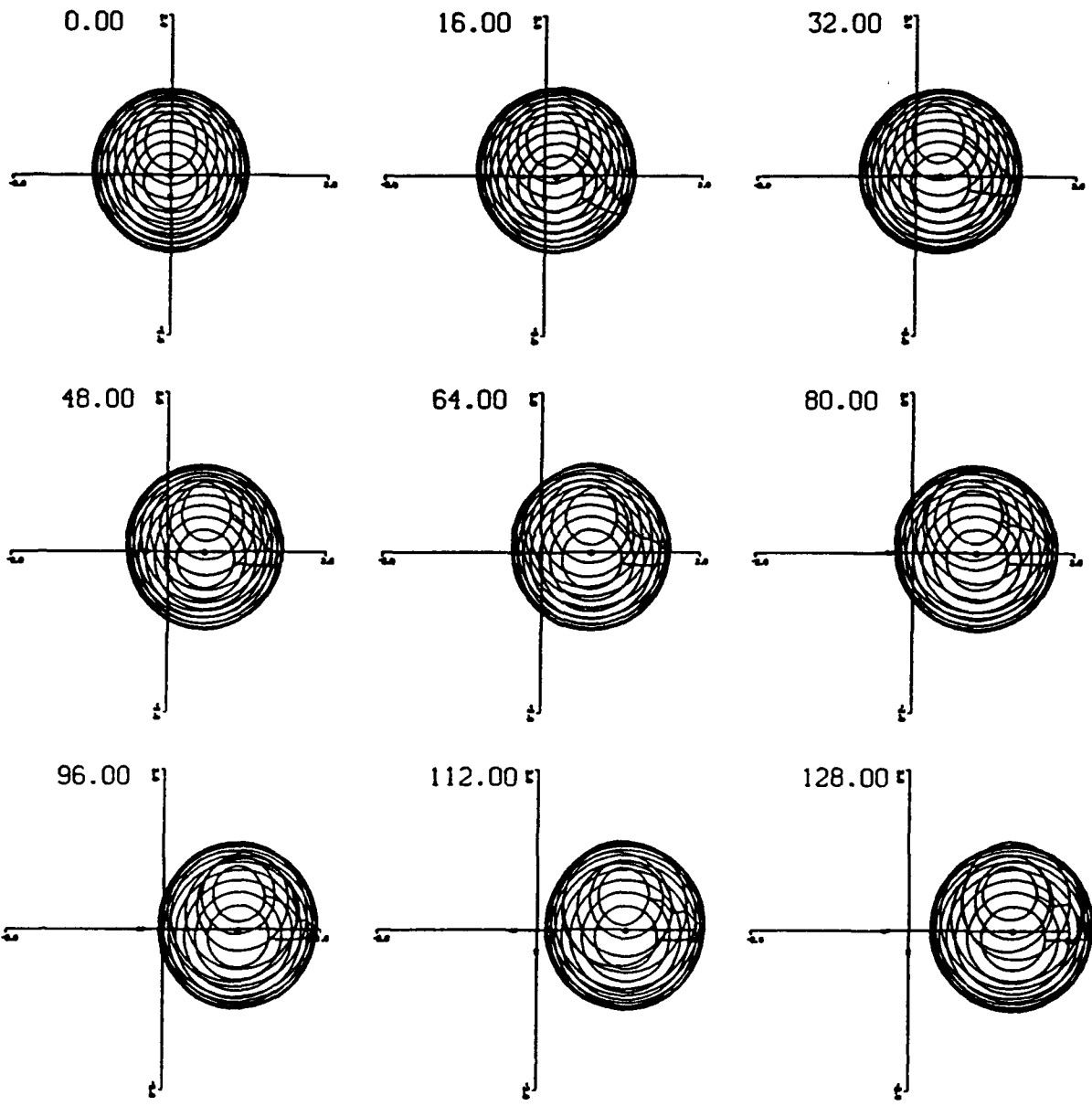
j: $\alpha = 0.05, b = 1.00$



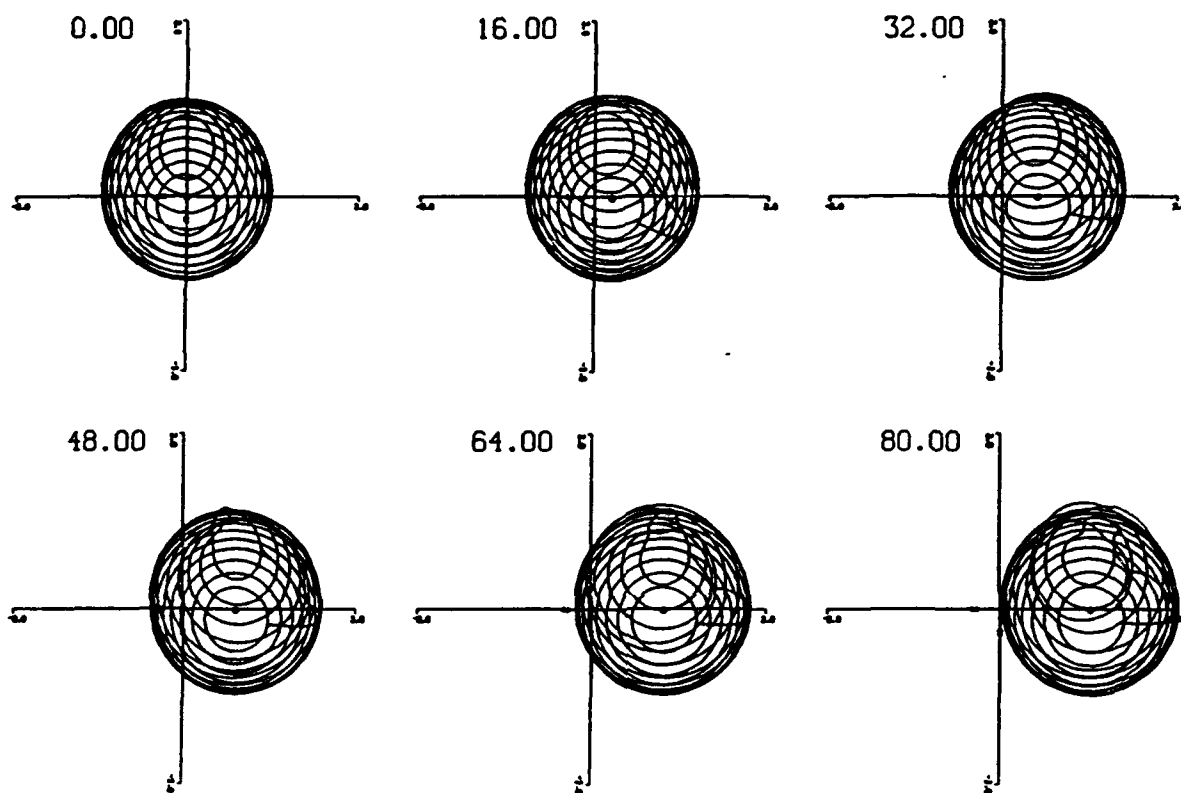
k: $\alpha = 0.06$, $b = 1.00$



1: $\alpha = 0.05$, $b = 1.25$



m: $\alpha = 0.03, b = 1.50$



n: $\alpha = 0.04$, $b = 1.50$

mode of behavior, or (b) been irreversibly distorted by the background flow. Most of the integrations were carried to $t = 128$, which is approximately $6\frac{1}{2}$ rotation periods for the monopolar vortex solution (recall from Chapter 3 that the rotation period for a fluid parcel in the core of a monopole is $6\pi \approx 19$).

Figure 4.12a shows a run in which a steady monopole in a shear given by $\alpha = .10$ is weakly perturbed ($\alpha \rightarrow 0.102$). Notice that the perturbed vortex wobbles slightly around its equilibrium shape, but no qualitative changes in shape are seen. However, the situation is qualitatively different in Figure 4.12b, in which the initial condition is a steady monopole in a slightly larger external shear $\alpha = 0.12$. When the solution is perturbed by increasing α to 0.122, the vortex is rapidly and apparently irreversibly stretched out by the external flow. This behavior is like that of the point vortex solutions. Recall from Chapter 2 that steady solutions in vertical shear became unstable if the shear (and hence the tilt) was too large. This was explained by noting that if the tilt of the pair is relatively small, then separating the vortices slightly leads to a stronger interaction (*i.e.*, a larger mutually induced relative velocity) between them. On the other hand, strongly tilted pairs interact less strongly when separated slightly, and are therefore less able to withstand external perturbations. Apparently the mechanism at work in Figure 4.12b is similar, as there appears to be a well defined maximum tilt beyond which any further tilt causes the vortex to be infinitely elongated.

The remainder of the runs shown in Figure 4.12 represent integrations from initial conditions with various values of α and b . The location of the initial conditions in (α, b) phase space is chosen close to the solvability limit shown Figure 4.8. When the baroclinicity is small, the unstable vortex is elongated at both ends simultaneously, as shown in Figure 4.12b,c. For larger b , the elongation of the core is increasingly confined to the bottom, where flow speeds are small, although the character of the elongation appears to be similar. Figure 4.12h shows a run in which the steady anticyclone characterized by $b = 0.75$, $\alpha = 0.060$ is subjected to a slightly larger shear $\alpha = 0.062$. Notice that the perturbed solution exhibits a periodic modulation while translating to the right, but its

character is still accurately described by the steady state solution in the sense that the average shape looks very much like the basic state solution. In this case the increased shear causes the vortex to rotate slightly in a counterclockwise direction, leading to further elongation by the external flow. However, this elongation stops when the vortex rotates back to the right, and is 'recompressed' by the external flow. The perturbed solution appears to have settled into a periodic mode of behavior, and is therefore stable. Closer to the solvability boundary, fluid from within the core can be pulled away by the external flow. In Figure 4.12i, a run is shown in which the steady solution for which $b = 0.75$ and $\alpha = 0.070$ is subjected to an external shear of $\alpha = 0.072$. Notice that the vortex again translates to the right, as linear theory predicts, but at $t \approx 96$ the boundary perturbation becomes very steep near the bottom of the lens, as some core fluid is torn off by the external flow. Soon after this the integration is stopped due to lack of resolution. In reality, the lens would presumably lose a certain amount of core fluid before settling into a new (probably unsteady) equilibrium. The form of the extrusions is similar to that found by Beckmann *et al.*, (1989) in a 9 layer QG simulation of Meddy movement on a β -plane. They found that as the Meddy drifted extrusions of core fluid were periodically lost to the surrounding waters. Notice that the solution in 4.12h exhibited a periodic nutation. For stable solutions the angular extent of the nutation is determined by the size of the perturbation (relative to the deformation of the boundary in the initial steady state) - the larger the perturbation, the larger the wobble. Whether fluid is pulled away from the core apparently depends upon the relative sizes of the nutation period of the perturbed vortex and the time scale for core deformation by the external flow. If the nutation period is small, then the lens will complete a nutation cycle (being elongated and then recompressed) before it can be irreversibly deformed by the external flow. In the remainder of the runs shown, the baroclinicity is progressively increased. The behavior of the solutions is similar to that described above, with solutions well within the solvability region being stable, and those close to the boundary being unstable. For large b the breakdown of the solutions appears to be similar to that for small b ,

with extrusions of fluid being lost from the core. However, as a result of the increasing up/down asymmetry of the basic flow for increasing b , the loss of core fluid is increasingly confined to the bottom of the lens. From these runs, the location of the linear stability limit in (α, b) space has been inferred, and it is shown by the sloping dashed line in Figure 4.8. This stability limit is clearly shifted with respect to the solvability limit discussed earlier. However, the sizeable region of (α, b) space in which the solutions are found to be stable indicates that the solutions are in general quite robust.

The behavior of the continuous model is similar in many respects to that of the point vortex model discussed in Chapter 2. There are, however, some important differences. Both models give translating solutions with trapped fluid cores, and both seem to be capable of qualitatively representing the low mode behavior of a baroclinic eddy in shear. Because the point vortex model represents only the lowest few modes of the continuous model, it cannot model high mode number phenomena *i.e.*, those with small vertical scales), such as the steering level phenomenon or the formation of cusps. These effects are responsible for the limiting b ($|b| \leq 5/3$) that was found, and for the slope of the α -solvability limit in Figure 4.8. It follows that there is no limit to the asymmetry of a point vortex pair (as measured by Δ), and neither the solvability nor the stability of the solutions depends upon Δ . Another important difference is that for a given value of the external shear there are in general two possible steady configurations, while the continuous model apparently admits only one. This difference is not very surprising, since the point vortex representation of a continuous potential vorticity field is only *strictly* valid when the continuous field is comprised of two widely separated blobs – a situation not considered here. Despite the various problems associated with the use of a point vortex representation of a continuous potential vorticity field, it nevertheless seems to give a good qualitative representation of many of the important aspects of the behavior of the continuous model.

Summary

The properties of finite amplitude steady vortex solutions have been discussed. The qualitative character of the solutions agrees well with that of the linear solutions discussed in Chapter 3 over much of the parameter space. In particular, the propagation speeds are in good agreement with the linear values. It was shown that this is because the linear propagation speed is in fact a fully nonlinear result. In addition, the shape of the deformed boundary is qualitatively well described by the linear solutions. The solvability limit associated with the baroclinicity of the flow in the core appears to be the same in the linear and nonlinear cases. In contrast to the linear solutions, the numerical solutions predict the maximum vertical shear α for which solutions can be found. This critical shear decreases as the baroclinicity b of the solutions increases. For small shears, the solutions are stable, since introducing a small perturbation leads only to a periodic modulation of the steady solution. At larger shears, the solutions are unstable to small perturbations, as perturbed vortices are rapidly and irreversibly stretched out by the external flow. The stability boundary is fairly close to the solvability limits shown in Figure 4.8, so the solutions are stable with respect to small perturbations unless they are quite close to the solvability boundary.

Chapter 5

Float Analysis

This chapter presents new results obtained from a recent SOFAR float experiment which show a Mediterranean Salt Lens being deformed by external flows. In addition, the propagation of the lenses through the surrounding waters (Richardson *et al.*, 1989) is related to the external shear and the potential vorticity structure inside the core using the analytical results discussed in Chapter 3. The data are taken from the SOFAR Float Mediterranean Outflow Experiment (Price *et al.*, 1986; Zemanovic *et al.*, 1988) in which Mediterranean Salt Lenses (Meddies) were seeded with floats and the first continuous record of the life history of a Meddy was obtained. Three different Meddies were seeded: one with with five floats, another with two, a third with a single float. Many more floats were deployed in the surrounding waters. Figure 5.1 shows the trajectories of three of the Meddy floats as they move with the Meddies. The data contain information pertaining to the structure of the flow within the Meddy core and on the motion of Meddies with respect to the surrounding water. Richardson *et al.* found that Meddies moved at $1.4 \pm 0.3 \text{ cm s}^{-1}$ relative to floats at similar depths outside of Meddies. In the present analysis, a tilting of the rotation axis of the Meddy has been observed, which is presumably due to the influence of external shear. In what follows, we shall interpret these observations using the model discussed in Chapter 3.

Our analysis focuses on Meddies 1 and 2, as each of these contained at least two SOFAR floats at different depths, which is necessary to resolve the vertical structure of the core deformation. Meddy 2 contained two floats, which were separated by roughly 100 m in the vertical. Meddy 1 contained a total of five floats, but the pressure sensors on several of the floats did not function properly, so their depths are not well known. In some cases, however, it was possible to infer the depth of the float from the temperature record, using the temperature structure for this Meddy found by Hebert (1988). Using this procedure, we deduced that float EB150 was at approximately 1220 db, about 120 m beneath EB128, which was at 1100 db. The three remaining floats in the this Meddy:

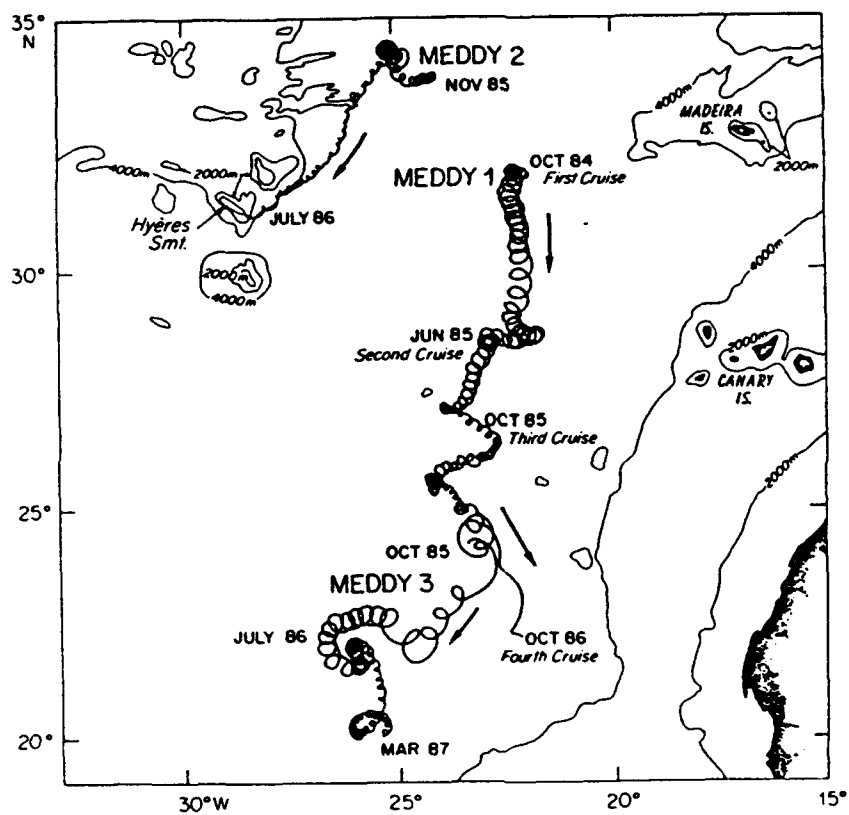
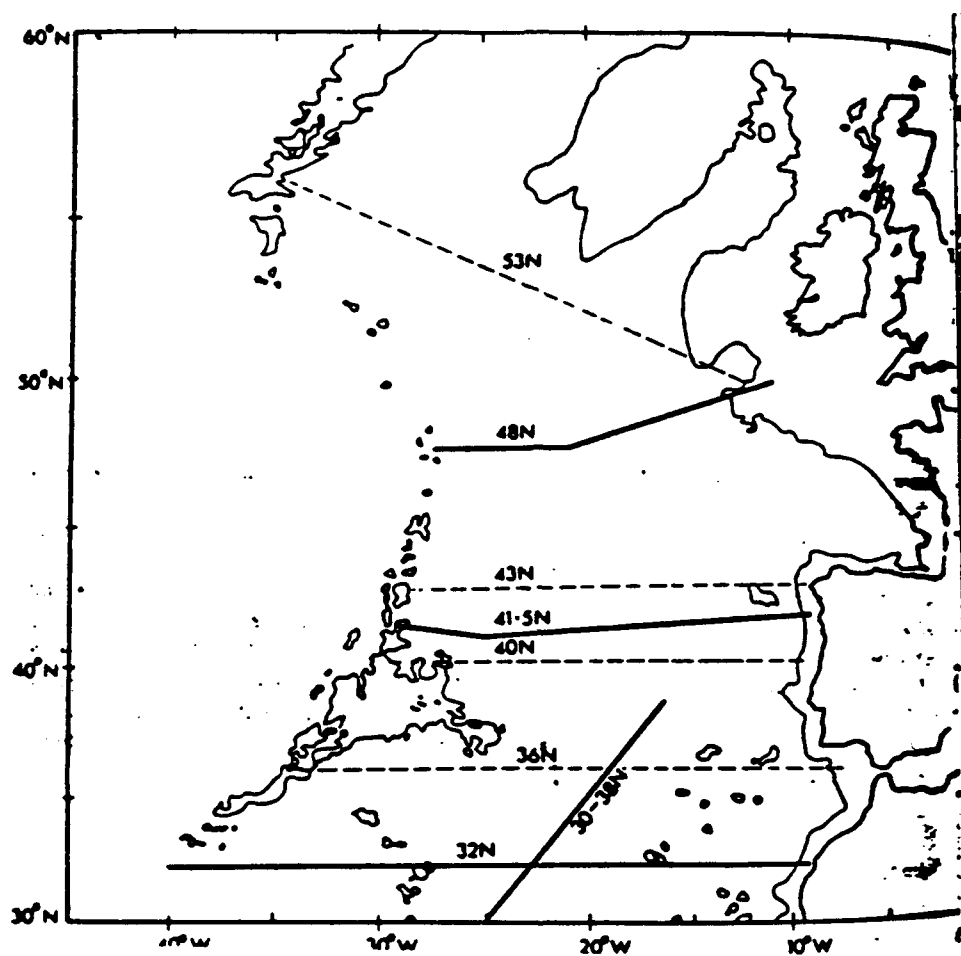


Figure 5.1: Trajectories of three SOFAR floats in three different Meddies (from Richardson *et al.*, 1989). Two floats were deployed in Meddy 1, five in Meddy 2, and one in Meddy 3.

EB140, EB141, and EB143, were all near the 1100 db level, and were therefore not used in the analysis. The float data show that the flow within the core of a Meddy is strong, with typical azimuthal velocities of some 20 cm s^{-1} at a distance of 20 km from the center. By core we refer to the region of warm and salty water in which swirl velocities are found to increase linearly with distance from the rotation axis, rather than to the entire region of trapped fluid which moves with the Meddy. Although the flow within the core is approximately in solid body rotation over certain depth ranges, the trajectory of float EB145 shows that the rotation frequency may be still be a strong function of depth within the core. The looping period of this float decreased from approximately 23 days to just 12 days as the float rose from 1300 db to 1050 db within the core. This acceleration happened over a rather narrow depth range (about 40 db), suggesting an almost discontinuous change of rotation frequency with depth. It should be emphasized that the float temperature stayed fairly constant at about 7.5°C while the float rose by 250 db, implying that the float was indeed in the core of the Meddy all the while. Rotation rates in Meddy 1 also varied significantly with depth: float EB128 looped with a six day period at the 1100 db level, while EB150 looped with a period of 16 days at 1220 db. In this case, however, a comparison with Hebert's data indicates that EB145 was probably slightly beneath the Meddy core. Thus, the different rotation rates measured for this Meddy are probably not due to the baroclinicity of the core alone.

The structure of the mean flow field in the Canary Basin is not well known. Perhaps the most detailed information can be found in the study by Saunders (1981), who computed geostrophic velocity profiles from several sections in the eastern North Atlantic (Figure 5.2). The two southernmost sections (one at 32N and another extending from 30N/25W to 38N/17W) show that the flow is generally southward with larger velocities near the surface. The 32N section shows a variation in the flow speed of about 0.3 cm s^{-1} between 1500 db and 500 db, while the second section shows a much larger variation of about 2 cm s^{-1} over the same range of pressures. Finally, it is interesting to notice that at 32N there is virtually no meridional flow at 1000 db, near the core of the Salt Tongue



5.2a: Section Locations

Figure 5.2: Geostrophic velocity profiles along several sections in the eastern North Atlantic (from Saunders, 1981). The southernmost two sections show the vertical profile of the large scale flow in the study region. A significant vertical shear is present in the study region, which amounts to a variation in flow speed of about 2 cm s^{-1} over the depth of a Meddy core.

(Saunders, 1981), which is consistent with the observation that the mean velocity from nearby floats outside Meddies was quite low.

Data Analysis

To investigate the tilt of the rotation axis of the Meddies, it was necessary to calculate the center of rotation from float trajectories at different depths inside the core. A low pass filter was used to remove the looping component from the float trajectories, and to give an estimate of the position of the lens center as a function of time. This technique worked quite well in general, because of the large spectral gap between the looping motions of the floats and the motions of the lens as a whole. However, the technique failed when the trajectory of the lens turned sharply, or when the looping frequency of the float changed suddenly. In such cases the trajectory was split into two or more sections, and the different sections processed independently. In the present analysis only well behaved sections of the trajectories were used. Due to the different looping frequencies of the floats, it was nevertheless necessary to use several different filters in the analysis. For float EB150 a 61 day moving average filter having Gaussian filter weights with a standard deviation of 11 days was used, providing a frequency response of 0.5 at a frequency of about $\frac{1}{65}$ cycles/day, with higher frequencies being more strongly attenuated. For EB128 a 31 day filter with a standard deviation of 5.7 days was used, giving a frequency response of 0.5 at $\frac{1}{28}$ cycles/day. For floats EB148 and EB149 a filter with a standard deviation of 4.0 days was used, giving a frequency response of 0.5 at $\frac{1}{20}$ cycles/day.

An alternative (and somewhat less direct) way to accomplish the same thing is to divide the time series of positions into a number of shorter sections, fitting each section to a simple model of the form

$$\begin{aligned}x_n(t) &= x_{n0} + U_n t + R_n \cos(\omega_n t + \phi_n) \\y_n(t) &= y_{n0} + V_n t + R_n \sin(\omega_n t + \phi_n),\end{aligned}\tag{5.1}$$

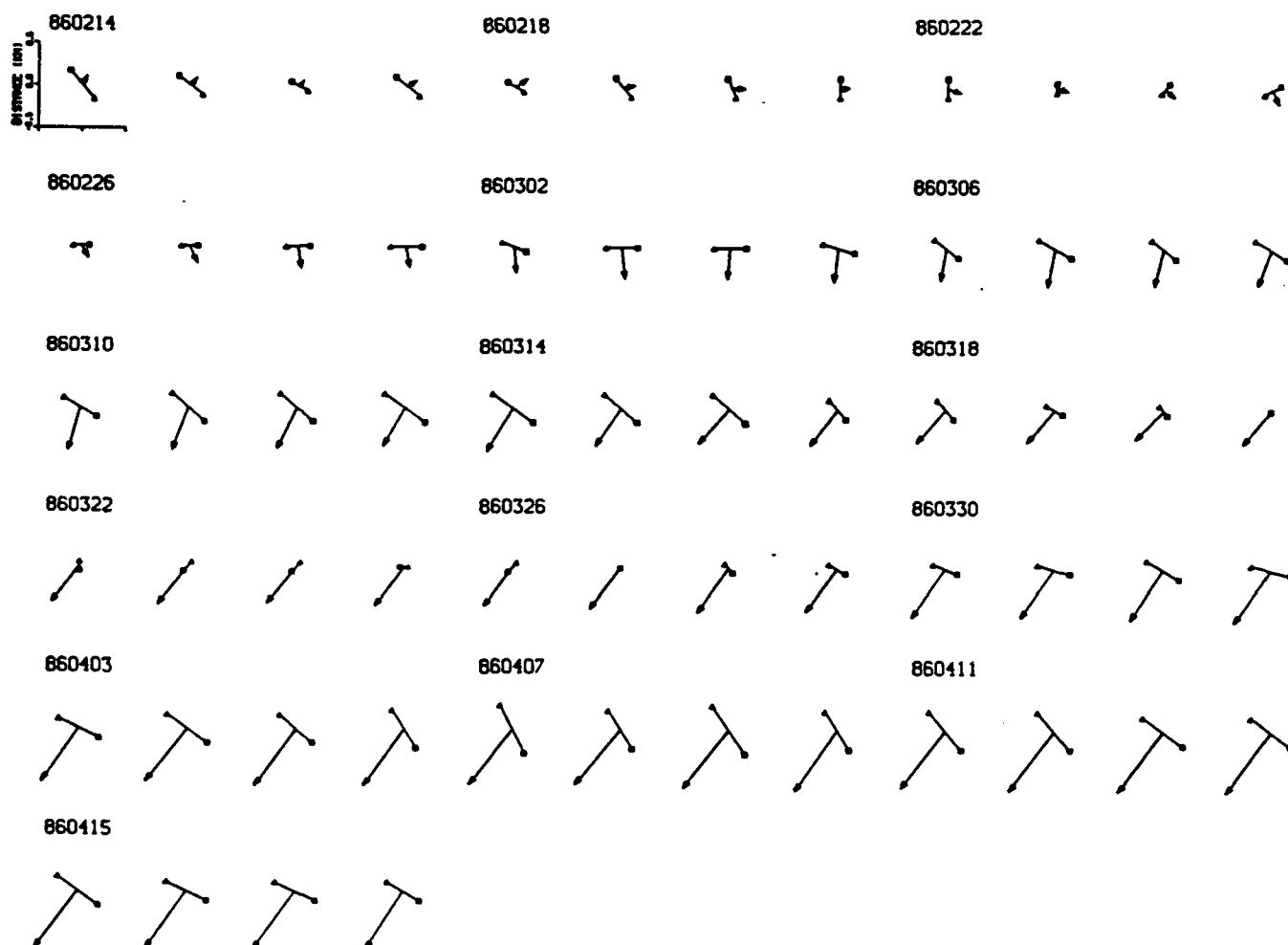
where the subscript n refers to the n^{th} section. Thus, each section of a trajectory was decomposed into a linear drift plus a circular looping component. The model parameters were fitted using standard nonlinear least-squares algorithms found in *Numerical Recipes* (Press *et al.*, 1986), which gave satisfactory results when the initial guesses were reasonably good. This technique seemed to give results inferior to those of the low pass filtering technique ¹, so we have used the filtering technique exclusively.

Careful examination of the results shows a systematic lateral shift between filtered trajectories from floats at different depths. To illustrate this, daily realizations of the configuration of Meddy 2 were plotted for the period from 14 February 1986 through 18 April 1986 (see Figure 5.3a). This section of the trajectory was chosen because it is fairly well behaved, with no sharp corners, so that the filtering method should work quite well. The most notable aspect of the plot is the apparent tendency of the Meddy rotation axis to 'tilt' in a direction perpendicular to the drift direction of the Meddy, with maximum displacements of almost a kilometer in late June 1986. Notice that the top of the lens is shifted to the right with respect to the drift direction of the Meddy. The core was in this tilted configuration for all but one of the nine weeks shown. Figure 5.3b shows a similar plot for Meddy 1, using the trajectories from floats EB128 and EB150 for the period from 23 January, 1986 through 11 March, 1986. The general pattern is the same, with displacements normal to the drift direction of the Meddy, and the top of the lens deflected to the right. In this case the observed displacements were *much* larger than those seen in Meddy 2, sometimes exceeding 10 km.

The large observed displacements are probably a result of float EB150 being in the region of trapped fluid beneath the actual core, which may become very distorted as the Meddy moves. It is also possible that the large tilt is due in part to the fact that the Lagrangian center of an eddy is displaced from the Eulerian center if the eddy is in motion (Flierl, 1979). If the rotation frequency is the same at the depths of the two

¹This is probably due to the fact that the parameters U_n and V_n are *derivatives* of the original position time series, which would tend to amplify any errors in the calculation.

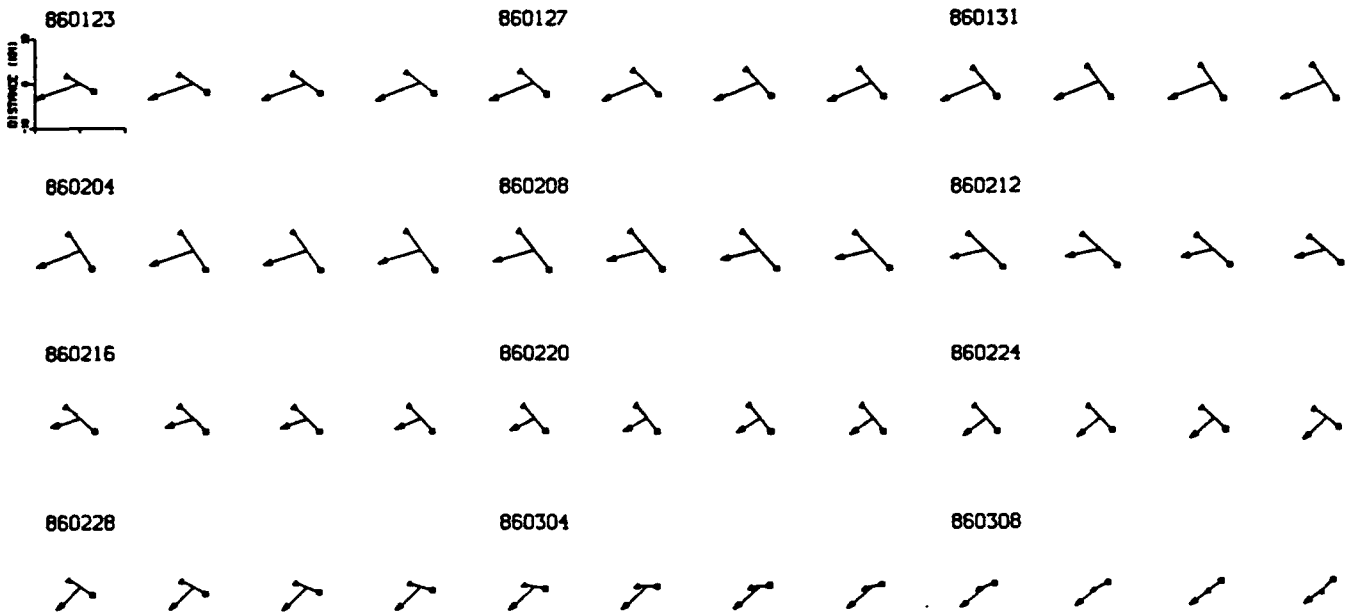
Meddy 2



5.3a

Figure 5.3: Daily realizations of Meddy drift velocity, represented by arrows, and 'tilt', shown by a line connecting the centers of rotation at different depths. Figure 5.3a shows Meddy 2 during the period from 14 February, 1986 through 18 March, 1986. The triangle in Figure 3a represents the position of the lens center given by float EB149, at an average pressure of about 1050 db, while the square gives the position of the lens center computed from float EB148, at an average pressure of 1160 db. The drift velocity of the Meddy is scaled such that the longest arrow represents a velocity of about 4 cm s^{-1} . Figure 5.3b shows the data from Meddy 1 between 23 January, 1986 and 11 March, 1986. The triangle represents the center at the 1100 db level, while the square gives the center at about 1220 db. In this case the longest arrow represents a velocity of about 3 cm s^{-1} . Notice that in each case the Meddy has a tendency to tilt in a direction perpendicular to its drift direction.

Meddy 1



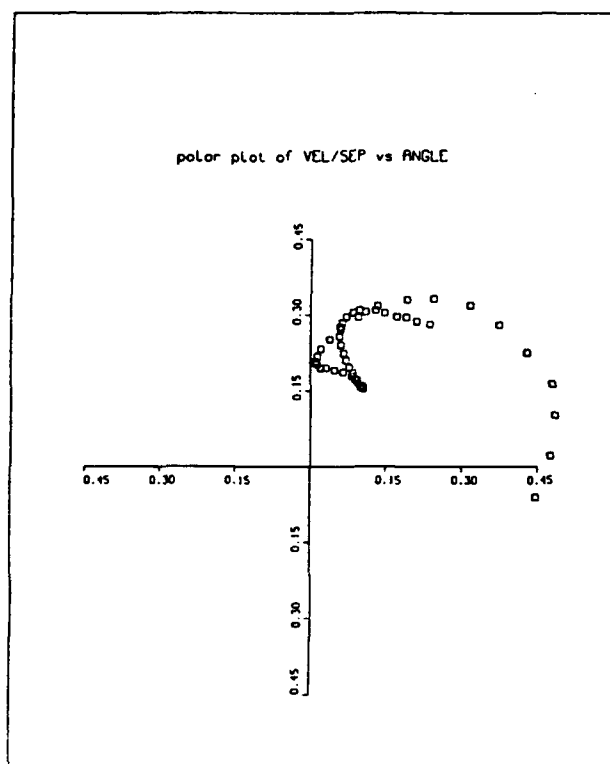
5.3b

floats, then the displacement of the centers will not vary with depth, and there will be no 'Lagrangian tilt'. This is the case for Meddy 2, for which the rotation frequency of the two floats was almost identical. For Meddy 1, however, the situation is different, as the rotation frequency of the upper float is almost three times that of the lower float. If the Meddy moves at roughly 1 cm s^{-1} , and the rotation frequencies of the two floats are 1 cycle/6 days and 1 cycle/16 days, respectively, a simple calculation shows that the Lagrangian tilting effect leads to a displacement between the centers at the two depths of about 1.4 km. Since the observed displacements are much larger than this, they must be primarily due to some other effect. It seems more likely that they can be explained by float EB150 being in the region of trapped fluid beneath the core of the Meddy.

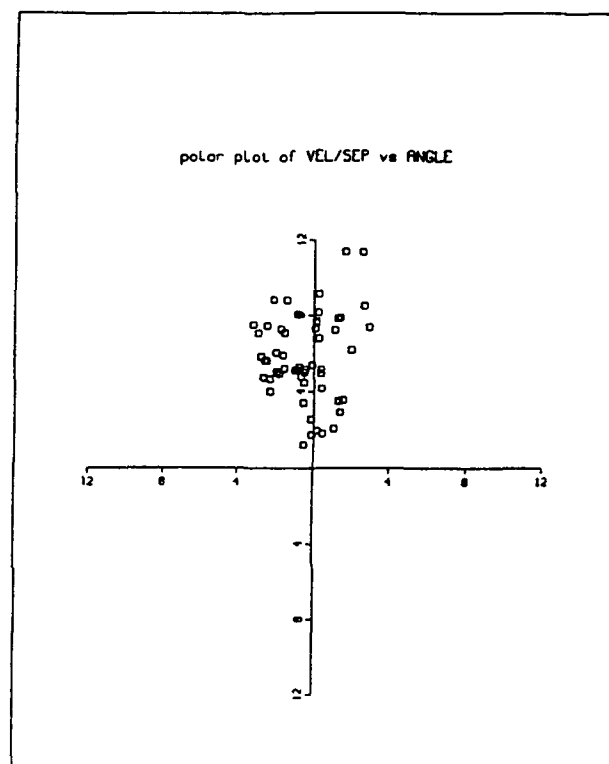
Looking once again at Figure 5.3, we see that there are periods of time in which the lens is clearly *not* in the tilted configuration discussed above. In particular, during the period from 19 May through 29 May Meddy 2 appears to 'wobble' briefly, before returning to the tilted configuration. It is reasonable to interpret this behavior in terms of the natural precession tendency of the deformed lens, as discussed in Chapter 3. This sort of behavior could, for example, be caused by a variation of the shear outside the lens. The 'wobbling' in Figure 5.3a is consistent with a weakening of the external shear. The decreased external shear would lead to an anticyclonic precession of the lens, which would in turn result in a gradual 'recompression' of the lens by the external flow. Continuing to precess beyond this point, the lens might eventually approach a new equilibrium similar to the first. Unfortunately, the variations in the external shear are completely unknown, and the resolution of the data limited, so this interpretation is necessarily speculative.

Figure 5.4 gives a statistical summary of the information in Figure 5.3. Each of the squares in 5.4a marks the tip of a vector, the length of which measures the ratio of the drift speed of the Meddy to the horizontal displacement of the rotation axis. Thus, if the propagation speed were proportional to the deflection of the rotation axis, the vectors would all have the same length. The inclination angle Θ is the angle between the displacement vector and the velocity vector. Notice how the points tend to cluster along

Meddy 1



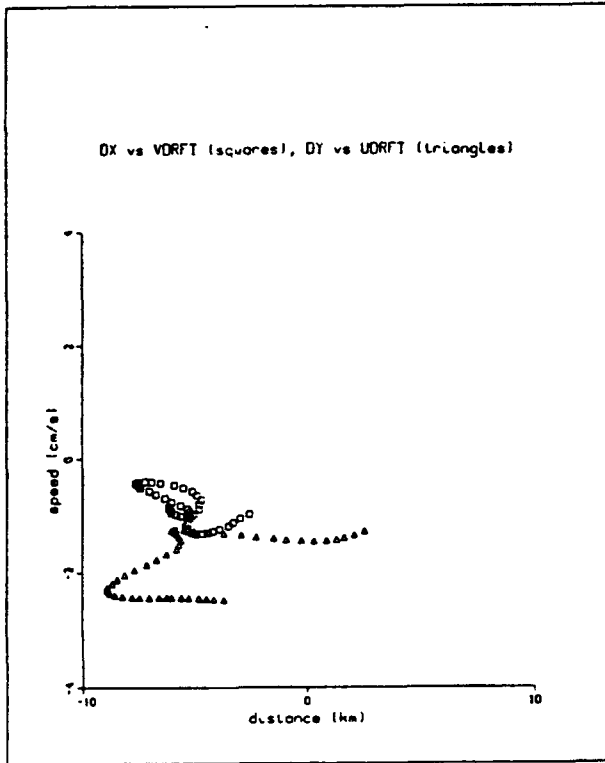
Meddy 2



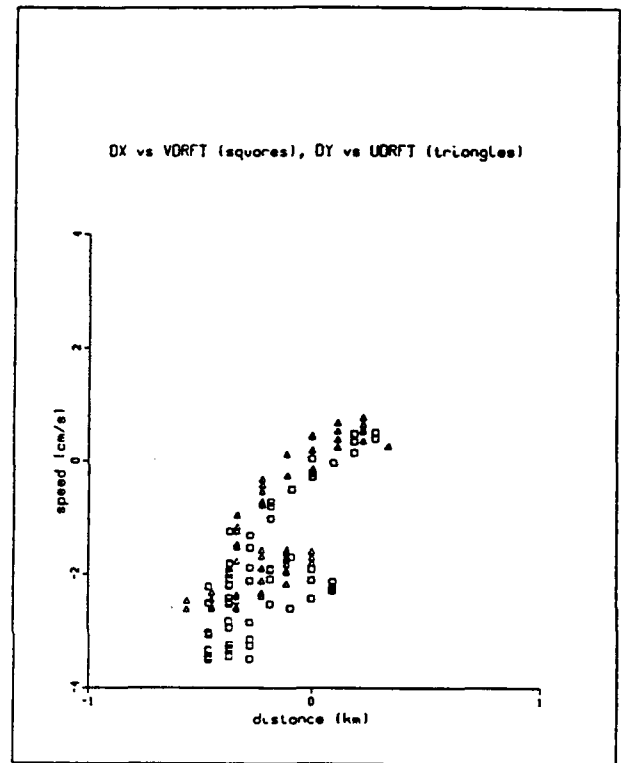
5.4a

Figure 5.4: Statistical summary of Meddy velocity and tilt data from Figure 5.3. Each of the daily realizations in Figure 4 is represented by a vector of length ℓ and angle Θ , where ℓ is the ratio of the drift speed to the horizontal displacement of the rotation axis. The squares represent the tips of these vectors. In 5.4b the x separation of the rotation axis is plotted against the v velocity component (squares), and the *negative* of the y separation *vs* the u velocity component (triangles), showing the apparent correlation between the deflection of the rotation axis and the speed of the lens.

Meddy 1



Meddy 2



5.4b

the vertical axis, illustrating the tendency for the rotation axis to be deflected at right angles to the drift direction of the lens. Plotting the data in a slightly different way shows an apparent relationship between the deflection of the rotation axis and the translation speed of a Meddy. In 5.4b the x separation of the centers of rotation is plotted *vs* the v velocity of the lens, and the *negative* of the y displacement *vs* the zonal velocity of the lens. Plotted in this way, a straight line through the origin would represent the case in which the propagation speed is proportional to the tilt. This shows quite clearly that for Meddy 2, large displacements of the rotation axis are associated with rapid translation. For Meddy 1 the relationship between the propagation speed and the tilt of the axis is not so clear. We speculate that (as noted before) this is due to the fact that EB150 was not in the core of the Meddy.

Comparison with the Model Results

The behavior illustrated in Figures 5.3 and 5.4 may be usefully interpreted in terms of the simple model discussed in Chapter 3. As a consequence of the idealized nature of the model, detailed agreement with observation should not be expected. For example, the modeling results assume that the Burger number S has a value of one, while observations seem to indicate that $S \approx 0.23$ is more realistic. Our hope is simply to convince the reader that the dynamics inherent in the model solutions may play a significant role in the behavior of Mediterranean Salt Lenses. In Chapter 3 it was shown that when external shear is present, steady states are possible in which the tendency of the boundary disturbance to precess is counterbalanced by the advection due to the external shear. Figure 3.5a illustrates one such steady configuration, in which the eddy is tilted in a transverse sense by a vertically sheared background flow. The results discussed in Chapter 3 show that the magnitude of the 'tilt' for such a configuration is directly proportional to the strength of the external vertical shear. It was shown that the amplitude of the boundary perturbation for the model vortex in an external vertical

shear given by $u_{b*} = \alpha_* z_*$ is

$$|\eta_{f*}| = \frac{5}{4} \frac{\alpha_* D}{U_{max}} R, \quad (5.2)$$

where an asterix denotes a dimensional quantity. Here D is the half-depth of the lens, R is its radius, U_{max} is the the maximum swirl speed inside the lens, α_* is the vertical shear of the external flow, and $|\eta_{f*}|$ is the amplitude of the boundary deformation caused by the external flow. If we let $D = 500$ m, $R = 25$ km, $U_{max} = 20$ cm s⁻¹, and $\alpha_* = 2 \times 10^{-5}$ s⁻¹, giving a variation in the external flow speed of 2 cm s⁻¹ over the core depth, it follows that

$$|\eta_{f*}| \approx 1.6 \text{ km}. \quad (5.3)$$

This is in good agreement with the results shown in Figure 5.3a, if we assume that the displacement of the rotation axis is comparable with the size of the boundary deformation. However, because the floats are quite closely spaced in the vertical (≈ 100 m), it is likely that the full extent of the tilting is not seen. The displacements observed for Meddy 1 are significantly larger than this, perhaps indicating very large external shears, or else that the float is not in the core at all, but is instead in the region of trapped fluid outside the core. Based on the earlier discussion of the depth of this float, we believe that it was in fact located slightly beneath the Meddy core.

In Chapter 3 it was demonstrated that the propagation speed of a lens-like f plane quasigeostrophic vortex in a stratified fluid in a flow with constant vertical and horizontal shear *relative to the external fluid* is given by

$$u_{0*} = \frac{1}{5} \alpha_* D \frac{b_* D}{a_*}. \quad (5.4)$$

The parameters a_* and b_* describe the potential vorticity within the core of the model vortex: $q_{0*} = a_* + b_* z_*$. If $b_* = 0$ the potential vorticity within the core is constant, and the core region will be in pure solid body rotation. If b_* is nonzero, the rotation frequency will vary with depth in the core. This flow is consistent with that reported by Richardson *et al.* (1989) for a real Meddy. Thus, the model predicts that the translation speed is completely determined by the form of the potential vorticity field within the lens and

the magnitude of the external vertical shear. For a Meddy such as Meddy 3, reasonable estimates of the baroclinicity give $\frac{b_* D}{\alpha_*} \approx 1$, implying that depth variations of the core potential vorticity are comparable with the absolute values. Estimates for Meddy 1 give about the same value. Within the context of the model discussed in Chapter 3, $\frac{b_* D}{\alpha_*} \approx 1$ implies that the rotation rate varies by a factor of four over the core depth. It should be emphasized that this estimate is very approximate, as the floats typically undersample in the vertical (they are designed to remain at a fixed pressure level). The only thing that can be said with certainty is that the flow within the core of a Meddy may be quite baroclinic, and therefore it is not unreasonable to assume that the flow within the core of Meddy 2 was also significantly baroclinic. We will therefore assume in our analysis that both Meddies 1 and 2 have order one baroclinicity. Choosing $D = 500$ m and $\alpha_* = 2 \times 10^{-5} \text{ s}^{-1}$ (implying that the flow speed varies by 2 cm s^{-1} over the core), it follows that the predicted translation speed is 0.2 cm s^{-1} . Finally, it was shown in Chapter 3 that no solutions could be found for a lens with radius $R = ND/f_0$ for which $\frac{b_* D}{\alpha_*} \geq \frac{5}{3}$, from which it follows that the *maximum* attainable propagation speed is

$$u_{0,MAX} = \frac{1}{3} \alpha_* D . \quad (5.5)$$

For the previous parameter values, this takes the value

$$u_{0,MAX} \approx 0.33 \text{ cm s}^{-1} , \quad (5.6)$$

which is significantly smaller than the value of $1.4 \pm 0.3 \text{ cm s}^{-1}$ found by Richardson *et al.*. It is possible that this discrepancy is due to an underestimate of the external shear strength. Alternatively, it is possible that it can be attributed to the fixed horizontal scale that was used in the calculation. Recall that it was assumed that the radius of the lens was given by $R = ND/f_0$, while ocean data indicate that the radius of the lens may be closer to $2ND/f_0$. How can this make a difference? In the context of the present model, it is the differential circulation over the depth of the core, which (in conjunction with the external shear) causes the eddy to propagate. The differential circulation component is

bounded by the requirement that the circulation in the core be of the same sign at all depths (recall that there were no solutions for which the circulation changed sign over the depth of the core). As the horizontal dimension of the lens is increased, the circulation increases, allowing for the possibility of larger differential rotation rates, and hence larger propagation speeds. In the context of the present model, this implies that the estimated value of b may be a function of the lens dimension, and preliminary calculations show that larger lenses require significantly larger values of b to achieve the same variation in rotation rate. Finally, it seems fairly certain that β plays some role in Meddy movement. Using a nine layer QG β -plane model, Beckmann *et al.*, (1989) found that a model Meddy drifted nonuniformly to the southwest at about 0.8 cm s^{-1} , as a result of the mechanism first described by Bretherton & Karweit (1975). More recently, Colin de Verdiere (in press) has suggested a dynamical balance between the slow vertical erosion of the core of the Meddy by small scale mixing processes and meridional translation on the β -plane. It is possible that one or both of these mechanisms plays a role in producing the observed translation. However, we feel that much of the discrepancy between the predicted and observed speeds can be attributed to the fixed horizontal scale of the model vortex.

It is hypothesized that Meddies 1 and 2 are, on average, in configurations qualitatively like the steady configuration just described for much of the duration of Figure 5.3. There is, of course, no obvious reason why the system should seek out such a steady configuration, and one can easily envisage a situation in which the solution is periodic in the external shear. In such a case, the boundary perturbation may be considered to have two components, one of which is in a steady equilibrium with the external shear, the forced component, and an homogeneous component, which precesses freely. This would lead to a periodic modulation of the vortex boundary, with a period given by the precession period of the homogeneous mode. It is quite likely that any freely precessing component of the response is at least partially filtered out in our analysis, causing the response to look more steady than it actually is. The apparent tilting of the lens is consistent with a vertically sheared external flow which is approximately parallel to the direction of drift

of the Meddy, and which becomes more intense with decreasing depth. The drift velocity vectors in Figure 5.3 apparently represent some average of the external velocity field over the Meddy core – not (directly) the vertical shear of the external flow. However, it is reasonable to suppose that the *direction* of the external shear is well represented by these vectors, if not its magnitude. The periods during which the Meddy is not in a transverse configuration may correspond to events in which the magnitude or the direction of the external shear changes, so that a steady balance cannot be maintained.

Possible Sources of Error

Given the small horizontal shifts of the rotation axis indicated in Figure 5.3a, it is natural to question the accuracy of the computed positions. This is a rather complex issue, as there are a number of random and systematic errors which could contaminate the position data. The accuracy of the absolute position fixes will typically depend upon where the float is located with respect to the array of moored listening stations tracking it, on how well the listening stations are localized, on how accurately the mean sound speed between source and receiver is known, and also upon how well the float and listening station clock drifts which occur over the duration of the experiment can be determined and corrected for. Further inaccuracies may be introduced by unknown mooring motions, and also by sound speed fluctuations that occur between the float and the listening stations. Finally, small systematic errors may be introduced when different arrays of listening stations are used to track different floats. Therefore, in the present analysis, all floats within a given Meddy have been tracked using the same listening stations. We have reviewed the processing of the data, and believe that the listening stations are well situated to track the floats, that the clock drift corrections are quite clean, and that the position fixes for these floats should therefore be quite good. It is estimated (P. Richardson, *personal communication*) that with a good tracking configuration, as we have here, the *absolute* position of a float can be determined with an accuracy of at best a few kilometers. However, the accuracy in determining the *displacement* between two *nearby* floats will be significantly better than this, as most of

the errors mentioned above will tend to cancel. For example, any error in the position of a listening station should affect the computed positions of both floats in the same way, and the error should subtract out when displacements are computed. Similarly, the effect of large scale sound speed fluctuations between the Meddy and the listening stations will tend to cancel out when the displacements are calculated. Finally, the effect of random positioning errors on the float displacements is likely to be quite small, since each point in the filtered trajectory represents an average of many individual position fixes. A rather detailed analysis shows that for Meddy 2 this effect can be expected to give errors which are on the order of 0.2 km (Richardson, *personal communication*). This is significantly smaller than the displacements shown in Figure 5.3 for this Meddy, so it seems unlikely that random positioning errors could qualitatively change our results.

There is one systematic error which will not tend to cancel, and that is due to the different effective sound speeds for the two floats in the Meddy. This is a potentially serious problem if the floats are at very different radii within the core. In this case, averaged over time, the sound from the float nearer the center of the lens will travel through more of the warm water in the core, leading to a decreased net travel time. The travel time decrease will be erroneously interpreted as a lateral shift of one of the trajectories relative to the other, which could lead one to conclude that the core is tilted. This is illustrated in Figure 5.5 for the extreme case in which one float is exactly in the center and the other is at the extreme edge of the Meddy core. At point p_1 , the sound from float B must travel through the full diameter of the lens to reach the listening stations, while at points p_2 , p_3 , and p_4 the sound misses the warm core water entirely. On average, then, the sound from this float travels a distance of about $\frac{1}{2}R$ through the core, while that from the float A travels a distance R through the core. Thus, on average, the sound from the float A travels through $\frac{1}{2}R$ more of the core water than does that from the first float. The *maximum* travel time difference due to this effect is then

$$\Delta t \leq \frac{1}{2}R \left(\frac{1}{c_{\text{outside}}} - \frac{1}{c_{\text{inside}}} \right), \quad (5.7)$$

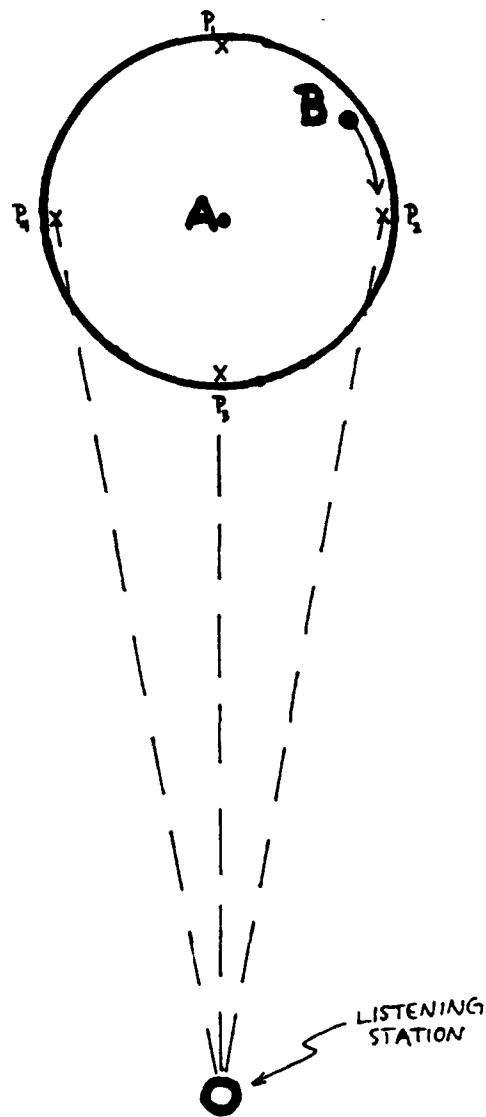


Figure 5.5: Mechanism by which mean float positions could be biased by sound speed differences if the floats are at different radii. On average, the sound from float A travels through more of the warm water in the core than does that from float B, as described in the text. As the sound speed is greater inside the Meddy core than in the surrounding water, this leads to a travel time difference, and an *apparent* shift in the average position of float A toward the listening station relative to float B. It is estimated that for a lens 25 km in diameter with a temperature of 12°C inside, 8°C outside, the maximum position error due to this effect is approximately 0.12 km (see text).

where R is the radius of the lens. The maximum deviation in the float position due to this effect is therefore

$$\Delta R \approx c \Delta t \leq \frac{1}{2} R \frac{c_{\text{inside}} - c_{\text{outside}}}{c} . \quad (5.8)$$

We shall assume that the temperature is 12°C inside the core, 8°C outside the core, that the salinity is 36 psu inside, 35 psu outside, and that the depth is 1100 m. With these assumptions, it follows that ²

$$c_{\text{inside}} \approx 1516 \text{ m s}^{-1} \quad (5.10)$$

$$c_{\text{outside}} \approx 1502 \text{ m s}^{-1} , \quad (5.11)$$

so the sound speed varies by about 0.9% due to the warmth and salinity of the core water. Substituting these values into the expression for ΔR , and assuming (as before) that the radius of the lens is 25 km, it follows that

$$\Delta R \leq 0.12 \text{ km} . \quad (5.12)$$

This is significantly smaller than the deviations shown in Figure 5.3, so we conclude that the apparent tilting cannot be due this effect alone. A similar error is possible when the two floats are at significantly different depths within the core. However, a 100 m depth difference produces a change in sound speed of only 1.6 m s^{-1} , so that the maximum possible error due to this effect is an order of magnitude smaller than the value of 0.12 km listed above, and it follows that the effect is negligible in this case.

In conclusion, the data show a low mode distortion of the Meddy cores which is evidently a consequence of the vertical shear of the external current. The size of the observed distortion of Meddy 2 is consistent with a variation in the external flow speed of about 2 cm s^{-1} over the depth of the core, according to the simple theoretical model discussed in Chapter 3. This external flow speed variation is in good qualitative

²The sound speed (in m s^{-1}) can be calculated using the standard formula

$$c = 1449.2 + 4.6T - 0.055T^2 + 0.00029T^3 + (1.34 - 0.010T)(S - 35) + 0.016 |z| , \quad (5.9)$$

where T is measured in degrees Centigrade, z in meters, and S in parts per thousand (Clay and Medwin, 1977, p.3)

agreement with the available data on the vertical structure of the flow within the Canary Basin. The tilt is much larger in the data from Meddy 1, with displacements of the rotation axis of the same order as the radius of the lens. This implies either that the external shears are quite large, or else that one of the floats is not in the core at all, but is instead in the region of trapped fluid outside the core. We favor the second explanation. The predicted movement of the model vortex through the surrounding waters is significantly smaller than that observed by Richardson *et al.* (1989). It is felt that this discrepancy may be largely due to the fixed horizontal scale of the model vortex.

Concluding Remarks

Recent observations of subsurface mesoscale lenses have provided an unprecedented glimpse of their behavior in the ocean. The importance of the various mesoscale and submesoscale lenses to the oceanic general circulation has not yet been fully assessed. However, one such lens, the Meddy, is known to transport large amounts of warm & salty Mediterranean water within the eastern North Atlantic. Meddies are thought to play an important role in maintaining the structure of the Mediterranean Salt Tongue – a prominent feature in the North Atlantic Circulation. The cores of these lenses are gradually eroded via intrusive / double-diffusive mixing processes, and thus they are a source of salt for the surrounding waters (*e.g.*, Ruddick and Hebert, 1988). Meddies are known to be embedded in a larger scale mean flow / eddy field, and we have tried to understand the influence of this larger scale flow on Meddy behavior. A pair of simple process models have been examined to investigate the role played by the external shear in determining the viability of such eddies, and to determine the role played by the external shear in producing the observed propagation of oceanic lenses. The availability of high quality Lagrangian float data has permitted a direct verification of certain of the model predictions. The float analysis has demonstrated that the rotation rates within the core may vary significantly with depth. Furthermore, the data show that Meddy cores may be deformed (presumably via interactions with external flows), and that this deformation is apparently related to the translation velocity of the lenses. These results of the float analysis were carefully checked to rule out the many possible errors.

While differing in their detailed predictions, the models which have been examined give predictions which are qualitatively in agreement with observations. The point vortex model discussed in Chapter 2 illustrated many aspects of the behavior of a mesoscale lens in shear (*e.g.*, a region of trapped fluid which is deformed by external flows, and which may translate through the surrounding waters), while in Chapter 3 it was shown that the simple dynamical mechanisms inherent in the point vortex model are readily generalized to more sophisticated models. These solutions were found to propagate in the presence

of external vertical shear, provided that the potential vorticity field associated with the lens had a baroclinic component. Furthermore, the solutions exhibited an average transverse tilt, which was shown to be consistent with the available float data. The numerical integrations described in Chapter 4 extended these linear, analytical results into the nonlinear regime, and demonstrated that the solutions are stable for moderate values of the external shear and core baroclinicity, and that therefore eddies of this sort can be expected to persist for long periods of time. Thus, oceanic lenses governed by these dynamics should last for long periods of time, which is in agreement with the long observed lifetimes of Mediterranean Salt Lenses. While the model solutions gave boundary deformations of the correct order (given the uncertainties concerning the external flow), the predicted translation speeds were significantly smaller than those observed by Richardson *et al.* (1989). This implies that other effects are important in producing the large translation speeds that have been observed. The neglect of β rules out mechanisms like that proposed by Colin de Verdiere (*in press*) and Bretherton and Karweit (1975). It seems fairly likely that these mechanisms play some role in producing the observed movement, but the extent of that role is not presently known. We believe that the analysis of the float data demonstrates fairly conclusively that the mechanism proposed by Hogg & Stommel (1990) plays a role in producing the observed propagation, and feel that the quantitative disagreement between the propagation speeds of the model solutions and observed Meddy propagation speeds is due in large part to the fixed horizontal scale of the model solutions, rather than to the neglect of β , or other model deficiencies. An examination of the effect of allowing the horizontal scale of the lens to vary would be an interesting topic for further investigation. This would allow a more meaningful comparison of the model results with the data. In particular, such an analysis would give a better idea of where Mediterranean Salt Lenses actually lie in the (α, b) plane (see Figure 4.8), which would allow a reasonably confident prediction of whether or not the unstable breakdown of the steady solutions documented in Chapter 4 can be expected to be an important oceanic effect. Despite the shortcomings in the

present work which have been noted, it is felt that the simple model examined here does a surprisingly good job of modeling several aspects of the behavior of real Mediterranean Salt Lenses.

Appendix 1: Kinematics

In this section the velocity field will be computed from the streamfunction ψ . Expressing the unit vertical vector \hat{z} and the gradient operator $\vec{\nabla}$ in the spherical coordinates (r, θ, ϕ) :

$$\hat{z} = \hat{r} \cos \theta - \hat{\theta} \sin \theta, \quad (\text{A1.1})$$

$$\vec{\nabla} \psi = \hat{r} \psi_r + \frac{\hat{\theta}}{r} \psi_\theta + \frac{\hat{\phi}}{r \sin \theta} \psi_\phi, \quad (\text{A1.2})$$

and recalling that the velocity and streamfunction are related by

$$\vec{u} = \hat{z} \times \vec{\nabla} \psi, \quad (\text{A1.3})$$

it follows that

$$\vec{u} = \hat{z} \times \vec{\nabla} \psi = -\hat{r} \psi_\phi / r - \hat{\theta} \frac{\cot \theta}{r} \psi_\phi + \hat{\phi} \left(\frac{\cos \theta}{r} \psi_\theta + \sin \theta \psi_r \right). \quad (\text{A1.4})$$

Thus the ϕ velocity component is given by

$$u^{(\phi)} = \frac{\cos \theta}{r} \psi_\theta + \sin \theta \psi_r. \quad (\text{A1.5})$$

These general relations can now be utilized to examine the flow associated with the basic state streamfunction (3.7):

$$\psi^v = \begin{pmatrix} r^2/6 - 1/2 \\ -1/3r \end{pmatrix} + b \begin{pmatrix} zr^2/10 - z/6 \\ -z/15r^3 \end{pmatrix}. \quad (\text{A1.6})$$

It follows by differentiation that

$$\psi_r^v = \begin{pmatrix} r/3 \\ 1/3r^2 \end{pmatrix} + b \begin{pmatrix} 3r^2 \cos \theta / 10 - \cos \theta / 6 \\ 2 \cos \theta / 15r^3 \end{pmatrix}, \quad (\text{A1.7})$$

and

$$\psi_\theta^v = b \begin{pmatrix} -r^3 \sin \theta / 10 + r \sin \theta / 6 \\ \sin \theta / 15r^2 \end{pmatrix}, \quad (\text{A1.8})$$

so that

$$u^{(\phi)} = \frac{1}{3} r \sin \theta \begin{pmatrix} 1 \\ 1/r^3 \end{pmatrix} + \frac{1}{10} b r^2 \sin 2\theta \begin{pmatrix} 1 \\ 1/r^5 \end{pmatrix}. \quad (\text{A1.9})$$

Within the vortex core, this may be written

$$u^{(\phi)} = \frac{1}{3}r_{\perp} + \frac{1}{5}b z r_{\perp}, \quad (\text{A1.10})$$

where $r_{\perp} = r \sin \theta$ is the perpendicular distance from the z axis. It follows that the monopolar component of the potential vorticity field induces a flow within the vortex core which is independent of z , while the dipole component induces a flow which has uniform shear in z .

Appendix 2: Calculation of the Integral (3.72)

In this section the integral (3.72) is computed for the continuous vortex model, in which case

$$u_0 \equiv \frac{d}{dt} \int \int \int_{r \leq 1+\eta} q x d\tau / \int \int \int_{r \leq 1+\eta} q d\tau = \int \int \int_{r \leq 1+\eta} q u d\tau / \int \int \int_{r \leq 1+\eta} q d\tau . \quad (\text{A2.1})$$

Physically, this says that the center of potential vorticity moves at a weighted average of the flow speed over the vortex core. The translation speed u_0 is therefore defined to be the rate at which the center of potential vorticity moves.

We intend to find u_0 by evaluating the second integral above. The calculation can be considerably simplified by making use of a generalized version of the well known Poincare vorticity theorem, which governs the evolution of various moments of a vorticity field. To establish the theorem for stratified quasigeostrophic flows will require a brief diversion. The theorem will show that u_0 , as defined above, must vanish in the absence of an external flow u_b . More specifically, u_0 must vanish if the flow decays faster than $1/r$ as $r \rightarrow \infty$. Because the calculations in Chapter 3 showed that velocities associated with the basic state vortex are of $O(r^{-2})$ as $r \rightarrow \infty$, it follows that only the background flow (which doesn't vanish as $r \rightarrow \infty$) contributes to the above integral. To show this, we begin with the potential vorticity equation

$$q_t + \vec{\nabla} \cdot (q\vec{u}) = 0 , \quad (\text{A2.2})$$

where

$$q = \psi_{xx} + \psi_{yy} + \psi_{zz} \quad (\text{A2.3})$$

$$u = -\psi_y$$

$$v = +\psi_x .$$

If the potential vorticity equation is multiplied by some twice differentiable function $A(x, y, z)$, a little manipulation gives

$$(Aq)_t + \vec{\nabla} \cdot (Aq\vec{u}) = q\vec{u} \cdot \vec{\nabla} A . \quad (\text{A2.4})$$

Further manipulation shows that the right side of this equation can be written in the form

$$\begin{aligned}
q\vec{u} \cdot \vec{\nabla} A &= (uvA_x + \frac{1}{2}(v^2 - u^2)A_y - \frac{1}{2}A_y\psi_z^2)_x + \\
&+ (-uvA_y + \frac{1}{2}(v^2 - u^2)A_x + \frac{1}{2}A_y\psi_z^2)_y + \\
&+ (uA_x\psi_z + vA_y\psi_z)_z + \\
&- uv(A_{xx} - A_{yy}) - 2A_{xy}(v^2 - u^2)/2 - uA_{xz}\psi_z - vA_{yz}\psi_z.
\end{aligned} \tag{A2.5}$$

Now, if $A(x, y, z)$ is chosen such that

$$\begin{aligned}
A_{xx} &= A_{yy} \\
A_{xy} &= A_{xz} = A_{yz} = 0,
\end{aligned} \tag{A2.6}$$

it follows that (A2.4) can be written in the form

$$(Aq)_t + \vec{\nabla} \cdot (Aq\vec{u} - \vec{S}) = 0, \tag{A2.7}$$

where \vec{S} is given by

$$\begin{aligned}
\vec{S} &= \hat{x}(uvA_x + \frac{1}{2}(v^2 - u^2)A_y - \frac{1}{2}A_y\psi_z^2) + \\
&+ \hat{y}(-uvA_y + \frac{1}{2}(v^2 - u^2)A_x + \frac{1}{2}A_y\psi_z^2) + \\
&+ \hat{z}(uA_x\psi_z + vA_y\psi_z).
\end{aligned} \tag{A2.8}$$

In accordance with (A2.6), $A(x, y, z)$ is chosen in the special form

$$A(x, y, z) = a_1(x^2 + y^2) + a_2z^2 + a_3x + a_4y + a_5z + a_6. \tag{A2.9}$$

Now, if u , v , and ψ_z decay sufficiently rapidly as $r \rightarrow \infty$, (A2.7) can be integrated over all space to obtain:

$$\partial_t \int \int \int Aq d\tau = - \int \int (Aq\vec{u} - \vec{S}) \cdot d\vec{\sigma}, \tag{A2.10}$$

where the surface integral results from using the divergence theorem, and the integration is considered to be over the surface of a sphere of radius r as $r \rightarrow \infty$. Consider now the

case in which $A = z$ (which may be obtained through a suitable choice of the coefficients in (A2.9)), and there is no external flow, so that $q = 0$ outside the vortex and u, v , and ψ_z all vanish as $r \rightarrow \infty$. Because u, v , and ψ_z are of $O(r^{-2})$ as $r \rightarrow \infty$ and the surface of integration increases like r^2 , it follows that the right hand side of (A2.10) vanishes, and therefore

$$\partial_t \int \int \int x q_v d\tau = 0. \quad (\text{A2.11})$$

Because the integral is only a function of t , the partial derivative in (A2.11) can be replaced by a total derivative, and then it follows from (A2.1) that

$$\int \int \int u_v q_v d\tau = 0. \quad (\text{A2.12})$$

Therefore, in the absence of an external flow, the center of potential vorticity of the vortex cannot move ($u_0 = 0$).

As a result of (A2.12), the integral (A2.1) can be written in the form

$$u_0 = \int \int \int_{r \leq 1+\eta} q_v u_b d\tau / \int \int \int_{r \leq 1+\eta} q_v d\tau, \quad (\text{A2.13})$$

where now only the *external* flow u_b appears in the integrand. Next, because $\eta \ll 1$ the integration can to a good approximation be carried out over the volume $r \leq 1$ of the basic state vortex. This leads to

$$u_0 \approx \int \int \int_{r \leq 1} (1 + q_b + bz)(u_v + u_b) d\tau / (\frac{4}{3}\pi) + O(\eta^2). \quad (\text{A2.14})$$

The part of the integrand proportional to u_v integrates to zero, for the reasons discussed above. Thus, in spherical coordinates:

$$u_0 \approx (\frac{4}{3}\pi)^{-1} \int \int \int_{r \leq 1} (1 + q_b + br \cos \theta)(\alpha r \cos \theta - q_b r \sin \theta \sin \phi) r^2 \sin \theta dr d\theta d\phi, \quad (\text{A2.15})$$

where we have put

$$u_b = \alpha z - q_b y,$$

as in Chapter 3. All terms proportional to q_b integrate out, and we are left with

$$u_0 \approx \alpha b (\frac{4}{3}\pi)^{-1} \int \int \int_{r \leq 1} r^4 \cos^2 \theta \sin \theta dr d\theta d\phi, \quad (\text{A2.16})$$

which may be readily evaluated to get

$$u_0 \approx \frac{1}{5} \alpha b . \quad (\text{A2.17})$$

This is the potential vorticity weighted average of the background flow speed over the core. In the present case, it can be shown that this is equal to the background flow speed at the center of potential vorticity:

$$\langle u_b \rangle = u_b(\langle x \rangle, \langle y \rangle, \langle z \rangle) , \quad (\text{A2.18})$$

where we use the notation

$$\langle \Phi \rangle \equiv \int \int \int_{r \leq 1+\eta} q_v \Phi d\tau / \int \int \int_{r \leq 1+\eta} q_v d\tau . \quad (\text{A2.19})$$

The result (A2.18) follows from the fact that u_b is a linear function of its arguments. This relation will be used to compute the translation speeds of the numerical solutions discussed in Chapter 4.

Appendix 3: Evaluation of the Integral (3.41)

In this section the integral

$$F_{mn} = \int \int_{\text{sphere}} (u_0 \sin \theta \cos \phi + \psi_b) Y_n^{m*} d\sigma \quad (\text{A3.1})$$

is evaluated, which is just equation (3.41) from Chapter 3. As in Chapter 3, ψ_b is of the form

$$\psi_b = \frac{1}{2} q_b y^2 - \alpha yz, \quad (\text{A3.2})$$

so that (A3.1) may be written

$$F_{mn} = \int \int_{\text{sphere}} (u_0 \sin \theta \cos \phi - \alpha \sin \theta \cos \theta \cos \phi + \frac{1}{2} q_b \sin^2 \theta \sin 2\phi) Y_n^{m*} d\sigma. \quad (\text{A3.3})$$

Making use of the following definitions (see, e.g., Arfken, p.448):

$$\begin{aligned} Y_1^1 &= -\sqrt{\frac{3}{8\pi}} \sin \theta e^{i\phi} \\ Y_1^{-1} &= +\sqrt{\frac{3}{8\pi}} \sin \theta e^{-i\phi} \\ Y_2^1 &= -3\sqrt{5/24\pi} \sin \theta \cos \theta e^{i\phi} \\ Y_2^{-1} &= +3\sqrt{5/24\pi} \sin \theta \cos \theta e^{-i\phi} \\ Y_2^2 &= +3\sqrt{\frac{5}{96\pi}} \sin^2 \theta e^{2i\phi} \\ Y_2^{-2} &= +3\sqrt{\frac{5}{96\pi}} \sin^2 \theta e^{-2i\phi}, \end{aligned} \quad (\text{A3.4})$$

it is easily shown that

$$\begin{aligned} \sin \theta \cos \phi &= -\sqrt{8\pi/3} (Y_1^1 - Y_1^{-1})/2 \\ \sin \theta \cos \theta \cos \phi &= -\frac{1}{6} \sqrt{24\pi/5} (Y_2^1 - Y_2^{-1}) \\ \sin^2 \theta \sin 2\phi &= \frac{1}{6i} \sqrt{96\pi/5} (Y_2^2 - Y_2^{-2}). \end{aligned} \quad (\text{A3.5})$$

Substituting these expressions into the integral (A3.3), and using the orthogonality properties of the spherical harmonics ¹ gives

$$\begin{aligned} F_{mn} &= -u_0 \sqrt{2\pi/3} (\delta_{n,1} \delta_{m,1} - \delta_{n,1} \delta_{m,-1}) \\ &\quad + \frac{q_b}{12i} \sqrt{96\pi/5} (\delta_{n,2} \delta_{m,2} - \delta_{n,2} \delta_{m,-2}) + \frac{1}{6} \alpha \sqrt{24\pi/5} (\delta_{n,2} \delta_{m,1} - \delta_{n,2} \delta_{m,-1}). \end{aligned} \quad (\text{A3.6})$$

¹ $\int \int_{\text{sphere}} Y_n^{m'*} Y_n^m d\sigma = \delta_{n,n'} \delta_{m,m'}$

Appendix 4: Numerical Implementation of the Contour Dynamics Algorithm

In this section a summary of the numerical implementation of the contour dynamics code used in Chapter 4 is given. The derivation of the analytical form of the equations was given in Chapter 4. The code is designed to solve the following set of integro-differential equations numerically

$$\begin{aligned}\frac{dx}{dt} &= - \int \int q_v(z_0) G dx_0 dz_0 + u_b \\ \frac{dy}{dt} &= - \int \int q_v(z_0) G dy_0 dz_0 + v_b .\end{aligned}\tag{A4.1}$$

At each time step, the surface integral on the right hand side is computed numerically, then the points on the boundary are evolved in time, using a 2nd order Runge-Kutta time stepping scheme to compute the time derivatives. The numerical results appear to be quite accurate. Numerical integrations reproduce the particle rotation rates and the precession frequencies of the simple analytical solutions quite accurately. In addition, the area within each horizontal contour is preserved quite accurately (as it should be) as long as the boundary is adequately resolved and the time step not too large.

In order to compute the integral, the boundary must first be discretized. This is done by taking horizontal sections through the vortex, so that the surface is represented by a series of closed horizontal contours. Each of these contours is in turn represented by a number of points $x(i)$, $y(i)$, spaced more or less evenly around the contour. The boundary must then be 'tiled' into uniquely defined area elements. This is done by defining quadrilateral elements everywhere except at the top and bottom, where triangular elements are used. This is sketched in Figure A7.1a. The tiling system requires that each layer have the same number of points, so that shorter contours (e.g., the top and bottom) will be relatively over resolved. In addition, the scheme requires that points in adjacent layers remain relatively well 'synchronized'. Therefore, at each time step the points on a given layer are relabeled so that the 'first' point on the contour is more or less aligned with the first point on the contour immediately above. The points are then redistributed so that they are equally spaced around each contour.

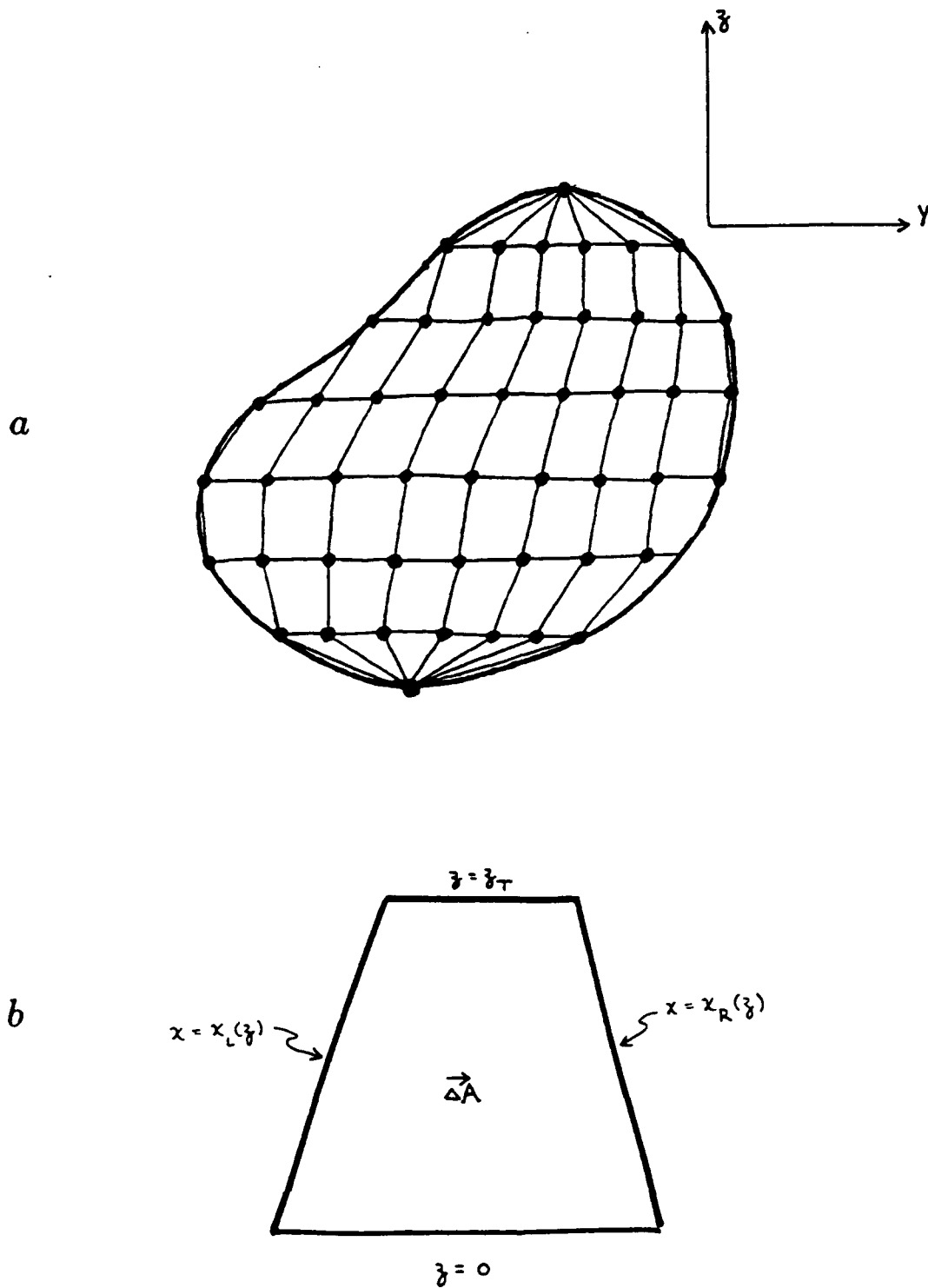


Figure A7.1: Figure A7.1a illustrates the way in which the boundary of the lens is tiled. At the top and bottom of the lens area elements are triangular; everywhere else they are quadrilaterals. Figure A7.1b shows a typical area element.

The numerical implementation of (A4.1) can be written

$$\begin{aligned}\frac{dx_{ij}}{dt} &= -\Sigma_k \Sigma_l G(\vec{x}_{ij} | \vec{x}_{c,kl}) q_v(z_{c,k}) \delta x_c \delta z_c + s.p. + u_b(\vec{x}_{ij}), \\ \frac{dy_{ij}}{dt} &= -\Sigma_k \Sigma_l G(\vec{x}_{ij} | \vec{x}_{c,kl}) q_v(z_{c,k}) \delta y_c \delta z_c + s.p. + v_b(\vec{x}_{ij}),\end{aligned}\quad (A4.2)$$

where $\vec{x}_{c,kl}$ gives the coordinates of the 'centroid' of an area element. Thus, G is evaluated at the centroid of each area element, multiplied by the elemental area, and summed. It should be noted that the summation is carried out over only those elements which are not adjacent to the point \vec{x}_{ij} , since the integrand varies rapidly in these regions, and an analytic 'patch' (denoted by $s.p.$) is needed. Furthermore, the accuracy of the calculation improved when the Green's function was expanded in a truncated Taylor series about the centroid of nearby area elements. This patch is obtained by finding an analytic expression for the integral of the Green's Function on elements surrounding the source point. The sourcepoint integral is of the form

$$s.p. = \int \int_{\Delta A} \frac{dx dz}{\sqrt{x^2 + z^2}}. \quad (A4.3)$$

At the top and bottom of the boundary the shape of the elemental area ΔA is triangular, everywhere else the ΔA are quadrilaterals, as shown in Figure A7.1a.

To compute the sourcepoint integral, consider the area ΔA shown in Figure A7.1b. Assume that in a locally defined coordinate system the bottom of the element is given by $z = 0$ and the top is at $z = z_T$. In addition, assume that the left and right sides are given by $x_L = Bz$ and $x_R = C + Dz$, respectively. The integral (A4.3) can then be integrated once to get

$$s.p. = \int_0^{z_T} \ln(x + \sqrt{x^2 + z^2}) \Big|_{x_L}^{x_R} dz. \quad (A4.4)$$

This can be rewritten in the form

$$s.p. = \int_0^{z_T} \left(\sinh^{-1}(x_R(z)/z) - \sinh^{-1}(x_L(z)/z) \right) dz, \quad (A4.5)$$

which can be evaluated to get

$$s.p. = z_T \sinh^{-1} B - z_T \sinh^{-1}(D + C/z_T) +$$

$$+ \frac{C}{\sqrt{1+D^2}} (\sinh^{-1} D - \sinh^{-1} (\frac{CD/z_T + 1 + D^2}{C/z_T})) . \quad (\text{A4.6})$$

This result can be substituted into (A4.2), and the boundary can then be evolved in time.

References

- Arfken, G., *Mathematical methods for physicists*, Academic Press, New York, N.Y., 1966.
- Armi, L., and W. Zenk, Large lenses of highly saline Mediterranean water, *J. Phys. Oceanogr.*, **14**, 1560–1576, 1984.
- Armi, L., D. Hebert, N. Oakey, J. Price, P.L. Richardson, T. Rossby, and B. Ruddick, The History and decay of a Mediterranean Salt Lens, *Nature*, **333**, 649–651, 1988.
- Armi, L., D. Hebert, N. Oakey, J. Price, P.L. Richardson, T. Rossby, and B. Ruddick, Two years in the life of a Mediterranean Salt Lens, *J. Phys. Oceanogr.*, **19**, 354–370, 1989.
- Batchelor, G.K., *An Introduction to Fluid Mechanics*, Cambridge University Press, 615 pp., 1967.
- Beckmann, A., and R.H. Kase, Numerical simulation of the movement of a Mediterranean Salt Lens, *Geophys. Res. Lett.*, **16**, 65–68, 1989.
- Bretherton, F.B., and M. Karweit, Mid-ocean mesoscale modeling, *Numerical Models of the Ocean Circulation*, National Academy of Sciences, Washington D.C., 1975.
- Brickman, D., The behavior and stability of a lens in a strain field, *J. Geophys. Res.*, **95**, 9657–9670, 1990.
- Clay, C.S., and H. Medwin, *Acoustical Oceanography*, John Wiley & Sons, New York, N.Y., 1977.
- Colin de Verdiere, A., On the southward motion of Mediterranean Salt Lenses, *J. Phys. Oc.*, in press.
- D'Asaro, E.A., Observations of small eddies in the Beaufort sea, *J. Geophys. Res.*, **93**, 6669–6684, 1988.
- Dritschel, D.G., The repeated filamentation of two-dimensional vorticity interfaces, *J. Fluid Mech.*, **194**, 511–547, 1988.
- Flierl, G.R., Baroclinic solitary waves with radial symmetry, *Dyn. Atm. Oc.*, **3**, 15–38, 1990.
- Flierl, G.R., V.D. Larichev, J.C. McWilliams, and G.M. Reznik, The Dynamics of baroclinic and barotropic solitary eddies, *Dyn. Atm. Oc.*, **5**, 1–41, 1980.
- Flierl, G.R., Particle motions in large amplitude wave fields, *Geophys. Astrophys. Fluid Dyn.*, **18**, 39–74, 1981.
- Flierl, G.R., Isolated eddy models in geophysics, *Ann. Rev. Fluid Mech.*, **19**, 493–530, 1987.
- Flierl, G.R., M.E. Stern, and J.A. Whitehead, The physical significance of modons: laboratory experiments and general integral constraints, *Dyn. Atm. Oc.*, **7**, 233–263, 1983.
- Flierl, G.R., On the instability of geostrophic vortices, *J. Fluid Mech.*, **197**, 349–388, 1988.

- Gent, P.R., and J.C. McWilliams, The instability of circular vortices, *Geophys. Astrophys. Fluid Dyn.*, **35**, 209–233, 1986.
- Gill, A.E., Homogeneous intrusions in a rotating stratified fluid, *J. Fluid Mech.*, **103**, 275–296, 1981.
- Griffiths, R.W., and P.F. Linden, The stability of vortices in a rotating stratified fluid, *J. Fluid Mech.*, **117**, 343–377, 1981.
- Hebert, D.L., A Mediterranean Salt Lens. *Ph.D. Thesis, Dalhousie Univ.*, 187 pp., 1988.
- Hebert, D.L., Evolution of a Mediterranean salt lens: scalar properties, *J. Phys. Oceanogr.*, **20**, 1468–1483, 1990.
- Hedstrom, K., and L. Armi, An experimental study of homogeneous lenses in a stratified rotating fluid, *J. Fluid Mech.*, **191**, 535–556, 1988.
- Helfrich, K.R., and U. Send, Finite-amplitude evolution of two-layer geostrophic vortices, *J. Fluid Mech.*, **197**, 331–348, 1988.
- Helfrich, K.R., Experiments on baroclinic eddy evolution and stability in rotating continuously stratified systems, *Proc. 3^d International Symposium on Stratified Fluids*.
- Hildebrand, F.B., *Advanced calculus for applications*, Prentice-Hall, Englewood Cliffs, N.J., 1976.
- Hogg, N.G., and H.M. Stommel, How currents in the upper thermocline could advect Meddies deeper down, *Deep-Sea Research*, **37**, 613–623, 1990.
- Hogg, N.G., and H.M. Stommel, Hetonic explosions: the breakup and spread of warm pools as explained by baroclinic point vortices, *J. Atm. Sci.*, **42**, 1465–1476, 1985.
- Ikeda, M., Instability and splitting of mesoscale rings using a two-layer quasi-geostrophic model on an f -plane, *J. Phys. Oceanogr.*, **11**, 987–998, 1981.
- Ikeda, M., A simple model of subsurface mesoscale eddies, *J. Geophys. Res.*, **87**, 7925–7931, 1982.
- Killworth, P.D., On the motion of isolated lenses on a β -plane, *J. Phys. Oceanogr.*, **13**, 368–376, 1983.
- Killworth, P.D., On the propagation of multilayer and continuously stratified eddies, *J. Phys. Oceanogr.*, **16**, 709–716, 1986.
- Kozlov, B.F., Construction of a numerical model of geostrophic eddies in a baroclinic fluid based on the contour dynamics method, *Izvestiya, Atmospheric and Oceanic Physics*, **21**, 161–163, 1985.
- Manley, T.O., and K. Hunkins, Mesoscale eddies of the Arctic Ocean, *J. Geophys. Res.*, **90**, 4911–4930, 1985.
- McDowell, S.E., and H.T. Rossby, Mediterranean water: an intense mesoscale eddy off the Bahamas, *Science*, **202**, 1085–1087, 1978.

- McWilliams, J.C., and G.R. Flierl, On the evolution of isolated, nonlinear vortices, *J. Phys. Oc.*, **9**, 1155–1182, 1979.
- McWilliams, J.C., and P.R. Gent, The evolution of sub-mesoscale coherent vortices on the β -plane, *Geophys. Astrophys. Fluid Dyn.*, **35**, 235–255, 1986.
- McWilliams, J.C., Submesoscale coherent vortices in the ocean, *Rev. Geophys.*, **23**, 165–182, 1985.
- Meacham, S.P., Steadily rotating quasigeostrophic vortices in a stratified fluid, *unpublished manuscript*.
- Meacham, S.P., G.R. Flierl, and U. Send, Vortices in Shear, *Dyn. Atm. Oc.*, **14**, 333–386, 1990.
- Nof, D., On the β -induced movement of isolated baroclinic eddies, *J. Phys. Oceanogr.*, **11**, 1662–1672, 1981.
- Pedlosky, J., The instability of continuous heton clouds, *J. Atm. Sci.*, **42**, 1477–1486, 1985.
- Pedlosky, J., *Geophysical Fluid Dynamics*, Springer-Verlag, New York, N.Y., 1987.
- Polvani, L.M., Geostrophic Vortex Dynamics, *Ph.D. Thesis, MIT-WHOI Joint Program*, 1989.
- Pratt, L.J., and M.E. Stern, Dynamics of potential vorticity fronts and eddy detachment, *J. Phys. Oceanogr.*, **16**, 1101–1120, 1986.
- Press, W.H., B.P. Flannery, S.A. Teukolsky, and W.T. Vetterling, *Numerical recipes (The art of scientific computing)*, Cambridge University Press, 818 pp., 1986.
- Price, J.F., T.K. McKee, J.R. Valdes, P.L. Richardson, and L. Armi, SOFAR Float Mediterranean Outflow Experiment Data from the First Year, 1984–1985, *Woods Hole Oceanographic Institution Technical Report*, WHOI-86-31, July 1986.
- Richardson, P.L., Gulf stream rings, in *Eddies in Marine Science*, edited by A.R. Robinson, Springer-Verlag, New York, N.Y., 1983.
- Richardson, P.L., D. Walsh, L. Armi, and J. Price, Tracking three meddies with SOFAR floats, *J. Phys. Oceanogr.*, **19**, 371–383, 1989.
- Richardson, P.L., M.S. McCartney, and C. Maillard, A Search for Meddies in Historical Data, *Dyn. Atm. Oc.*, **15**, 241–265, 1991.
- Riser, S.C., W.B. Owens, H.T. Rossby, and C.C. Ebbesmeyer, The structure, dynamics, and origin of a small-scale lens of water in the western North Atlantic thermocline, *J. Phys. Oceanogr.*, **16**, 572–590, 1986.
- Rossby, T., Five drifters in a Mediterranean salt lens, *Deep Sea Res.*, **35**, 1653–1663, 1988.
- Ruddick, B.R., Anticyclonic lenses in large scale strain and shear, *J. Phys. Oceanogr.*, **17**, 741–749, 1986.
- Ruddick, B.R., and D. Hebert, The mixing of meddy “Sharon”, in *Small Scale Turbulence and Mixing in the Ocean, Elsevier Oceanography Series*, vol. 46, edited by J.C. Nihoul and B.M. Jamart, Elsevier, N.Y., U.S.A., pp. 249–262, 1988.

- Saunders, P.M., Circulation in the eastern North Atlantic, *J. Mar. Res.*, **40**, 641-657, 1981.
- Shultz Tokos, K., and T. Rossby, Kinematics and dynamics of a Mediterranean Salt Lens, *J. Phys. Oceanogr.*, **21**, 879-892, 1991.
- Stern, M.E., and L.J. Pratt, Dynamics of vorticity fronts, *J. Fluid Mech.*, **161**, 513-532, 1985.
- Yano, J., and G.R. Flierl, Isolated Potential Vorticity Patches in Quasi-Geostrophic Zonal Flows, *in press, Dyn. Atm. Oc.*
- Zabusky, N.J., M.H. Hughes, and K.V. Roberts, Contour Dynamics for the Euler Equations in Two Dimensions, *J. Comp. Phys.*, **30**, 96-106, 1979.
- Zemanovic, M.E., P.L. Richardson, J.R. Valdes, J.F. Price, and L. Armi, SOFAR Float Mediterranean Outflow Experiment Data from the Second Year, 1985-1986, *Woods Hole Oceanographic Institution Technical Report*, WHOI-88-43, September 1988.
- Zhmur, V.V., Dynamics of vortices with ellipsoidal form of core in a stratified ocean, *unpublished manuscript*.

DOCUMENT LIBRARY

March 11, 1991

Distribution List for Technical Report Exchange

Attn: Stella Sanchez-Wade
Documents Section
Scripps Institution of Oceanography
Library, Mail Code C-075C
La Jolla, CA 92093

Hancock Library of Biology &
Oceanography
Alan Hancock Laboratory
University of Southern California
University Park
Los Angeles, CA 90089-0371

Gifts & Exchanges
Library
Bedford Institute of Oceanography
P.O. Box 1006
Dartmouth, NS, B2Y 4A2, CANADA

Office of the International
Ice Patrol
c/o Coast Guard R & D Center
Avery Point
Groton, CT 06340

NOAA/EDIS Miami Library Center
4301 Rickenbacker Causeway
Miami, FL 33149

Library
Skidaway Institute of Oceanography
P.O. Box 13687
Savannah, GA 31416

Institute of Geophysics
University of Hawaii
Library Room 252
2525 Correa Road
Honolulu, HI 96822

Marine Resources Information Center
Building E38-320
MIT
Cambridge, MA 02139

Library
Lamont-Doherty Geological
Observatory
Columbia University
Palisades, NY 10964

Library
Serials Department
Oregon State University
Corvallis, OR 97331

Pell Marine Science Library
University of Rhode Island
Narragansett Bay Campus
Narragansett, RI 02882

Working Collection
Texas A&M University
Dept. of Oceanography
College Station, TX 77843

Library
Virginia Institute of Marine Science
Gloucester Point, VA 23062

Fisheries-Oceanography Library
151 Oceanography Teaching Bldg.
University of Washington
Seattle, WA 98195

Library
R.S.M.A.S.
University of Miami
4600 Rickenbacker Causeway
Miami, FL 33149

Maury Oceanographic Library
Naval Oceanographic Office
Stennis Space Center
NSTL, MS 39522-5001

Marine Sciences Collection
Mayaguez Campus Library
University of Puerto Rico
Mayaguez, Puerto Rico 00708

Library
Institute of Oceanographic Sciences
Deacon Laboratory
Wormley, Godalming
Surrey GU8 5UB
UNITED KINGDOM

The Librarian
CSIRO Marine Laboratories
G.P.O. Box 1538
Hobart, Tasmania
AUSTRALIA 7001

Library
Proudman Oceanographic Laboratory
Bidston Observatory
Birkenhead
Merseyside L43 7 RA
UNITED KINGDOM

REPORT DOCUMENTATION PAGE		1. REPORT NO. WHOI-92-21	2.	3. Recipient's Accession No.
Title and Subtitle A Model of a Mediterranean Salt Lens in External Shear				5. Report Date June, 1992
Author(s) David Walsh				6.
Performing Organization Name and Address The Woods Hole Oceanographic Institution Woods Hole, Massachusetts 02543				8. Performing Organization Rept. No. WHOI 92-21
Sponsoring Organization Name and Address Funding was provided by the Office of Naval Research and the National Science Foundation.				10. Project/Task/Work Unit No.
				11. Contract(C) or Grant(G) No. (C) N00014-89-J-1182 (G) OCE89-16446/OCE87-00601
				13. Type of Report & Period Covered Ph.D. Thesis
				14.

Supplementary Notes

This report should be cited as: David Walsh. A Model of a Mediterranean Salt Lens in External Shear.
Ph. D. Thesis, WHOI-92-21.

Abstract (Limit: 200 words)

A pair of models representing the interaction of a continuously stratified f-plane quasigeostrophic lens with an external shear flow are examined. The first models the eddy as a pair of quasigeostrophic 'point potential vortices' in uniform external shear; in the second the lens is represented by an isolated three dimensional patch with potential vorticity linear in z, which is embedded in a uniform shear. Analytical solutions are found representing a baroclinic lens with a trapped fluid core, which may propagate in the presence of external shear. An algorithm which is a generalization of the contour dynamics technique to stratified quasigeostrophic flows is used to extend these results into the nonlinear domain, allowing a determination of the range of conditions in which steadily translating solutions may be found. The stability of the solutions is examined numerically, and it is found that the solutions are stable neither the external shear nor the core baroclinicity are too large. As a test of the model, new results from a recent SOFAR float experiment are presented. The data show that the cores of two different Mediterranean Salt lenses are tilted in agreement with the model solutions, presumably as a result of interactions with external flows.

Document Analysis a. Descriptors

1. quasigeostrophic vortex dynamics
2. Mediterranean salt lenses
3. contour dynamics

b. Identifiers/Open-Ended Terms**c. COSATI Field/Group****Availability Statement**

Approved for publication; distribution unlimited.

19. Security Class (This Report)

UNCLASSIFIED

21. No. of Pages

174

20. Security Class (This Page)**22. Price**